Doctoral Dissertations   Student Theses and Dissertations

Spring 2019

Pressure versus impulse graph for blast-induced traumatic brain injury and correlation to observable blast injuries

Barbara Rutter

Follow this and additional works at: https://scholarsmine.mst.edu/doctoral_dissertations

Part of the Explosives Engineering Commons, and the Mathematics Commons
Department: Mining and Nuclear Engineering

Recommended Citation

PRESSURE VERSUS IMPULSE GRAPH FOR BLAST-INDUCED TRAUMATIC BRAIN

INJURY AND CORRELATION TO OBSERVABLE BLAST INJURIES

BY

BARBARA RUTTER

A DISSERTATION

Presented to the Faculty of the Graduate School of the

MISSOURI UNIVERSITY OF SCIENCE AND TECHNOLOGY

In Partial Fulfillment of the Requirements for the Degree

DOCTOR OF PHILOSOPHY

IN

EXPLOSIVES ENGINEERING

2019

Approved by:

Catherine E. Johnson, Advisor
Kyle Perry
Braden Lusk
Paul Worsey
Dimitri Feys

ABSTRACT

With the increased use of explosive devices in combat, blast induced traumatic brain injury (bTBI) has become one of the signature wounds in current conflicts. Animal studies have been conducted to understand the mechanisms in the brain and a pressure versus time graph has been produced. However, the role of impulse in bTBIs has not been thoroughly investigated for animals or human beings.

This research proposes a new method of presenting bTBI data by using a pressure versus impulse (P-I) graph. P-I graphs have been found useful in presenting lung lethality regions and building damage thresholds. To present the animal bTBI data on a P-I graph for humans, the reported peak pressures needed to be scaled to humans, impulse values calculated, and impulse values scaled. Peak pressures were scaled using Jean et al.'s method, which accounts for all the structures of the head. Impulse values were estimated in two methods: Friedlander's impulse equation and a proposed modification to the Friedlander's impulse equation. The modification was needed as some animal testing was not subjected to shock waves with a steady decay, such as outside the end of a shock tube. Mass scaling was used to scale the reported time duration in the impulse calculation.

The scaled peak pressure and impulse values were plotted on a P-I graph with the reported severity. The three severities did not overlap; thus, each severity had its own region on the P-I graph. The severity regions were overlaid with lung damage and eardrum rupture P-I curves. Seven correlations were found between the bTBI regions and the observable injuries. bTBIs are not a new phenomenon, but in the past other serious injuries were more prominent, due to body armor not attenuating the shock wave as effectively.

iv

ACKNOWLEDGMENTS

TABLE OF CONTENTS

LIST OF FIGURES

LIST OF TABLES

NOMENCLATURE

Symbol	Description
a	Experiment-fitting constant
a	Direction and width of parabola
A	Fitting parameter
b	Experiment-fitting constant
B	Fitting parameter
bTBI	Blast-induced traumatic brain injury
c	Speed of sound
C_1	Fitting constant for a
C_2	Fitting constant for h
C_3	Fitting constant for k
c_{brain}	Speed of sound in brain
c_{flesh}	Speed of sound in flesh
cm	Centimeter
c_{skull}	Speed of sound in skull
D	Detonation velocity
DAS	Data acquisition system
DDESB	Department of Defense Explosives Safety Board
DVBIC	Defense and Veterans Brain Injury Center
E_{exp}	Available energy of an explosive to do work
EDR	Eardrum rupture
FM	Molecular weight

g	Grams
g_e	moles of gas produced by explosive
GCS	Glasgow coma scale score
h	x value of vertex of a parabola
HE	High explosive
I	Impulse
IED	Improvised explosive device
k	y value of vertex of a parabola
kg	Kilogram
kJ	Kilojoules
kPa	Kilopascal
kPa*s	Kilopascal seconds
LLNL	Lawrence Livermore National Laboratory
m	Meter
$m_{baseline}$	Scaling mass
m_e	Mass of explosive
Missouri S&T	Missouri University of Science and Technology
modTBI	Moderate traumatic brain injury
ms	Milliseconds
m^s_{brain}	Mass of brain in species
m_{scaled}	Mass being scaled
m^s_{flesh}	Mass of flesh in species
m^s_{skull}	Mass of skull in species

mTBI	Mild traumatic brain injury
P	Pressure
P(t)	Pressure function with respect to time
P_0	Fitting parameter
PETN	Pentaerythritol tetranitrate
P_{amb}	Ambient pressure
P-I	Pressure versus impulse
$P_{incident}$	Incident pressure
P_r	Reflective pressure
P^s	Peak overpressure
PP	Peak pressure
psi	Pounds per square inch
psi*s	Pounds per square inch seconds
P-sT	Pressure versus scaled duration
P-T	Pressure versus duration
q	Dynamic pressure
Ref	Reference
s	Seconds
sTBI	Severe traumatic brain injury
t	Time
T	Time duration
t^+	End of positive phase
t_0	Time of arrival

TBI	Traumatic brain injury
TNT	Trinitrotoluene
TNT equ	TNT equivalency
UN	United Nations
V	Volume of the shock tube between the explosive and exit
wt	Weight of explosive
α	Constant modifier
α	Fitting parameter
β	Impulse modifier
γ	Ratio of specific heats of the air
ΔH_R^0	Molar heat of detonation
Δn	Number of moles of gas produced per mole of high explosive
Δt	Change in time
η^s	Scaling parameter

1. INTRODUCTION

1.1. PROBLEM STATEMENT

Traumatic brain injury (TBI) has become one of the most prominent [1–4] and difficult to diagnose injuries [5] of the modern warfighter. Though TBIs have occurred in previous conflicts, modern warfighters are exposed to a greater risk of TBIs. The advent and increased use of improvised explosive devices (IEDs) have led to modern warfighters being more at risk to explosives detonating in close proximity that result in blast-induced TBIs (bTBIs). The increased exposure to conditions that can generate bTBIs has illuminated the need to understand further the bTBI pressure and impulse thresholds.

The survivability after an explosive blast has greatly improved from previous conflicts due to advances in three areas. The first advancement is improved body armor, which has reduced the number of individuals dying from lung injuries. Second, advancements in transporting critically injured warfighters to field hospitals in a timely manner have resulted in life-saving medical treatment. Third, advances in field medicine and field hospitals have allowed medical professionals to stabilize the most critically injured for transport to hospitals in allied countries to receive appropriate treatment [6–8]. Consequentially, the number of warfighters who survive an event resulting in a bTBI whom may have otherwise succumbed to their injuries in previous conflicts have increased. An unfortunate consequence of the increased survival rate is that bTBIs have become more apparent than in prior conflicts. The warfighters who sustained bTBIs can have a wide range of struggles and treatments. For the less severe cases, such as concussion, the treatment has a short duration and has no major lifelong effects. However, for the more

severe cases, the treatment is lifelong and the warfighter may not be able to reenter the workforce [9].

Numerous animal studies have been conducted to gain an understanding of the mechanisms that result in a bTBI. The focus of bTBI studies is identifying the brain's response to dynamic loading from an explosive blast, to aid earlier detection and treatment of bTBIs. A pressure versus scaled duration (P-sT) graph, which was used by Bowen et al. [10] to display lung injury thresholds, is currently used to compare bTBI results across different studies , for example Zhu et al., Jean et al., and Rafaels [11–13]. To allow various animal studies to be viewed on one graph, the overall mass of the animal subject is used as a scaling factor. P-sT graphs plot the peak pressure of the shock wave versus the scaled positive phase.

The P-sT graph cannot be easily compared to other published building damage and lung injury curves. One commonly used method to compare different damage and injury curves from a detonation of an explosive is pressure versus impulse (P-I) graphs [14]. Impulse is defined as the area under the pressure curve in a pressure versus time (P-T) graph, where pressure is the pressure of the shock wave and time is the duration of the shock wave above ambient pressure. Unlike the P-sT graph, a P-I graph accounts for the different impulse values. For example, an open air and shock tube test can have the same peak pressure, but the impulse values can be vastly different. Due to the wide use of the P-sT graph; majority of researchers do not publish the impulse and only publish peak pressure and duration. By graphing both bTBI data and observable physical injury data together on a single P-I graph would allow for any correlations to be identified. Identified correlations

could then be used as visual indicators of an otherwise invisible injury. Early identification and prompt treatment result in improved outcomes for people exposed to bTBI.

1.2. TRAUMATIC BRAIN INJURY

A TBI is "a nondegenerative, noncongenital (not existing at birth) insult to the brain from an external mechanical force, possibly leading to permanent or temporary impairment of cognitive, physical, and psychosocial functions, with an associated diminished or altered state of consciousness" [15]. Four methods of TBIs exist, which are blast-induced, acceleration, thoracic, and penetrating, and are differentiated by the way in which the TBI was acquired. These four methods are further separated into two types, primary and secondary. Primary TBIs occur when an outside force directly interacts with the brain, where bTBI and penetrating TBI are types of primary TBI. Examples include the shock wave encountered in close proximity to a detonating explosive and shrapnel thrown from a detonating explosive impaling the brain, respectively. A secondary TBI occurs when the outside force interacts with the body and the brain is injured as a result of the body insult. Acceleration and thoracic methods are secondary TBIs. Examples of secondary type TBIs include falling, whiplash, and gunshot wounds to the chest. The focus of this research is on primary bTBI and will not discuss the other methods of acquiring TBIs.

A bTBI is acquired when an explosively produced blast wave passes through the skull and interacts with the brain; however, the exact mechanisms behind the injury are not known [16, 17]. For bTBIs and other TBI methods, three severity levels exist: mild, moderate, and severe. One tool found useful in classifying civilian TBIs, but not proven useful in classifying bTBIs, is the Glasgow Coma Scale score (GCS) and is currently used to help determine the severity of bTBIs [4, 18]. The Defense and Veterans Brain Injury

Center (DVBIC) has also published the characteristics of each bTBI severity and the number of service members who have sustained a bTBI [19]. Mild TBI (mTBI) is the most common diagnosis for bTBIs in warfighters [19]. Moderate TBI (modTBI) and severe TBI (sTBI) are less common. The characteristics of mTBI, modTBI, and sTBI are summarized in Table 1.1.

Table 1.1. TBI characteristics from Ling et al. [18] and DVBIC [19]

	mTBI	modTBI	sTBI
GCS	15-13	13-9	8-3
Confusion	< 24 hrs.	> 24 hrs.	> 24 hrs.
Unconsciousness	< 30 min.	30 min. – 24 hrs.	> 24 hrs.
Memory Loss	< 24 hrs.	24 hrs. – 7 days	> 7 days
CT scan	normal	normal/abnormal	-
Brain Imagining	normal	normal/abnormal	abnormal

Unlike other battlefield injuries such as gunshot wounds and traumatic amputations, bTBIs are difficult to diagnose quickly and treatments are varied. Depending on the severity of the bTBI, treatments range from rest to long term rehabilitation therapies [20]. Other currently investigated therapies that have been shown to improve bTBIs include hyperbaric oxygen therapy, noninvasive brain stimulation, and virtual reality [21]. These and other methods in development may lead to alleviating and possibly reversing the effects of TBIs [22]. The likelihood of TBI's effects being reversed or reduced are greatly improved when treatment is rendered shortly after the TBI was acquired [22].

1.3. RESEARCH APPROACH

The overall objective of this research is to use observable physiological injuries as a visual guide in determining if an individual subjected to an explosive blast sustained an invisible bTBI. The hypothesis of this research is a pressure versus impulse (P-I) graph can be used to represent the regions for mild, moderate, and severe bTBIs in humans and relate those regions to observable physiological injuries, which then can be used as an early indicator of the bTBI. Five assumptions were made to produce a P-I graph from available animal bTBI data, which included 16 Missouri blast model tests and 157 data points resulting in a total of 258 data points.

1. bTBI is solely caused by a shock wave (Section 2.2.1)

2. severities of the bTBI are assumed the same whether determined based on behavioral or histological studies (Section 2.2.1)

3. reported pressures and durations are assumed true and can be used for impulse calculations (Section 2.2.1)

4. head scaling is assumed to be true and correct to scale different animal species on the same graph (Section 2.2.2.2)

5. severity regions are independent of animal orientation with respect to shock wave origin (Section 2.2.1)

Assumptions one and two were not addressed in this research, as the data collected from the animals cannot be reanalyzed and this is beyond the scope of this research. Three objectives, summarized in Table 1.2, were defined to address assumptions 3-5 and

determine the validity of the hypothesis. Each objective required a positive outcome to validate the proposed hypothesis. This research has shown it is possible to present bTBI data on a P-I graph with the severity regions related to observable physiological injuries.

Table 1.2. Objectives of Research and Sections where each is addressed

	Objective	Section
1	Accurately determine impulse for all experimental designs	3
2	Scale bTBI studies to humans and create a P-I graph with severity regions	4
3	Correlate human bTBI to observable injuries	5

Objective one required determining impulse equations that could represent all experimental designs when impulse is not calculated and published in the literature. The three experimental designs used to conduct animal bTBI testing are: open-air, shock tube with the animal placed within the shock tube, and shock tube with the animal placed outside the shock tube. For both open-air and shock tube with the animal placed within the tube experimental designs, the integration of the Friedlander equation has been documented to closely approximate the impulse of a shock wave [23]. The Friedlander equation mathematically describes the exponential decay of an open-air blast and estimates the impulse of the shock wave when integrated. Unlike the two previously mentioned locations, animals placed outside the shock tube are exposed to the shock wave and a vortex ring. The vortex ring forms as the shock wave exits the shock tube and follows the shock wave at a slower velocity. The vortex ring influences the shape and duration of the shock wave until the shock wave and vortex ring separate [24–27]. However, no impulse equation

has been published for shock tube experimental designs with the animal placed outside the shock tube. The hypothesis of this objective is the impulse equation for experimental design with the animal placed outside the shock tube is a piecewise function to account for the vortex ring influencing the shape of the shock wave. To test this hypothesis, experimental testing was conducted with a cylindrical shock tube with a pressure sensor placed at set distances outside the tube. This objective is described in Section 3.

Objective two applied the Friedlander equation and the impulse equation determined in objective one to the gathered published animal bTBI data that did not report impulse. The Friedlander equation was used for open air test and interior shock tube experiments. The derived equation was applied to data where the animal was placed outside the shock tube. The impulse was calculated by inputting the needed published values: peak pressure, time duration, mass of explosive, density of explosive, and distance outside the shock tube plus the calculated values: volume of the shock tube and moles of gas produced by the explosive. The reported peak pressures were then scaled to humans by using Jean et al.'s scaling method [12] from assumption four. The published and calculated impulse values were scaled using the mass scaling method proposed by Bowen et al. [10]. The severity and orientation of the animal was applied to each datum point to determine the validity of assumption five. The severity regions for humans were determined by the location of each scaled severity point. The postulate of this objective is humans have a lower pressure threshold, but higher impulse threshold than a majority of animals. The produced P-I graph with severity threshold P-I curves was used to achieve objective two and is discussed in Section 4.

Objective three required gathering known P-I impulse curves for eardrum rupture thresholds, lung injury thresholds, and lung lethality thresholds after an explosive blast. The human bTBI severity curves determined in objective two were then overlaid with these observable injuries to determine if any correlations exist. The hypothesis of this objective is eardrum rupture can be used as a visual sign for possibly sustained mTBI or modTBI and lung injury is a visual sign for both modTBI and sTBI. The existence of correlations between human bTBI P-I severity threshold curves and observable human physiological injury curves would confirm or deny the proposed hypothesis. This objective is described in Section 5. Note: However, in the modern battlefield our troops wear body armor which raises the threshold levels for lung damage. Have sheep, pigs, and goats been tested with body armor?

1.4. CONTRIBUTION TO SCIENCE

This research proposes presenting bTBI data on a pressure versus impulse graph and defining severity regions. To the author's knowledge, no such graph currently exists and would greatly aid in finding the threshold for bTBI in humans. These severity regions can then be compared to published injury thresholds, thus relating the probable severity of an "invisible" injury to observable physical injuries. The visible indictors for unprotected humans could be used by first responders to quickly assess the wounded to determine who also needs to be evaluated for a possible bTBI. Overall, the generation of the bTBI P-I graph can have far reaching effects in military combat situations, live fire training for the military and police, industrial explosions, and acts of terrorism involving explosives.

A new impulse equation was developed to more accurately estimate the impulse of a shock wave outside of a shock tube with the variables provided in published bTBI studies.

The equation accounts for the vortex ring interacting with different portions of the shock wave, resulting in different decay rates and estimates the distance where the vortex ring and shock wave separate. Based on the experiments conducted as part of this research, it is philosophized that:

- The vortex ring extends the positive phase duration of the shock wave

- The vortex ring expands and weakens as it travels away from the shock tube

- The separation distance was found to be dependent upon mass of the explosive, density of the explosive, and gas production of the explosive

With the new impulse equation, a pressure versus impulse graph for human bTBIs was produced from published animal bTBI data. From the pressure versus impulse graph, regions were identified that had little to no bTBI data points. The severity regions were defined and compared to published eardrum rupture and lung injury thresholds. bTBIs were found to occur below the threshold of eardrum rupture, thus a bTBI is likely to have occurred when the eardrum is ruptured or would have without appropriate personal protective equipment.

2. LITERATURE REVIEW

The review of the published literature presented in this section is important to understand the reasoning behind the five assumptions and accomplishment of the three objectives. The literature review is divided into subsections for each of the three objectives listed in Table 1.2. To formulate an impulse equation, knowledge of shock waves, shock wave characteristics, tools used to simulate shock waves, and tools comparing different explosive characteristics are needed (Section 2.1). The current methods used to document bTBIs in animals and scaling methods used to compare between different animal species need to be known in order to derive a P-I graph of human bTBI data from animal bTBI studies (Section 2.2). In order to correlate human bTBI regions to observable injuries, the thresholds and visual characteristics of common shock wave induced injuries need to be known and understood (Section 2.3).

2.1. IMPULSE CALCULATION

This section discusses the properties of shock waves, explosives, and P-I graphs.

2.1.1. Shock Waves. A shock wave is a compressive wave traveling through a media faster than the media's speed of sound [28]. The shock wave can also be described as a compression wave, which is a longitudinal wave propagated by the elastic compression of the medium [29]. The near vertical front of the shock wave causes the material, through which the wave is traveling, to "jump" from an unshocked state to shocked state, as illustrated in Figure 2.1.

Shock waves have been studied by observing explosives detonating in various environments, such as in open air and shock tubes. Though the mechanisms of shock wave

generation are different, the characteristics of the shock waves produced by these mechanisms remains the same. The shock wave is a complex phenomenon composed of numerous characteristics; however, only the pertinent characteristics to this research will be discussed. These characteristics are jump conditions, attenuation wave, pressure wave, shock velocity, and reflections. These characteristics were chosen, because they are needed to understand how the shock wave interacts with the brain and the surrounding environment. The jump condition characteristic describes how the shock wave causes a discontinuity of the material as the shock wave moves through the material, as shown in Figure 2.1. As the shock wave moves through the material, the material goes from an unshocked state to a shocked state resulting in increased pressure, density, and other internal material properties. These changes occur almost instantaneously as the shock front moves through the material. This type of loading is known as dynamic loading, as the load is applied rapidly over time.
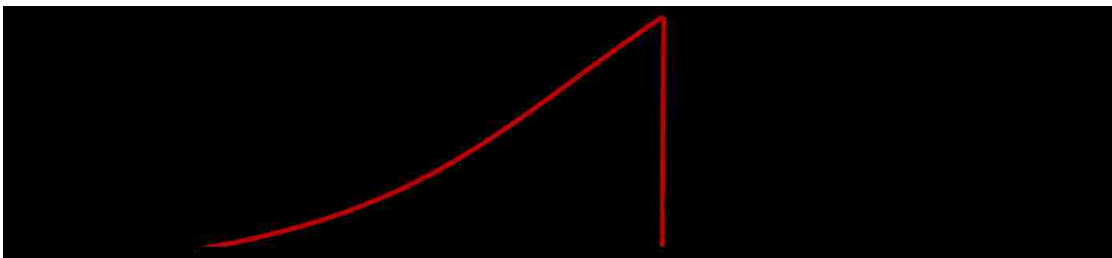
Figure 2.1. Shock front moving through a material, adapted from Cooper [28]

As the shock wave moves through the material, a pressure wave is formed and travels behind the shock front. A pressure wave is "a wave in which the propagated

disturbance is a variation of pressure in a material medium" [30]. The pressure wave is measured to understand how the shock wave affected the material and has several characteristics as well. A defining characteristic of a pressure wave is the occurrence of a positive phase and a negative phase, as shown in Figure 2.2. The positive phase is relative to the compression wave of the shock wave, as the pressure nearly instantaneously rises from ambient pressure to peak pressure, shown in Figure 2.2b. The negative phase is the region of negative pressure associated with the rarefaction wave, as shown in Figure 2.2c. The rarefaction wave is "the progression of particles being accelerated away from the compressed or shocked zone" [28]. The negative phase only occurs some distance away from the point of origin. The negative phase is observed initially at minimum distance of roughly one-tenth the scaled distance and exponentially increases to roughly one scaled distance, where it plateaus [28, 31]. Scaled distance is a factor relating explosive blasts with different charge weights of the same explosive at various distances and calculated by Equation (1) [28, 32].
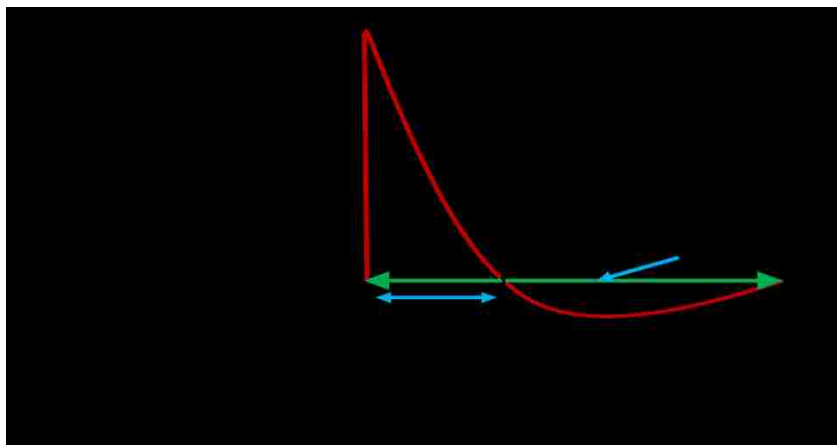
Figure 2.2. Characteristics of a shock wave a. ambient pressure b. positive phase c. negative phase d. return to ambient pressure, adapted from Cooper [28]

$$Scaled\ distance = distance/\sqrt[3]{weight\ of\ explosives} \qquad (1)$$

An exaggerated illustrative representation of a shock wave on a house can be seen in Figure 2.3. The ambient pressure before the shock wave passes through is represented by 2.3*a*. The positive phase, the "push", of the shock wave is represented by 2.3*b*. The negative phase of the shock wave, the "pull" to fill the vacuum, is represented by 2.3*c*. The return to ambient pressure after the passage of the shock wave is represented by 2.3*d*. It must be noted that Figure 2.3 is an extremely exaggerated illustration of the effect of a shock wave on a house. The air, however, does not experience damage when a shock wave passes through. The air experiences changes in pressure from the shock wave and returns to ambient pressure with little to no damage [31].
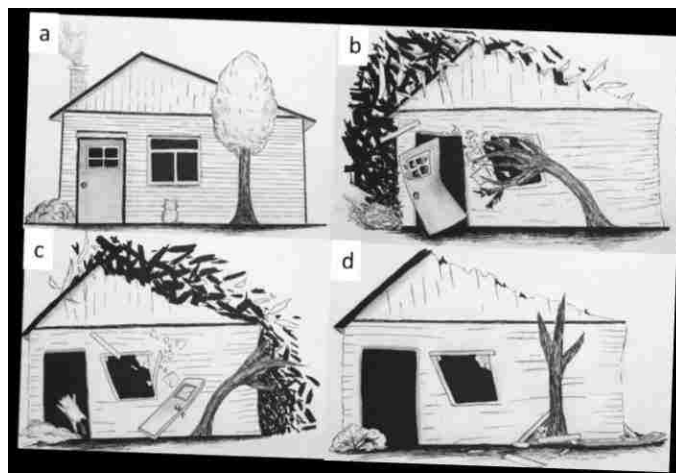
Figure 2.3. Illustration of a left going pressure wave a. ambient pressure b. positive phase c. negative phase d. return to ambient pressure, adapted from Kinney and Graham [31]

Each material's properties govern how the material responds to compression caused by the shock wave. In many cases, the shock wave causes the material to compress beyond its natural limits resulting in damaged regions. In some materials, the damaged regions can appear as spalling, when the tensile wave magnitude is greater than the tensile strength of the material [28]. The tensile wave increases the length of the material. The shock wave causes the compression of the material until the shock wave impacts a free surface (air). The shock wave reflects back into the material forcing the material into tension [33]. The attenuation wave occurs after the passage of the shock wave, and slowly relieves the material of the increased pressure and density.

As a shock wave moves through a medium, the particles in the medium are set into motion. The shock wave and particle velocities can be described by using Cooper's popsicle stick analogy [28]. Ten popsicle sticks are lined up with the width of the popsicle stick used as the distance between each of the popsicle sticks, as shown in Figure 2.4. For this analogy, the popsicle sticks are assumed to be five centimeters wide, thus the distance between the popsicle sticks is five centimeters. The left most popsicle stick is then given a constant velocity towards the other popsicle sticks and contacts the tenth popsicle stick 15 seconds later. The first stick traveled 45 centimeters; therefore, the velocity was 3 centimeters per second. The sticks represent the particles in the medium, thus the particle velocity was 3 centimeters per second. Likewise, the velocity of the front of the popsicle can be calculated. The front of the stick traveled 90 centimeters in the same length of time resulting in a velocity of 6 centimeters per second, as shown in Figure 2.5. This higher velocity represents the velocity of a shock wave through a material. Thus, the shock wave would arrive before the particles in which the shock wave is traveling [28].
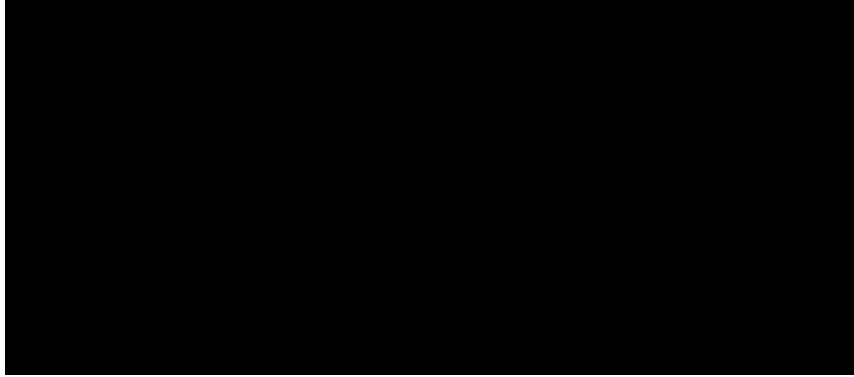
Figure 2.4. Ten popsicle sticks, adapted from Cooper [28]

Figure 2.5. Popsicle method to describe particle velocity and shock velocity, adapted from Cooper [28]

The attenuation wave slowly relieves the shocked material back to the ambient state, as shown in Figure 2.1. Unlike the jump condition, the attenuation wave is an exponential decay. The decay is the result of the attenuation wave traveling faster than the shock front. The attenuation wave has a higher velocity than the shock wave because the attenuation wave is traveling through material that is already in motion with a higher density after the passage of the shock front.

Pressure transducers and data acquisition systems (DAS) are used to measure and record the pressures produced by the passage of the pressure wave, respectively. The pressure transducers produce a voltage, which is converted to pressure by a unique calibration value. The pressure transducers are placed in either the reflective orientation or incident orientation. In the reflective orientation, the pressure transducer is placed facing the explosive, as shown in Figure 2.6a and measures the reflected pressure. Reflected pressure occurs when a shock wave impacts an object and produces a higher pressure [34]. In the incident orientation, the pressure transducer is placed facing 90 degrees to the blast, as shown in Figure 2.6b and measures the incident pressure. The pressures and time durations of the pressure wave recorded by these two sensor orientations vary greatly. The measured reflective peak pressures range from two to eight times higher than the incident pressures (overpressure) [35] and shown in Figure 2.7. Swisdak mathematically determined how reflective and incident pressures can be calculated from one another [35] as well as shock and particle velocities, as shown in Figure 2.7 and Equation 2,

$$P_r = 2P + (\gamma + 1)q \qquad\qquad (2)$$

where P_r is reflective pressure, P is incident pressure, γ is the ratio of specific heats of air

with average value of 1.4 below 1000 psi, and q is dynamic pressure. Equation (2) can be

rewritten to solve for P resulting in Equation (3).

$$P = \frac{P_r - (\gamma + 1)q}{2} \tag{3}$$

Due to the orientations recording drastically different values, the orientation of the pressure

transducer must be given in shock wave experiments.
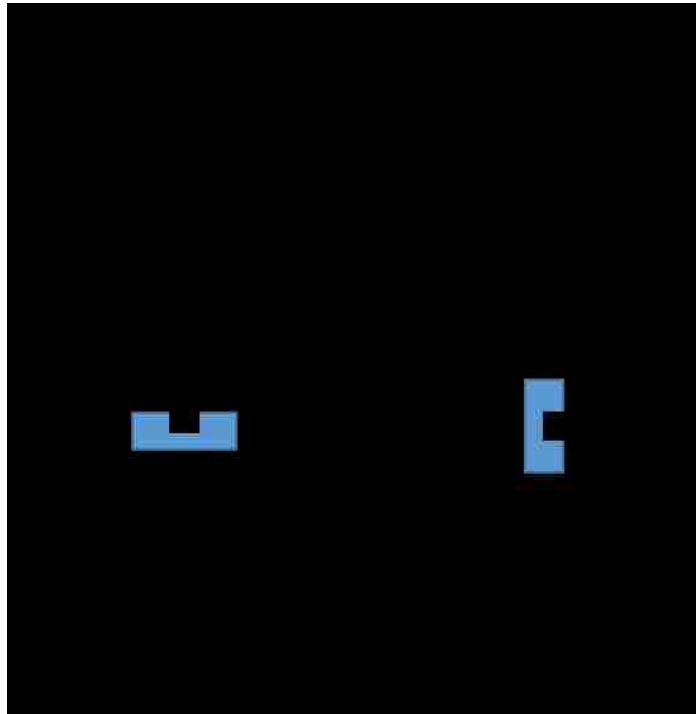
Figure 2.6. Pressure transducer orientation a. Reflective b. Incident

OVER PRESSURE (PSI)	SHOCK VELOCITY (FT/SEC)	PARTICLE VELOCITY (FT/SEC)	DENSITY RATIO	DYNAMIC PRESSURE (PSI)	REFLECTED PRESSURE (PSI)
1.0	1118.7	51.97	1.049	2.40 E-2	2.06
1.5	1134.2	76.89	1.073	5.38 E-2	3.13
2.0	1149.4	101.16	1.097	9.5? E-2	4.23
2.5	1164.5	124.81	1.120	.15	5.36
3	1179.4	147.89	1.143	.21	6.51
4	1208.7	192.42	1.189	.37	8.90
5	1237.2	235.00	1.234	.58	11.39
6	1265.1	275.79	1.279	.83	13.98
7	1292.4	314.98	1.322	1.11	16.68
8	1319.2	352.70	1.365	1.44	19.46
9	1345.4	389.08	1.407	1.81	22.34
10	1371.1	424.23	1.448	2.21	25.31
15	1493.1	584.53	1.643	4.77	41.45
20	1605.8	724.85	1.823	8.14	59.53
25	1711.2	850.51	1.988	12.22	79.33
30	1810.4	964.91	2.141	16.94	100.66
40	1994.2	1168.56	2.415	28.04	147.26
50	2162.5	1347.69	2.654	40.98	198.29
60	2318.7	1509.05	2.864	55.45	252.95
70	2465.1	1656.84	3.050	71.18	310.63
80	2603.3	1793.88	3.216	87.99	370.87
90	2734.5	1922.17	3.366	105.73	433.28
100	2859.8	2043.16	3.502	124.25	497.58
150	3418.7	2569.93	4.028	225.85	840.13

Figure 2.7. Overpressure to reflective pressure conversion chart with overpressure and reflective columns outlined, adapted from Swisdak [35]

There are two tools commonly used to estimate the incident and reflective pressures and impulses from an open-air detonation. The first tool is the Kingerly-Bulmash blast calculator from the United Nations (UN). The Kingerly-Bulmash calculator uses an equation developed from numerous explosive tests, of which hemispherical charges of TNT are the most common. The three parameters needed for the Kingerly-Bulmash calculator equation are explosive type, charge weight, and distance from the explosive [36]. The second tool is the Department of Defense Explosives Safety Board (DDESB) Blast

Effects Computer [37]. This calculator accounts for all of the same parameters as the UN

calculator, and also if the explosive is in a building, and if the explosive is enclosed in

something that could produce fragments upon detonation. The DDESB Blast Effects

Computer also gives a probability of eardrum rupture and lung damage from the explosive

detonation at the given distance.

Swisdak also observed that the overpressure of an explosive blast can be related to

the velocity of both the shock wave and particles in the medium [35]. If the overpressure

(incident pressure) is known, the velocity of the shock wave can also be determined. The

velocity could be determined in two manners. The first manner interpolates the value

between two given pressures, shown in Figure 2.7. The second manner uses Equation (4)

to calculate velocity,

$$U = C_0 \left(1 + \frac{\gamma + 1}{2\gamma} * \frac{P}{P_0} \right)^{1/2} \tag{4}$$

where U is shock velocity, C_0 is ambient speed of sound, γ ratio of specific heats of the

medium with 1.4 average value below 1000 psi, P peak overpressure, and P_0 is ambient

pressure.

2.1.2. Impulse. The area under the curve in a pressure versus time graph as

depicted in Figure 2.8, is impulse. The oscillating pressure after the negative phase in

Figure 2.8 is not considered for the calculation of impulse. The oscillations are the result

of the air returning to ambient pressure.
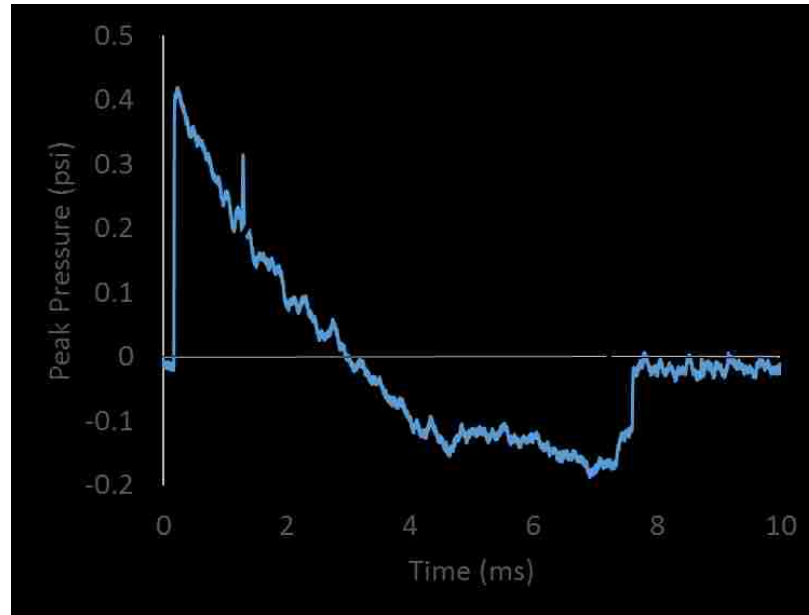
Figure 2.8. Example of experimental pressure trace taken 60 ft. from a 70 g C4 spherical charge

Impulse can be calculated with two different techniques. The first technique is to calculate the impulse between the time of arrival and the return to ambient pressure. This technique results in higher impulse due to all the changes in pressure being accounted for; however, this technique was not used in this research because this method is not used in majority of bTBI research. The other technique calculates impulse between the time of arrival of the shock wave and the end of the positive phase. For both impulse calculation techniques, the midpoint approximation method is used, as shown in Equation (5);

$$I = \int_{t_0}^{t_+} P(t) = \sum_{i=t_0}^{t_+} \left(\frac{P_i + P_{i+1}}{2}\right) * (t_{i+1} - t_i) \qquad (5)$$

where I is impulse, t_0 is time of arrival, t_+ is end of positive phase, P(t) is pressure as a function of time, P_i is pressure at specified time, and t_i is time at given i value. The midpoint approximation method can also be simplified to Equation (6),

$$I = \sum_{i=A}^{j} (y_i) * \Delta t \qquad (6)$$

where A is the initial value, y_i is change in pressure, and Δt is the change in time [38]. Both Equations 3 and 4 take the average of the peak pressures at the specified time values, multiply them by the change in time, and are summed over the duration of the positive phase.

The data acquisition software can also calculate impulse using Equation (5). The Hi-Techniques Synergy Data Acquisition System [39] can calculate impulse in two different methods. The first method (integral) accounts for all changes in pressure over the time interval under review [38]. The second method (ac-integral) is similar to the first, but subtracts the mean value of the data before the summation to remove small variations in the data. These small variations can greatly affect the calculated impulse, thus should be used if no changes or offsets in the data are expected in the signal are expected [38].

2.1.3. Friedlander Equation. In 1946, Friedlander published a series of calculations that resulted in an equation to describe how an incident sound wave travels parallel to a wall [40], which was based off of Taylor's previous work on blast waves [41].

This equation describes how the sound wave pressure exponentially decayed as it traveled past the wall. Friedlander's equation was found to be representative of an open-air surface explosive detonation in the 1940s with the advent of piezo-electric transducers and amplifiers [34, 42, 43]. However, the Friedlander does not account for reflections off the ground or surrounding materials. The equation only requires the peak overpressure, P_s, time of arrival, t, and the total positive phase time duration, t^+, shown in Equation (7) and Figure 2.9.

$$P = P_s e^{\left(\frac{-t}{t^+}\right)}\left(1 - \frac{t}{t^+}\right)$$
(7)

The impulse of the pressure wave could be calculated by integrating Equation (7) with respect to time, resulting in Equation (8).

$$I = \frac{P_s t^+}{e} = 0.368 P_s t^+$$
(8)

Many of the properties of the Friedlander equation were initially developed and described by Thornhill [44]. Thornhill also introduced a constant modifier, α, to Equation (7)

resulting in the modified Friedlander equation given in Equation (9) and when integrated,

Equation (10), to describe different decay rates of various shock waves [34, 43, 44].

$$P = P_s e^{-\alpha \frac{t}{t^+}} \left(1 - \frac{t}{t^+} \right) \tag{9}$$

$$I = \frac{P_s}{\alpha^2\, t^+} \left(e^{-\alpha t^+} - 1 + \alpha\, t^+ \right) \tag{10}$$

Dewey later clarified that the Friedlander equation was valid up to one atmosphere and the

modified Friedlander equation was valid up to seven atmospheres [42].
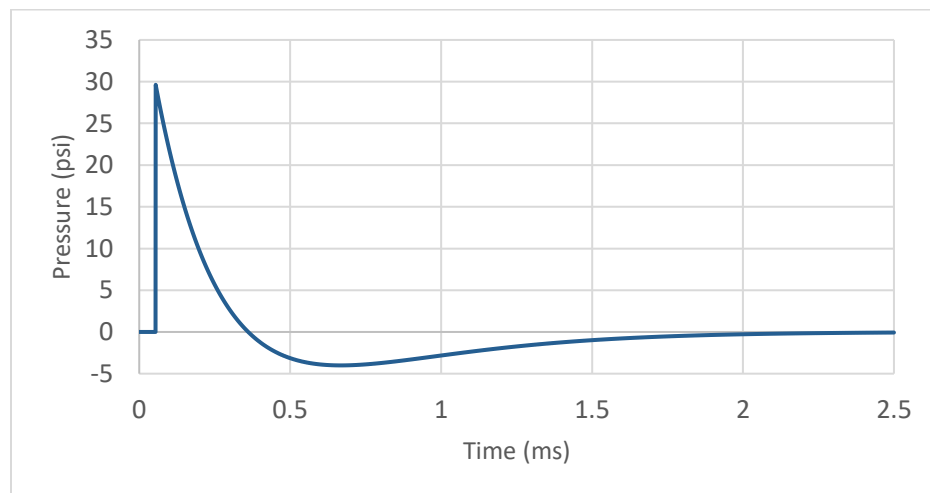
Figure 2.9. Example of Friedlander curve with 29 psi peak pressure and 0.3 ms duration

2.1.4. Shock Tubes. A shock tube is an instrument used to simulated an open-air explosive blast by focusing the shock wave's energy down the length of the tube [45]. A result of the focusing of shock wave energy, shock tubes can produce pressure traces that are very repeatable and similar to the Friedlander waveform. As a result, researchers studying how the brain responds to explosive loading use a shock tube to produce the shock wave. However, the resulting shock wave's duration is longer than in open-air testing. Shock tubes can either be explosively driven or gas driven [46]. For explosively driven shock tubes, explosives are used to generate the shock wave and uses less explosives than open-air. Depending on the design of the experiment, the shock tube can be composed of either one continuous tube or numerous sections [47]. The shock tube sections are used to confine the explosive energy and can gradually increase in diameter to accommodate the animal subject.

For gas driven shock tubes, a diaphragm separates the high-pressure section and the low-pressure section. The high-pressure section is filled with gas to the desired pressure for the experiment, whereas the low-pressure section is open to the ambient air. For a majority of experiments, the diaphragm ruptures when the desired pressure is reached in the high-pressure section. Few experiments use diaphragms that need to be manually punctured [48]. Once the diaphragm ruptures, a shock wave is produced, travels down the length of the tube, and exits the shock tube. The wide use of gas driven shock tubes to produce the shock wave has resulted in inconsistencies with the results made in the academic world [49–51]. Reneer et al. [52] tested compressed air, compressed helium, oxyhydrogen, and RDX to determine if the compressed gasses produced a similar pressure wave profile to the RDX. The compressed air did not fit the pressure profile of the RDX,

whereas compressed helium and oxyhydrogen did resemble the RDX pressure trace [52]. Gas driven shock tubes are accepted because the shock waves can be replicated quite well and do not require the use of explosives.

The progression of the shock wave in an explosively driven shock tube is similar to an open-air blast; however, the positive phase time duration and the rise time are longer due to the shock wave being confined and reflecting off of the walls of the shock tube. Rise time is the amount of time between the arrival of the shock wave and the time of peak pressure. The shock tube confines the shock wave generated during the detonation process resulting in reflected shock waves [53]. In an open-air blast, when the explosive is detonated, the resulting shock wave expands spherically and unimpeded from the explosive, as shown in Figure 2.10. When the same amount of explosive is placed in a shock tube, the shock wave expands spherically and at the same velocity as open air, until it encounters the walls of the shock tube [54, 55]. The shock wave then reflects off the walls of the tube, resulting in the shock wave's energy being confined and focused down the length of the tunnel, as shown in Figure 2.10.
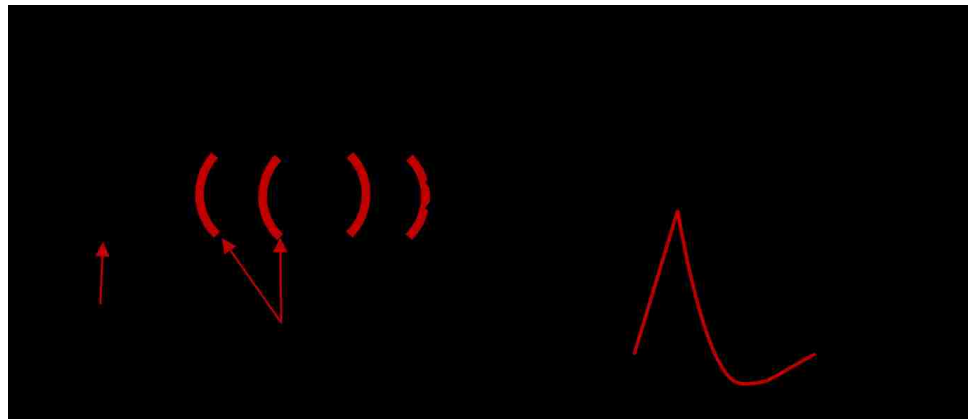
Figure 2.10. Comparison of open-air and explosively driven shock tube pressure trace

The passage of a gas driven shock wave is similar to the explosively driven shock wave; however, the generation of the shock wave is much different. The shock wave is generated by the rupturing of the diaphragm, which separates the high and low-pressure sections. The shock wave then travels down the low-pressure section of the shock tube, as shown in Figure 2.11. The resulting pressure trace can be similar to the explosively driven shock tube or vastly different, as noted by Reneer et al. [52]. Due to the reduced cost and the high repeatability, gas driven shock tubes have been widely used for blast induced TBI research.
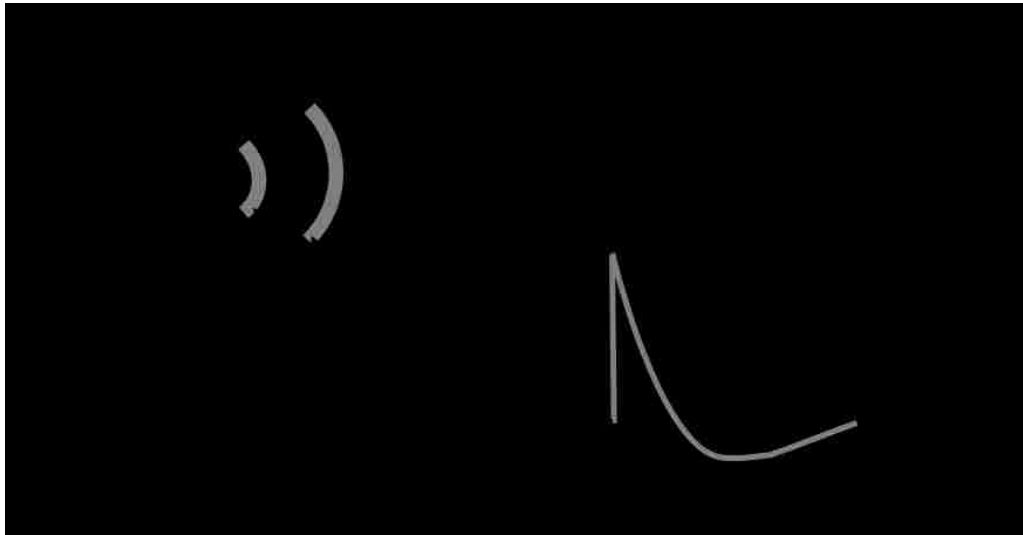
Figure 2.11. Gas driven shock tube pressure trace

Numerous studies have been conducted to understand the behavior of a shock wave at the exit of shock tubes [24, 25, 27, 49, 56–60]. Through these studies, it has been found that the pressures and durations exiting the end of the shock tube are greater than those

observed for open air explosive detonations represented by the Friedlander equation. These sustained pressures and longer positive phase durations result in the jet wind [25], also known as exit jet [49], effect. The jet wind is the result of vortices forming behind the shock wave as it exits the shock tube, as shown in Figure 2.12. Henkes and Olivier observed a nearly straight secondary shock wave caused by the expansion of hot gases exiting the shock tube [57]. Duan et al. also observed a similar phenomenon and determined the phenomenon was a Mach disk [59]. The surrounding energy and particles are redirected by vortices resulting in sustained low pressure over an extended time duration. The vortices are formed for simple geometry shock tubes, such as rectangular prisms and cylinders.
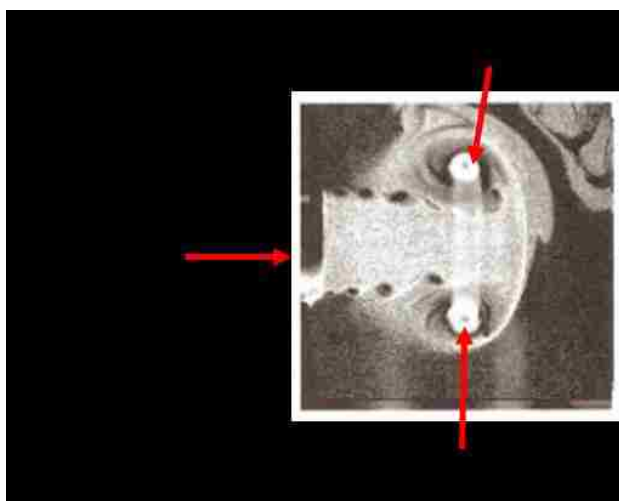
Figure 2.12. Vortices formed at shock tube exit after the passage of the shock wave [27]

When shock tubes are used to conduct bTBI research, a number of parameters must be reported so that the results can be properly compared to other published studies. The parameters that must reported are location of animal subject relative to the source of the

shock wave, diameter, and length of shock tube [61]. Each parameter is important because the resulting shock wave and brain injury are affected by any minor change in these parameters.

The initial parameter in animal bTBI research to be reported is the location of the animal. The three commonly used locations are in the center of the shock tube, at the exit, and a short distance from the exit [49, 61]. The Friedlander equation was found to be representative of shock waves for centrally placed animal specimens [23, 62]. However, the Friedlander equation does not describe the shape of shock waves measured outside the shock tube [23, 25, 62]. Giannuzzi et al. found that the pressures exiting a shock tube do not decay immediately, but remain "stagnant" for a distance similar to the diameter of the shock tube [26]. For the locations outside the shock tube, the shock wave will not be representative of an open-air test. Chandra et al.'s [25] experimental and simulation research found two differences between open air testing and a rectangular gas driven shock tube. The first difference observed was a secondary peak in the pressure trace, as shown in Figure 2.13A. The researchers determined that this second peak was due to reflections off the walls of the shock tube. The second peak was observed only by the sensors located within the tube and the first sensor outside the tube [25]. The second difference observed was the extended positive phase duration in the simulation and experimental results. This discrepancy in time duration was the result of the confinement of the shock tube and termed "jet wind", as shown in in Figure 2.13B.

A jet wind is the result of the rarefaction wave and low-pressure vortices at the exit of the shock tube. The vortices redirect some of the shock wave energy and surrounding air resulting in extended low pressure and long duration across the end of the open shock

tube (Figure 2.13) [25, 27, 63, 64]. Due to the Bernoulli Effect, the distance between the shock front and vortexes is shorter than the shock tube diameter. The particle velocities were higher in the jet wind than the shock front resulting in shorter time duration for pressures measured all distances (26, 103, 229, 391, and 596 mm) measured from the end of the open shock tube [25]. The placement of the animal subject influences the loading on the brain and affects the other two parameters. As a result, placement of the animal subject is an important parameter.
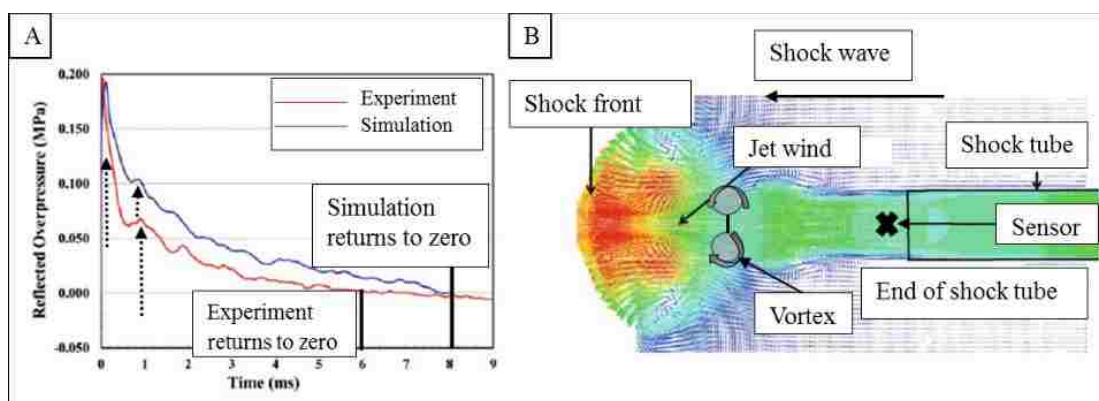
Figure 2.13. Jet wind effect: A-Sample of Chandra et al.'s data with pressure peaks denoted by dashed arrows B-Illustration of the jet wind with represent velocities with 'X' denoting location of pressure sensor, adapted from Chandra et al. [25]

The second parameter in animal bTBI research to be considered is the diameter of the shock tube. For animals placed inside the shock tube, the diameter must be large enough that the cross-sectional area of the animal's body does not occupy more than 20% of the cross-sectional area of the shock tube to reduce dynamic pressures that the animal is subjected to [49, 65, 66]. For animals placed outside the shock tube, the 20% cross-

sectional area does not apply allowing for the smaller diameter tubes to be used. The minimum diameter of the tube is the diameter of the animal subject's head. Overall, the diameter of the shock tube is a key parameter that must be considered if shock tube testing is to be conducted.

The third parameter in animal bTBI research to be considered is the length of the shock tube. The recommended minimum length for the shock tube is between three to ten times the diameter of the shock tube, which allows the shock wave to become planar [61, 67, 68]. A planar shock wave is desired because uniform pressure will be applied across the animal's head. The diameter of the shock tube and the desired peak pressure of the shock wave must be taken into account when determining the length of the shock tube.

Explosively and gas driven shock tubes are effective tools to produce repeatable shock waves in animal bTBI testing. Three parameters that should be reported for both types of shock tubes are location of animal subject, diameter, and length of the shock tube. Overall, shock tubes are useful in animal bTBI testing and can simulate open air testing.

2.1.5. TNT Equivalency. An equivalency tool for explosives was developed to compare the strengths between various different types of explosive. Trinitrotoluene (TNT) was chosen as the standard, due to TNT being one of the oldest and most well studied explosives [69]. Different equivalency equations have been developed to compare various explosive properties. All of these TNT equivalency equations are used to determine the equivalent weight of another explosive to the weight of TNT [28, 70].

Three equivalency equations are commonly used to determine the equivalent weight of explosives. The first TNT equivalency relates the explosive's available energy to work to that of TNT, as shown in Equation (11) [28],

$$\text{wt(TNT equivalent)} = \frac{wt(HE) * E_{exp}(HE)}{E_{exp}(TNT)} \qquad (11)$$

where wt is weight, HE is high explosive, and E_{exp} is the available energy of the explosive

to do work. The second equivalency equation relates the detonation velocities of the high

explosive to TNT, as shown in Equation (12) [28],

$$TNT\ equivalent = \frac{D^2(HE)}{48.3} \qquad (12)$$

where D is the detonation velocity in km/s and 48.3 is this the detonation velocity of TNT

squared with a density of 1.64 g/cm^3. This equation was used in this research to determine

the equivalent amount of explosives. The third equivalency relates the gas production of

the high explosive to TNT and was developed by Berthelot [28, 71, 72]. The Berthelot

method is shown in Equation (13),

$$\%(TNT\ equiv) = \frac{840 * \Delta n * (-\Delta H_R^0)}{(FM)^2} \qquad (13)$$

where Δn is the number of moles of gas produced per mole of high explosive, ΔH_R^0 is the

molar heat of detonation (kJ/mole), and FM is the molecular weight of the explosive. The

values for the Berthelot method variables can be found in numerous reliable sources, such

as: *Explosives Engineering* [28], Lawrence Livermore National Laboratory (LLNL) [73], and National Center for Biotechnology Information [74]. The Berthelot equation was used to calculate the gas production of the pentolite explosive, because all other values were known.

2.1.6. Pressure-Impulse Graphs. Another tool used to describe the destructive power of an explosive is a pressure-impulse (P-I) graph. A P-I graph visually shows the regions where damage is likely to occur to either a building [75–77] or a human [14] after the detonation of an explosive. The P-I curve is a combination of two asymptotic lines connected by a curve, which is the dynamic region. The dynamic region failure is dependent upon both the peak pressure and impulse of the shock wave [78]. The line separating the non-damaged region from the damaged region is the P-I curve, as shown in Figure 2.14. The asymptotic lines and dynamic region are determined by the use of experimental testing, simulations, or a combination of testing and simulations. Every structure has its own unique P-I curve to denote the line between no damage to severe damage. P-I curves have been developed for buildings with reinforced concrete columns [79], human lungs [80], and human eardrums [81]. Some P-I graphs differentiate the different severities of damage. One of the first published instances of a P-I graph was from an analysis of an elastic single degree of freedom model by Mays and Smith [14].

P-I graphs can also be used to denote the areas more sensitive to pressure, impulse, or both [82], as shown in Figure 2.14. In the pressure sensitive region, the structure is more likely to be damaged when the minimum pressure is exceeded, with little regard to the impulse. The same trend is observed for the impulse sensitive region, as long as the pressure is above the minimum. For the dynamically sensitive region, both the pressure

and impulse must be above the minimum values. The dynamically sensitive region can also be defined by an equation. These three regions have been termed "close in" for impulse sensitive loading, "far-field" for pressure sensitive region, and "near-field" for the dynamically sensitive region [83, 84]. Near field is any distance within ten times the charge diameters length [85]. Close in is any distance below 20 times the charge diameter [86]. Human P-I graphs for lungs and eardrums have been developed and discussed in more detail in Sections 2.3.1 and 2.3.2, respectively.
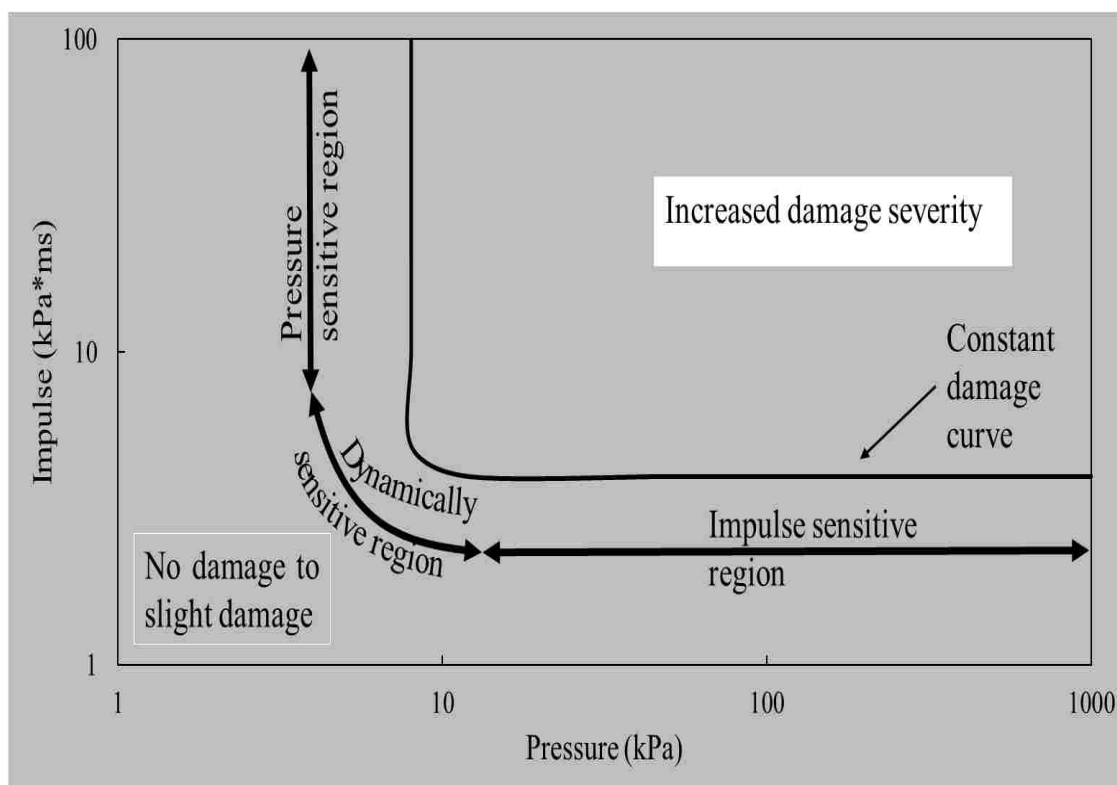
Figure 2.14. Typical P-I curves for structures with sensitivities labeled, adapted from Krauthammer et al. [87]

2.2. PRESENT bTBI DATA AND SCALING METHODS

This section discusses the animal bTBI data used and two animal scaling methods.

2.2.1. bTBI Testing. Numerous studies have been conducted to understand how bTBIs affect the brain. A majority of these studies expose small mammals, such as rats and mice, to a shock wave of varying strengths, durations and evaluating the animals for bTBIs. There are two main types of tests conducted to mimic an explosive blast experienced by a service member or civilian after an improvised explosive device detonates. These types are open air and shock tube, as discussed in Section 2.1.

Before a human bTBI P-I graph could be generated, several online search engines were used to find animal bTBI studies. The primary search engines used were Google Scholar, Scopus, and PubMed. For each of the search engines, the following terms were used: "traumatic brain injury", "open air", "shock tube", "blast", "bTBI", and "impulse". The results from the searches in Google Scholar, Scopus, and PubMed were approximately 5,000, 135, and 75 results, respectively. From those, all references that reported test type, sensor orientation, peak pressure, time duration, model, and animal location were used and given in Table 2.1. The first author column gives the last name of the first author of the article and the reference. The test type column states if the tests were conducted in open-air or with a shock tube. The model denotes the species of animal used: mouse, rat, goat, or pig. The sensor orientation indicates whether incident or reflective pressure were reported. The reported peak pressure, impulse, duration, and severity columns list the given values in each article. As observed in Table 2.1, the reporting of bTBI results is varied and can lead to incorrect assumptions, as noted by Needham et al [49], Panzer et al. [50], and Beamer et al. [51].

Table 2.1. Data considered for proposed P-I curve

First Author	Test type	Model	Sensor Orientation	Reported			
				Peak Pressure (kPa)	Impulse (kPa*ms)	Duration (ms)	Severity*
Song [88, 89]	Open Air	Mice	Incident	19.3 to 581	2.89 to 70.3	0.568 to 3.54	M
Pun [90]	Open Air	Rats	Incident	77.3 & 48.9	-	18.2 & 14.5	M
Chen 1 [91]	Open Air	Goats	Incident	41 to 703	-	0.442 to 5.90	-
Li [92]	Open Air	Goats	Incident	45 to 913	-	0.0663 to 2.7	-
Saljo 1 [93]	Open Air	Pigs	Incident	9 to 42	-	1.5 to 5	M
Chen 2 [94]	Open Air	Pigs	Incident	420 & 450	-	3.42 & 4.2	M
Beamer [51]	Shock Tube	Mice	Incident	202 to 456	41 to 160	0.61 & 0.108	M to Mod
Wang [48]	Shock Tube	Mice	Reflective	64 to 918	-	3 to 4	-
Kabu [95]	Shock Tube	Rats	Incident	313 to 839	-	2 & 4	M to S
Turner [96]	Shock Tube	Rats	Reflective	216 to 621	-	2	-
Risling [97]	Shock Tube	Rats	Incident	136 & 236	-	1 & 2	M
Pham [98]	Shock Tube	Rats	Incident	100 to 214	-	7.5	-
Kochanek [99]	Shock Tube	Rats	Incident	241	-	4	M
Budde [100]	Shock Tube	Rats	Incident	39 & 110	-	0.34 & 0.46	-
Reneer [52]	Shock Tube	Rats	Incident	120	175 to 275	3.5 to 5.5	M
Kawoos [101]	Shock Tube	Rats	Incident	72 & 110	150 &320	5.1 &7.1	-
Sawyer [102]	Shock Tube	Rats	Incident	103 to 203	204 to 456	5.8 to 7.6	-
Skotak [103]	Shock Tube	Rats	Incident	127 to 288	184 to 452	-	-
Long [104]	Shock Tube	Rats	Incident	114 to 147	-	3.5	-
Svetlov [105]	Shock Tube	Rats	Incident	110 to 358	-	1 to 10	-
Garman [106]	Shock Tube	Rats	Incident	241	-	4	M
Kuehn [107]	Shock Tube	Rats	Incident	262 to 1372	-	3	-
Saljo 2 [108]	Shock Tube	Rats	Incident	154 & 240	-	1.7 &2	-
Shridharani [109]	Shock Tube	Pigs	Incident	107 to 741	87 to 869	-	M

Note: * M – mild, Mod – moderate, S – severe

2.2.2. bTBI Scaling. Different methods have been used to scale animal bTBI injury and lethality curves to humans. Common methods are mass scaling and brain scaling. Mass scaling scales the entire body from one animal to another. Brain scaling only scales the mass of the brain. When scaling is conducted improperly from animals to humans, the data can be off by orders of magnitude [49]. For example, when the blast is not scaled down to the animal subject before experimentation, a mouse subjected to a 1 millisecond blast could equate to 13 milliseconds for a human [49].

2.2.2.1 Mass scaling. Bowen et al. [10] published a mass scaling equation based on a large number of animal lung injury data. The mass scaling equation scales the duration of the shock wave between different animal species, as shown in Equation (14),

$$t_{scaled} = (\frac{m_{scaled}}{m_{baseline}})^{1/3} t \qquad (14)$$

where m_{scaled} is the mass of humans, $m_{baseline}$ is the mass of test subject, and t is positive phase time duration. The one third power of mass comes from the one third power scaling for shock waves in air [28], as discussed in Section 2.1.1 and Equation (1). The mass scaling equation has been found to accurately predict lung damage [10, 110]. Rafaels et al. [13] conducted bTBI testing on rabbits and developed a pressure scaling equation from the data. Rafaels et al.'s proposed equation was a modification of the mass scaling equation

and. hypothesized that the brain sustained injury in the same manner as the lungs resulting in Equation (15),

$$P_{incident} = P_0(1 + a\Delta t^{-b}) \qquad (15)$$

where t is positive time duration and P_0, a, and b are experiment-fitting constants. Zhu et al. [11] conducted similar research on rats and found that the brain responded different to shock loading than lungs. Zhu et al. modified the values of variables a and b so that the bTBI P-T curve and lung injury P-T curve intersected. The bTBI P-T graph Zhu et al. produced did not account for impulse, which can vary between different experimental setups. Neither the Rafaels nor Zhu's equation accounted for the properties of the head of the animal.

2.2.2.2 Head scaling. Jean et al. [12], henceforward referred to as Jean, published a paper that proposed a different scaling method. Unlike Rafaels et al. and Zhu et al. equations, Jean's proposed scaling method accounts for all the major structures of the animal's head: brain, skull, and surrounding soft tissue. Jean's work was based on advanced computational models of a mouse, pig, and human. Jean proposed the scaling parameter that accounted for major characteristics of the head in Equation (16),

$$\eta^s = \frac{c_{brain}m_{brain}^s}{c_{skull}m_{skull}^s + c_{flesh}m_{flesh}^s} \qquad (16)$$

where c is speed of sound in the material, s is the species, and m is the mass of the material [12]. This accounts for the changes in intracranial pressure when the head is subjected to an incident shock wave. Jean assumed that the intracranial pressure threshold is normalized and invariant across species. Jean also assumed that the speed of sound for the brain, skull, and flesh were the same across all species. The resulting scaling factor was given as Equation (17),

$$p_{incident}^{h} = p_{incident}^{s} \left(\frac{\eta^{s}}{\eta^{h}}\right)^{\alpha} + \frac{B}{A}[1 - \left(\frac{\eta^{s}}{\eta^{h}}\right)^{\alpha}](P_{amb}) \qquad (17)$$

where α, A, and B are fitting parameters , p^{s} is incident-normalized overpressure that results in injury, η^{s} is the tested animal, and η^{h} is the human. Equation (16) is used to calculate the values for both the tested animal and humans. The values of α, A, and B were 0.48, 15.3, and 3.13, respectively. In Equation (17), p^{s} can be replaced with Equation (15) resulting in Equation (18). To illustrate the use of Equation (18), Jean inserted the parameters of the 50% survivability curve from Rafaels' work into Equation (18). The mass scaling curve was found to be 106% of the rabbit; whereas, Jean's proposed method estimated human survivability curve was 72% of the rabbit. By this comparison, Jean's method is more conservative than other scaling methods [111, 112].

Jean's method will be used to scale the different animal species given in Table 2.1, as it is the most conservative and accounts for the characteristics of the head. The characteristics of mice, rats, goats, pigs, and humans required for Equation (16) are

given in Table 2.2 along with the reference in parenthesis. Wherever possible, the masses of the brain, skull and flesh were found in the literature. The values not explicitly given will be calculated in Section 4.

$$p_{incident}^{h} = P_0(1 + a\Delta t^{-b})\left(\frac{\eta^s}{\eta^h}\right)^{\alpha} + \frac{B}{A}[1 - \left(\frac{\eta^s}{\eta^h}\right)^{\alpha}](P_{amb}) \qquad (18)$$

Table 2.2. Parameters for Equation (17) for selected species

Species	Brain, g	Skull, g	Flesh, g	c_{brain}, m/s	c_{skull}, m/s	c_{flesh}, m/s	η^s
Mouse	0.41 [12]	0.74 [12]	1.876 [12]	1,549 [12]	2,295 [12]	1,778 [12]	0.126 [12]
Rat	2 [90]	3.19 [113]	-	1,549 [12]	2,295 [12]	1,778 [12]	-
Goat	115 [114]	179.5 [115]	1455.5 [114]	1,549 [12]	2,295 [12]	1,778 [12]	-
Pig	151.3 [12]	948.9 [12]	4186 [12]	1,549 [12]	2,295 [12]	1,778 [12]	0.024 [12]
Human	1573 [12]	705.6 [12]	918.1 [12]	1,549 [12]	2,295 [12]	1,778 [12]	0.75 [12]

Jean's equation finds that humans are more susceptible to brain injuries than other animals. As shown in Table 2.2, humans have less skull and less surrounding soft tissue resulting in the shock wave not being attenuated. The snout and elongated skull of other mammals attenuates the shock wave resulting in the animals being able to endure a larger pressures before injury occurs. Jean's equation will be used in scaling animal bTBI data to humans, as the resulting values are more conservative than the mass scaling. For example, mouse to human results in 0.168, thus lowering the threshold for brain injury in humans.

2.3. HUMAN BLAST INJURIES

If precautions for safe distance and personal protective equipment are not available, animals and people can be injured when an explosive detonates, where the most susceptible organs to blast injury are the air containing organs: lungs, ears, and bowels [13, 116–118]. Eardrum rupture and lung damage can be physically observed unlike damage to the bowels. Eardrum rupture is observed from discharge from the ear canal and hearing loss [119] Lung injury observable symptoms are labored breathing, coughing, coughing up blood and chest pain [120]. Due to the observability of eardrum rupture and lung damage, numerous studies have been conducted to determine the peak pressures and durations that would result in injury or death. These properties will be discussed in further detail in the subsequent subsections.

2.3.1. Lung Damage. Numerous animal studies have been conducted to determine the lethality range for lung damage as a result of a blast incident [10]. Bowen et al. [10] concluded that lung injury was directly proportional to the mass of the specimen. Thus, mass scaling equations (Equations (15 and (14) were developed to estimate a 70 kg human's tolerance to an explosive blast. The results were plotted on a P-T diagram with threshold for injury, 99%, 90%, 50%, 10%, and 1% survivability curves plotted. For example, a child has a lower lung injury threshold than an adult [81]. Since the orientation of the specimen to the blast effects the lung injury curves, P-T graphs have been produced for each of the various orientations. For example, Courtney and Courtney examined how a 70 kg person in the incident orientation was affected by the shock wave [110], as shown in Figure 2.15 based upon Bowen et al.'s work [10]. These thresholds will increase for animals and humans with some sort of lung protection, such as a protective vest [61].
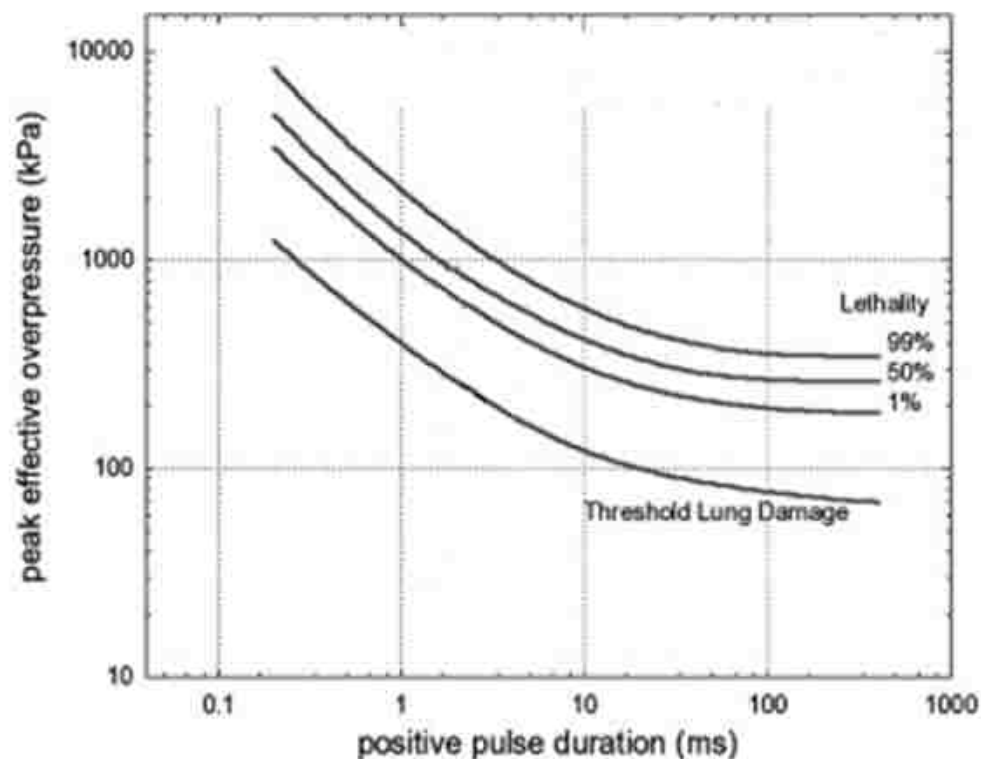
Figure 2.15. 70 kg man lung lethality curves adapted from Courtney and Courtney [110]

Baker et al. [80] produced a P-I curve for 50% lung lethality, shown in Figure 2.16. This P-I graph was produced from Bowen et al. and White et al.'s [10, 121] pressure and impulse points, as shown in Table 2.3. The 50% lung lethality curve is applicable to all people in an incident orientation to the blast as long as ambient pressure in Pascals and mass of the subject in kilograms are known.

An individual can sustain both a bTBI and a lung injury from the same blast. As a result, the bTBI can exacerbated due the reduced amount of oxygen in the blood [122, 123]. Therefore, lung injury curves should be plotted on a human bTBI P-I graph to determine if the TBI is exclusively from the blast. The lung injury could be observed before the brain injury; thus, the individual can receive appropriate treatment.
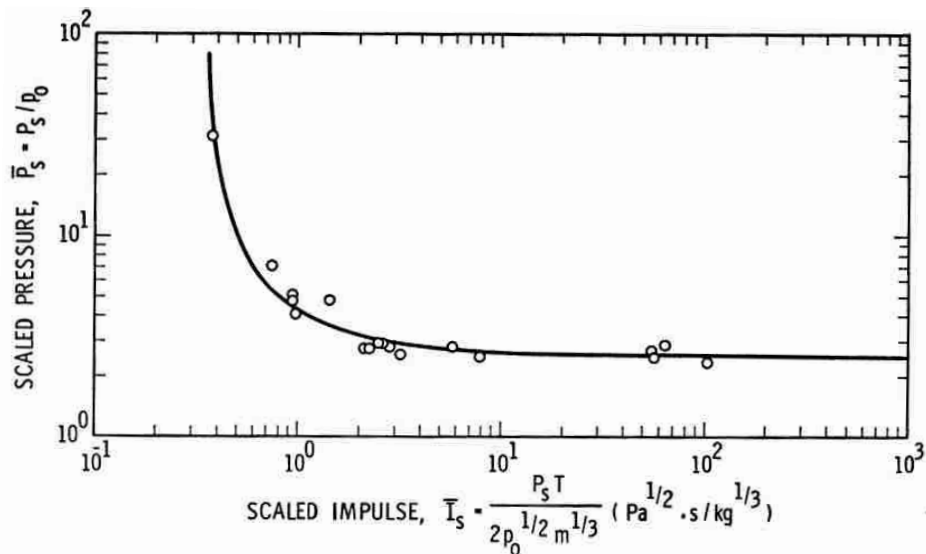
Figure 2.16. 50% lung survival pressure versus impulse curve from Baker et al. [80]

Table 2.3. Data points in Figure 2.16, adapted from Baker et al. [80]

Scaled Peak Pressure	Scaled Impulse		Scaled Peak Pressure	Scaled Impulse
2.35	100.66		4.95	0.953
4.8	1.4		2.9	2.53
2.8	28.23		2.8	5.79
4.1	0.97		2.85	64.02
2.9	2.5		2.65	55.88
2.75	2.27		32	0.378
2.55	3.21		7	0.749
2.5	7.92		2.75	21.87
2.49	57.58		2.3	10.86

2.3.2. Eardrum Rupture. Eardrums vibrate as sound enters the ear canals and ruptures when vibration limits are exceeded [81]. For an explosive blast, eardrum rupture occurs when the thresholds of minimum peak pressure and impulse are exceeded [81], as shown in Figure 2.17. If the sound wave has a very fast rise time, such as a normal rise

time for an explosive shock wave, Hirsh determined that the threshold was 34.5 kPa (5 psi) [124], which was also supported by White over a range of time durations [125]. Once the pressure is reached, the eardrum will rupture at any time interval, which is the cause of the horizontal lines in Figure 2.17. Hirsh also determined the 50% eardrum rupture occurs at 103 kPa (15 psi) [126].
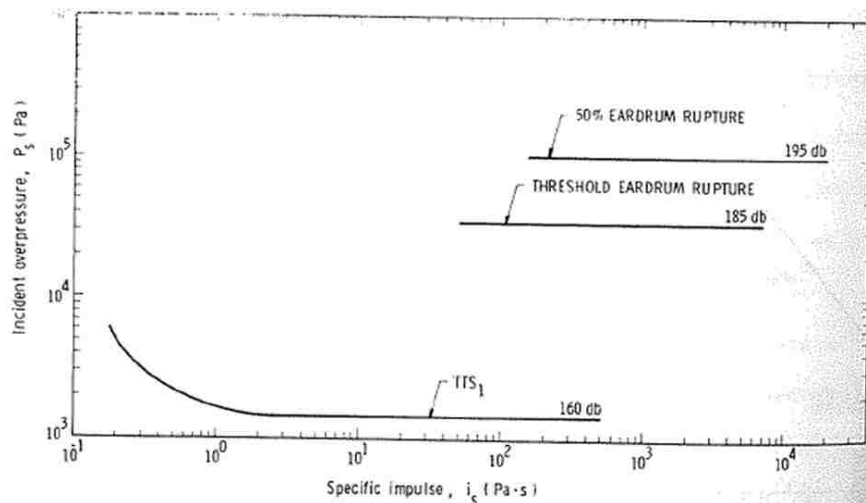
Figure 2.17. P-I curves for eardrum rupture from Baker et al. [81]

Peters [117] conducted a review of published literature of eardrum rupture caused by explosive loading, since eardrum rupture has been used as an indicator for other types of explosive trauma. Peters found that the eardrums do not always rupture when an individual sustains a bTBI. The bTBIs are theorized to occur below the threshold for eardrum rupture. However, the severity of the bTBI at eardrum rupture is not known. Thus, graphing the bTBI and eardrum rupture P-I curves will aid in determining the severity of the bTBI.

2.4. SUMMARY

The theories and concepts reviewed in this section discussed the characteristics of shock waves, P-I graphs, and shock waves' effect on human bodies. Understanding of the methods used to report bTBI animal data were required to conduct this research. This research proposes using a P-I graph to display animal bTBI data, which has not been previously done. This research opens significant opportunities to advance the understanding of bTBI and shock wave behavior at the end of a shock tube for a number of disciplines. Two significant opportunities are defining the jet wind region and a novel method of presenting bTBI data from a large number of studies.

3. FORMULATION EQUATION TO CALCULATE IMPULSE AT THE EXIT AND OUTSIDE OF A SHOCK TUBE (OBJECTIVE 1)

The current method to calculate impulse when only peak pressure and positive time duration are given is the Friedlander equation. The Friedlander equation has been found to represent the pressure trace produced from open-air and interior the shock tube testing [23, 25, 62]. However, the Friedlander equation does not account for sustained pressures observed at and near the shock tube's exit [53–55, 68, 105]. As a result, the loading on the brain is either underestimated or overestimated. To produce a more representative P-I graph of all animal bTBI data, the impulse of the shock wave must be more accurately calculated for the externally placed animal specimens, which accounts for 31.58% of the data points cited in Table 2.1. The equation needed to be calculated from the initial mass, moles of gas produced, and density of the explosive.

Experimental testing was conducted to determine whether modifications to the Friedlander equation or a new equation was needed for the commonly used external test locations to more accurately calculate impulse (Objective 1). The commonly used external test locations are the exit of the shock tube and a short distance away from the exit of the shock tube. At both external locations, the animal specimens are subjected to sustained pressures after the initial pressure decay [105]. The author hypothesizes that the vortex ring formed from the passage of the shock wave needs to be accounted for in the proposed equation, as the vortex ring would affect the pressure decay rate, thus affecting the shape of the measured pressure wave. This new impulse equation would allow for the creation of a human bTBI P-I graph scaled from small mammal bTBI testing when only peak pressure and positive phase duration are provided.

3.1. EXPLOSIVE EQUIVALENTS METHODS NEEDED

To test the proposed hypothesis and determine the parameters of the impulse equation to achieve Objective 1, a 15-foot-long, 6.125-inch-diameter pipe was used to conduct explosive testing. The 15 ft. length was chosen because the average distance between the shock source and sensor location was 14 ft. for the shock tubes referenced in Table 2.1. The explosive charge was placed 1 ft. into the pipe to achieve the 14 ft. distance between the explosive and the end of the pipe. The 6.125 in. diameter was chosen so that the pressure sensor would not obstruct more than 20% of the cross-sectional area of the pipe in accordance with Needham et al.'s findings [49]. The PCB pencil probe (model 137B23B) has a diameter of 0.87 in., and thus the probe obstructs approximately 2% of the cross-sectional area of the pipe. Reflected measurements were also recorded but not investigated further in this research.

The pencil probe was placed at four different locations outside of the shock tube so that the center of the sensor was located at horizontal and vertical centerline at 0 cm (0 in.), 3 cm (1.18 in.), 6 cm (2.36 in.), and 9 cm (3.54 in.) from the exit, as shown in Figure 3.1 and Table 3.1. The chosen distances were representative of external shock tube animal bTBI studies. These locations were chosen to determine the relationship of the shock wave and vortex ring, the vortex ring effect on positive phase time duration, the vortex ring effect on the measured impulse, and the decay rate of peak pressure. The data collected from these four distances would allow for verification that the vortex ring is the main source of the jet wind reported in numerous studies [25, 49, 62, 63] and the pressure does not decay immediately upon exiting the shock tube [26].
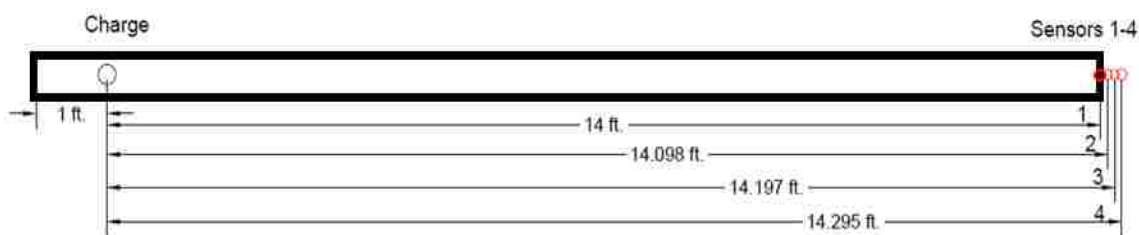
Figure 3.1. Explosively driven shock tube with charge location shown and sensor locations denoted by numbers 1-4

Table 3.1. Sensor and distances from explosive charge for sensors shown in Figure 3.1

Sensor #	1	2	3	4
Distance (ft.)	14	(14) + 0.098	(14) + 0.197	(14) + 0.295
Distance (in.)	168	(168)+ 1.18	(168)+ 2.36	(168)+ 3.54
Distance (cm)	426.72	(426.72) + 3	(426.72) + 6	(426.72) + 9

Two different types of explosives were used to generate the shock waves. The first explosive, pentolite, was used to determine the impulse equation. The second explosive, C4, was used to determine the applicability of the proposed impulse equation to different types of explosives. A 10 g Dyno Nobel Trojan Stinger was used for the pentolite charge. The pentolite charge produced pressures at the upper limit of the pencil probe pressure transducers calibrated range of 50 psi and characteristics of transducers are given in Appendix A. To ensure that the pressures did not exceed the calibrated range of the pencil probes, the weight of the C4 had to be reduced, as C4 is documented to have a higher brisance. An equivalence of 46% to pentolite was chosen resulting in 4.3 g C4 sphere. The mass of the C4 was determined by: calculating the pentolite charge's equivalent weight of

TNT using the detonation velocity method, multiplying 12.596 g by 0.46 to achieve 46%, and dividing by C4's equivalency resulting in approximately 4.3 g. The 46% TNT equivalency was used to determine the applicability of the impulse equation to varying TNT equivalencies. The detonation velocity method was used, because the detonation velocities were well documented by the manufacturers. The testing was broken into two test series: one for pentolite and one for C4. Each series was composed of 12 experiments allowing for three test iterations for each distance and shown in Table 3.2. One distance was tested at a time, due to space restrictions and interferences. Addition of another sensor would cause changes in the pressure readings not observed in animal bTBI studies.

Table 3.2. Parameters of test series used to gather data to develop impulse equations

Test series	Experiment #	Location	Explosive	Sensor location
1	1-3	Exit	10 g Pentolite	1
	4-6	3 cm		2
	7-9	6 cm		3
	10-12	9 cm		4
2	1-3	Exit	4.3 g C4	1
	4-6	3 cm		2
	7-9	6 cm		3
	10-12	9 cm		4

Before the equation could be developed, the relationships between the pentolite and the C4 needed to be known. Three such relationships are amount of gas produced/released to one mole of TNT, density of the explosive or gas to the average density of TNT, and the mass of the explosive or gas to the equivalent TNT mass.

3.1.1. Gas Produced Relationship to TNT. The first relationship is the gas ratio between the moles of gas produced or released from an explosive to the equivalent amount of gas produced by one mole of TNT. Explosives produce gas when detonated and must be considered in explosively driven shock tubes. The number of moles of gas produced per mole of explosive has been well documented by Cooper [28]. Other methods exist to calculate the number of moles produced by an explosive, such as Berthelot's gas equivalency method [28, 71, 72] and balancing the chemical reaction equation [28]. For gas driven shock tubes, the moles of gas released can be calculated by solving for moles of gas in the ideal gas law [28]. The volume of the driver section, rupture pressure, and temperature of gas are normally given in shock tube testing. Some studies provide the volume of gas from which moles can be calculated. The volume of gas is multiplied by density and moles per gram to determine the number of moles released into the driven section. The gas production relationship is the ratio between the moles of gas produced or released in the shock tube and the total moles of gas produced by an equivalent amount of TNT.

The moles of gas produced per mole of TNT and C4 were found in Cooper's work [28]. The moles of gas produced by pentolite were determined by solving for moles of gas produced in the Berthelot equation (Equation(19)). The value of molecular mass of 50/50 pentolite was determined to be twice the molar mass of pentaerythritol tetranitrate (PETN), as the 50/50 ratio is determined by weight and not moles, resulting in a mass of 0.454 kg/mol. The Berthelot's TNT equivalency and molar heat of detonation were taken from *Explosives Engineering* [28] (1.56% TNT equivalent) and a LLNL report [73] (6.4 MJ/kg or 2907.29 kJ/mol), respectively. When all the values were inserted into the Berthelot

equation, one mole of pentolite was found to produce 13 mol of gas when detonated, as shown in Equation (19). The moles of gas produced for each explosive and ratio to TNT gas production are shown in Table 3.3.

$$\Delta n = \frac{\%(TNT\ equiv) * (FM)^2}{840 * (-\Delta H_R^0)} = \frac{156 * 0.454264^2}{840 * 2907.29} = 13.18 \approx 13 \qquad (19)$$

Table 3.3. Moles of gas produced by TNT, C4, and pentolite and ratios

	TNT	C4	Pentolite
Gas (mole)	11	9	13
TNT ratio	1	9/11 (0.8182)	13/11 (1.182)
C4 Pentolite ratio	-	9/13 (0.6923)	13/9 (1.444)

3.1.2. Density Relationship to TNT. The second relationship is the density of the explosive or gas to the density of TNT. For explosively driven shock tubes, the density is not always given; however, the characteristics of the explosive charge are given. The density can be calculated from the mass of the charge divided by the volume of the charge. For the gas-driven shock tube, the density of the air can be calculated from the number of moles of gas found in the ideal gas relationship. The moles of gas need to be multiplied by the grams per mole for the gas and then divided by the volume of the driver section of the shock tube, as shown in Equation (20). The TNT density of 1.64 g/cm^3 given by Cooper [28] was used because the detonation velocity at this density will be used in the following relationship. The density of the pentolite was given by the manufacturer as 1.6 g/cm^3. The

density of C4 was determined by dividing the mass of the explosive by the volume of the explosive. The density was found to be 1.41 g/cm^3. The density of each explosive and ratio to TNT density are given in Table 3.4.

$$density\ of\ air = \frac{moles\ of\ air * g/mole}{volume\ of\ driver\ section} \qquad (20)$$

Table 3.4. Density of TNT, C4, and pentolite

	TNT	C4	Pentolite
Density (g/cm^3)	1.64	1.41	1.6
TNT ratio	1	1.41/1.64 (0.8598)	1.6/1.64 (0.9756)

3.1.3. Mass Relationship to TNT. The third relationship is the mass of the explosive or gas to the equivalent TNT mass. The equivalent TNT mass can be calculated by three different methods, as described in Section 2.1.5. However, to determine TNT equivalency of a gas driven shock tube, the detonation velocity method (Equation (12)) needs to be used, as only one variable needs to be determined. For explosively driven shock tubes, the detonation velocity of an explosive is usually given by the manufacturer and can be found in books, such as Cooper's book [28]. To determine the detonation velocity of a gas driven shock tube, the equivalent velocity of the rupture pressure was assumed equivalent to the detonation velocity of an explosive. The velocity at the rupture pressure was determined by using Equation (4) and Figure 2.7 developed by Swisdak [35]. The

relationship between the mass of an explosive or gas to the equivalent mass of TNT is needed to determine the equation to calculate impulse at the end of a shock tube.

The detonation velocity of the C4 and pentolite given by the manufacturer were used in Equation (12) to calculate the TNT equivalency of each explosive and assumed true for both explosives. C4 has a higher detonation velocity than pentolite resulting in a greater TNT equivalency. The C4 mass was found to be 46.3% of the mass of the pentolite. The equivalent masses for C4 and TNT are summarized in Table 3.5.

Table 3.5. Mass and equivalent TNT mass of C4 and pentolite

	TNT	C4	Pentolite
Mass (g)	0	4.3	10
TNT equivalency	1	1.3556	1.2596
Equivalent mass (g)	0	5.829	12.596

The three previously discussed relationships will be needed when the results of the experiments are analyzed. These relationships will aid in the development of an equation to more closely determine the impulse of a shock wave at and beyond the exit of a shock tube. The following section will discuss the setup of the experimental testing. The presented relationships will be further discussed in Sections 3.3 and 3.4.

3.2. TEST SETUP

The experimental testing took place at the Missouri S&T Experimental Mine's blast pad. The 15 ft. pipe (shock tube) described in Section 3.1 was placed on the blast pad on two stands so that the pipe did not move or rotate during the experimentation. Once the

shock tube was in the desired location, the charge holder was placed at one end of the shock tube, shown in Figure 3.2. The charge holder was a small section pipe with the same diameter of the shock tube with a three-pronged rod holder at one end of the pipe. The rod holder held a two-foot-long hollow conduit pipe. The conduit pipe ensured that the charge was placed 1 ft. into the shock tube. To ensure that the charge was centrally placed within the tube, two pieces of angle iron were welded to the sides of the charge holder.
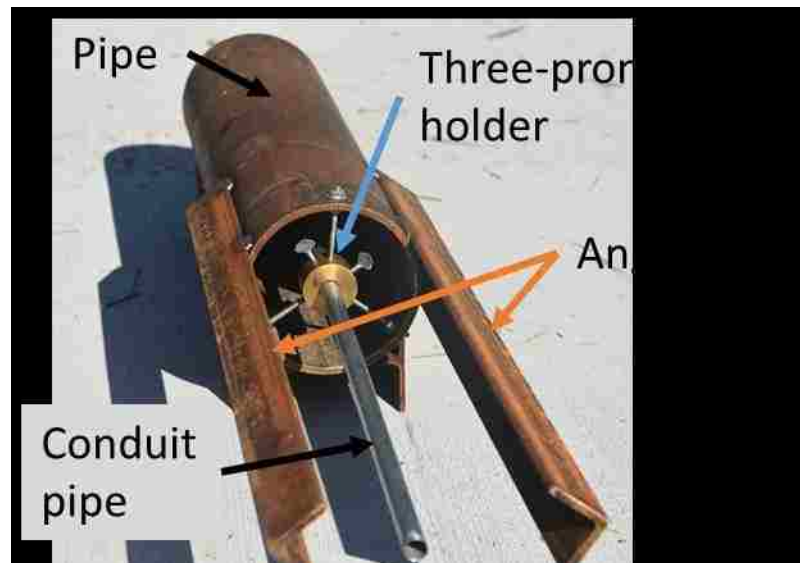
Figure 3.2. Charge holder for shock tube testing

The pencil probe holder was placed at the opposite end of the shock tube to record incident pressure. Incident pressure was used, because majority of the studies listed in Table 2.1 reported incident pressures. The pencil probe holder had a similar design to the charge holder except for the angle iron, as shown in Figure 3.3. The pencil probe holder had this design so that the pencil probe was placed in the center of the shock tube. The

central location was chosen to replicate animal bTBI testing. To ensure that the pressures measured by the pencil probe (PCB model: 137B23B) were only from the shock wave exiting the shock tube, the distance between the pressure transducer and the pencil probe holder was approximately 8.5 inches. If the pressure sensor was placed near the holder, the sensor would record both the incident shock wave and reflections from the holder. The 8.5 inches distance allowed for the entire shock wave to pass over before any reflections could reach the sensor and prolong the wave duration further.

Figure 3.3. Pencil probe holder for shock tube testing

The placement of the detonator was the same for both test series. However, the procedure for attaching the explosive charge to the detonator and conduit pipe was different between Test Series 1 and 2. The detonator was fed through the conduit pipe and then placed into the charge holder, as shown in Figure 3.4.a. For Test Series 1, the detonator

was inserted into a coupler attached to the pentolite stinger insuring that the detonator was in direct contact with the stinger. The detonator end of the pentolite stinger was placed end to end with the conduit pipe and secured in place with electrical tape. A break wire was placed on the other end of the pentolite stinger and secured with tape, as shown in Figure 3.4.b. For Test Series 2, the same procedure was used for the detonator and the conduit; however, the break wire was placed over the detonator. The C4 sphere was placed inside the finger portion of a latex glove and then the detonator was centrally placed within the charge. The charge was taped to the detonator to hold the detonator in place, increase confinement, and density of the C4. The charge was then measured to calculate the density of the charge. The C4 was taped to the end of the conduit, as shown in Figure 3.4.c. After the charge was attached to the end of the conduit pipe, a 1 ft. distance from the front of the explosive charge was measured, marked on the conduit and then inserted into the shock tube to the marked distance, as shown in Figure 3.4b. Once the charge and pencil probe were in place, the detonator's leg wires were connected to a lead line and then detonated with a hand-held blasting box.

Figure 3.4. Setup of explosive charges a. Detonator b. Stinger c. C4. d. Charge inserted into shock tube

As the charge was being placed, the pencil probe was positioned at the locations given in Table 3.2. For the exit location, the sensor was bisected by the cross section of the shock tube exit, being equally placed in the shock tube and in the open air, as shown in Figure 3.5. The locations of 3, 6, and 9 cm were measured from the end of the shock tube. The pencil probe holder was marked on the concrete pad at each distance; the marking was used to determine if the pencil probe holder was moved as a result of the shock wave as well as ensuring the probe was placed in the same location for each repeated test.
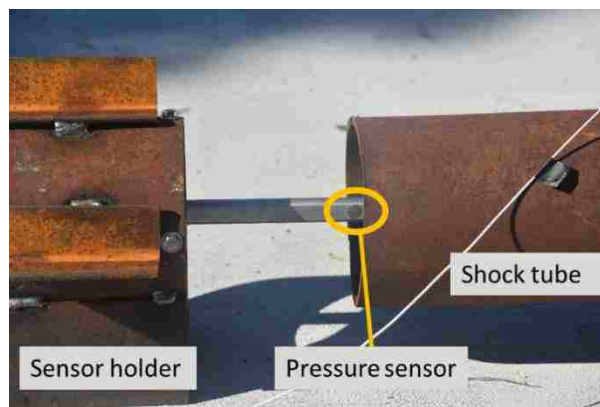
Figure 3.5. Sensor at exit location

A Synergy High Techniques Data Acquisition System (DAS) was used to record the pressure of the shock wave and vortex ring after each initiation of an explosive charge. The DAS was set to record 2 million samples per second and the pressure sensor has a response rate of approximately 154 kilohertz, thus allowing for the peak of the shock wave to be recorded and approximately 217 samples in the rise time. The DAS was connected to the pencil probe by a 100 ft. coaxial cable. The DAS was triggered by the explosive

breaking the break wire that was either connected to the DAS via a trigger box or to a phantom high-speed camera that was connected in series to the DAS. A pre-trigger of 25% was used on the DAS to ensure that the entire explosive event was captured. The recorded results were then exported and saved as an Excel file for data analysis.

Two different high-speed cameras were used to capture detonation, shock wave, and vortex ring. A color MREL Blaster's Ranger II high-speed camera was used to capture the majority of the experiments at different angles. The frame rate for the MREL was 668 frames per second. For the other experiments, a monochromatic Phantom high-speed camera was used to capture the progression of the shock wave and vortex ring. The frame rate of the Phantom was 22,000 frames per second. Both cameras used a lens with a 200 mm focal length.

3.3. RESULTS

The results were analyzed for each iteration after each day of testing. For brevity, the three iterations at each distance are presented on the same pressure versus time (P-T) graph. The peak pressure and the impulse calculated by the midpoint approximation method (Equation (5)) are given in tabular form for easier comparison and analysis. For each of the results, only the initial positive pressure phases were considered.

    3.3.1. Exit of the Shock Tube. The first distance tested for both types of explosives was at the exit of the shock tube. The results for Pentolite and C4 (Figure 3.6 and Figure 3.7 respectively) are presented on different graphs so that the trends are easier to observe. The peak pressure and calculated impulse are presented in the same table, as shown in Table 3.6. The 95% confidence intervals for peak pressure and time duration for both pentolite and C4 were calculated. The pentolite's confidence intervals were (46.573

psi, 50.221 psi) for peak pressure and (2.188 ms, 2.351 ms) for time duration. The C4's confidence intervals were (26.856 psi, 28.974 psi) for peak pressure and (1.878 ms, 1.946 ms) for time duration. Based on these confidence intervals, the data collected indicated a high level of precision and three test iterations were adequate. The P-T curves for the first and second iterations had more noise than the third iteration.

The variation in recorded signal, or noise, was observed in the first pentolite data set collected at the exit of the shock tube. The noise may be the result of a breeze passing over the sensor during the recording of the pressure trace. Another possibility is the interference of the coaxial cable exaggerated the minute pressure changes. This pressure trace was compared to the other two iterations and the first pressure trace was found to be in good agreement. Based on the close similarities, all three iteration at the exit of the shock tube were used in the development of the impulse equation.
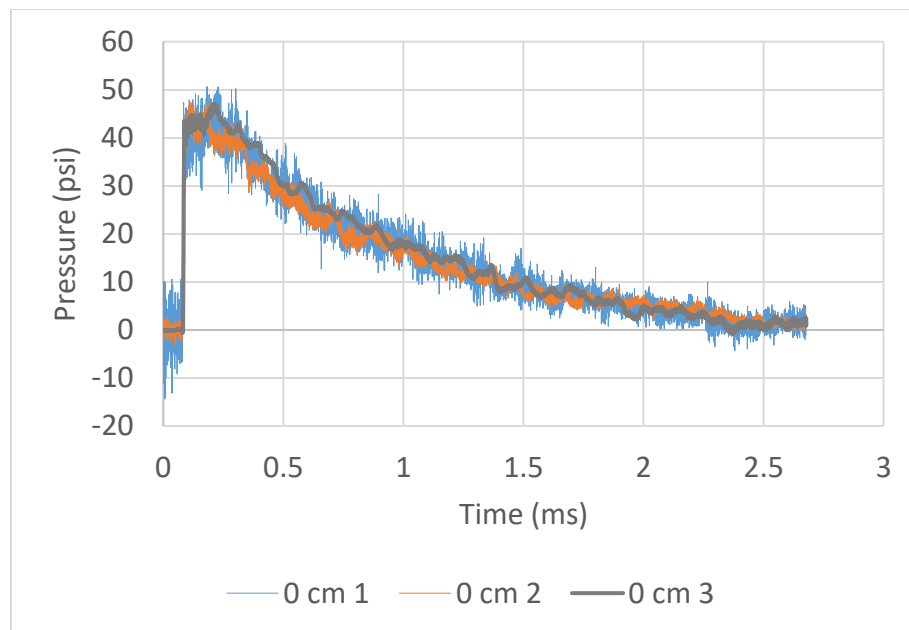
Figure 3.6. Pentolite data recorded at the end of the shock tube for three iterations
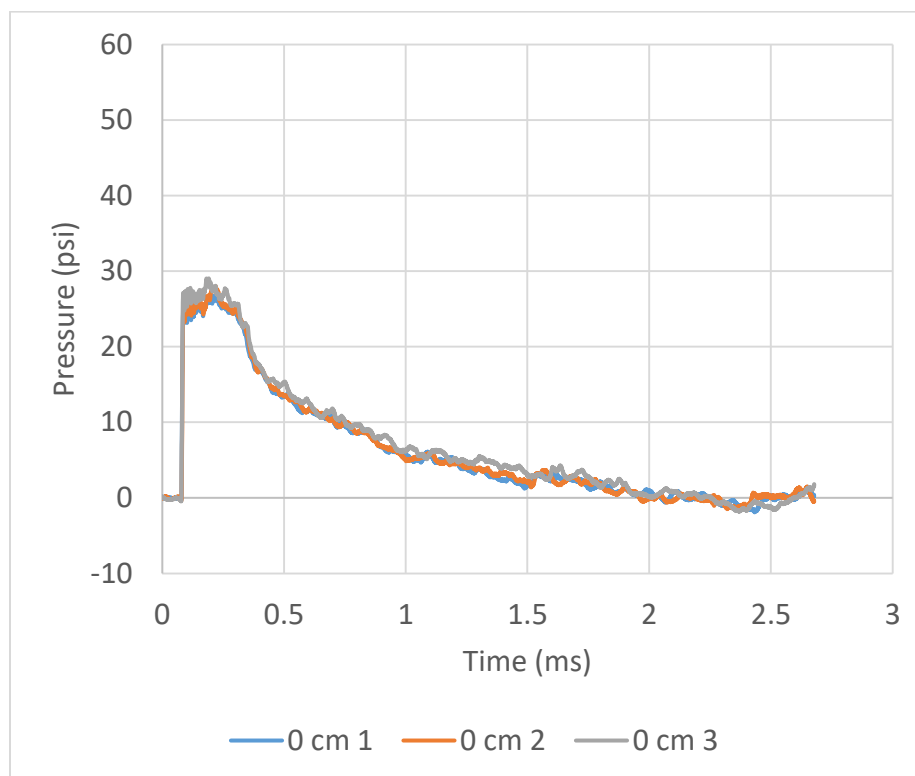
Figure 3.7. C4 data recorded at the end of the shock tube

Table 3.6. Peak pressures, durations, and impulses at the exit of the shock tube

	Pentolite			C4		
Experiment	1	2	3	1	2	3
Peak Pressure (psi)	50.673	47.381	47.138	26.740	27.973	29.030
Duration (ms)	2.182	2.358	2.267	1.948	1.875	1.913
Impulse (psi*ms)	37.795	37.574	39.525	16.549	16.837	18.341
Peak Pressure (kPa)	349.376	326.680	325.006	184.367	192.870	200.158
Impulse (kPa*ms)	260.584	259.062	272.513	114.102	116.089	126.459

3.3.2. 3 Centimeters from Exit of the Shock Tube. The second distance tested for both types of explosives was 3 cm (1.18 in.) from the exit of the shock tube. The results for each explosive (Figure 3.8 and Figure 3.9) are presented on different graphs so that the

trends are easier to observe. The third pressure trace in Figure 3.9 has a faster decay rate due to different weather conditions. The first two iterations were conducted on sunny days and no rainfall the day before. The third iteration was conducted on a cloudy day after a night of rain. A similar trend was also observed in the third iteration of pentolite with the sensor placed 6 cm from the end of the shock tube. The peak pressure and calculated impulse are both presented in Table 3.7. The 95% confidence intervals for peak pressure and time duration for both pentolite and C4 were calculated. The pentolite's confidence intervals were (45.007 psi, 51.417 psi) for peak pressure and (1.818 ms, 1.943 ms) for time duration. The C4's confidence intervals were (25.514 psi, 27.722 psi) for peak pressure and (0.957 ms, 1.438 ms) for time duration. Based on these confidence intervals, the data collected indicated a high level of precision and three test iterations were adequate.
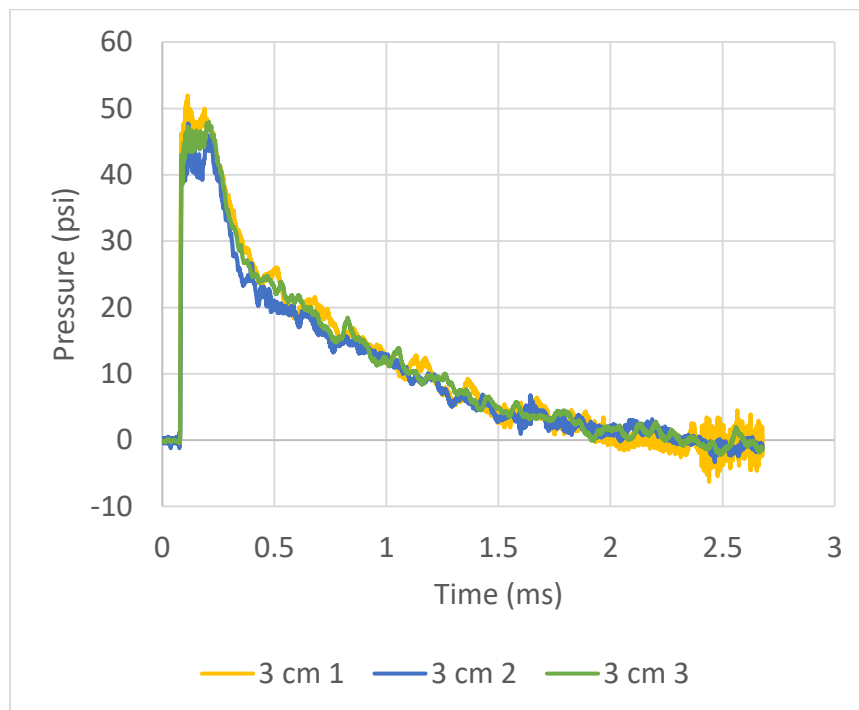
Figure 3.8. Pentolite data recorded 3 cm from the end of the shock tube
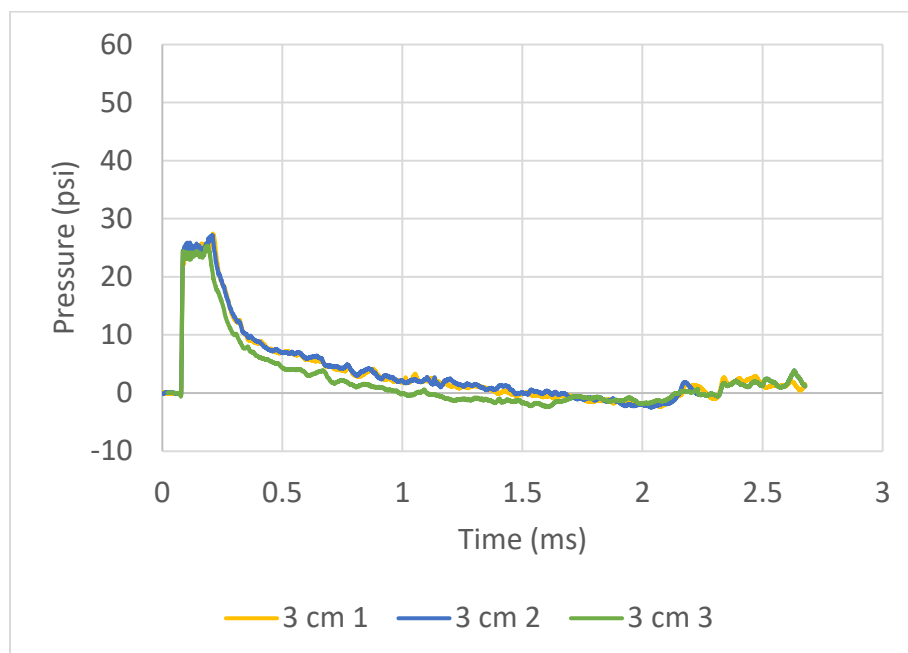
Figure 3.9. C4 data recorded 3 cm from the end of the shock tube

Table 3.7. Peak pressures, durations, and impulse 3 cm from the exit of the shock tube

	Pentolite			C4		
Experiment	1	2	3	1	2	3
Peak Pressure (psi)	51.965	47.713	47.959	27.439	27.169	25.247
Duration (ms)	1.851	1.957	1.833	1.308	1.384	0.900
Impulse (psi*ms)	29.974	27.047	29.211	9.446	9.694	6.780
Peak Pressure (kPa)	358.283	328.968	330.664	189.182	187.322	174.07
Impulse (kPa*ms)	206.661	186.481	201.406	65.1264	66.8371	46.746

3.3.3. 6 Centimeters from Exit of the Shock Tube. The third distance tested for both types of explosives was 6 cm (2.36 in.) from the exit of the shock tube. The results for each explosive (Figure 3.10 and Figure 3.11) are presented on different graphs so that the trends are easier to observe. The third iteration of the pentolite had a faster decay rate

than the other two iterations because rainfall on the previous night. The peak pressure and calculated impulse are both presented in Table 3.8. The 95% confidence intervals for peak pressure and time duration for both pentolite and C4 were calculated. The pentolite's confidence intervals were (45.426 psi, 48.217 psi) for peak pressure and (0.753 ms, 0.888 ms) for time duration. The C4's confidence intervals were (28.251 psi, 29.768 psi) for peak pressure and (0.342 ms, 0.365 ms) for time duration. Based on these confidence intervals, the data collected indicated a high level of precision and three test iterations were adequate.
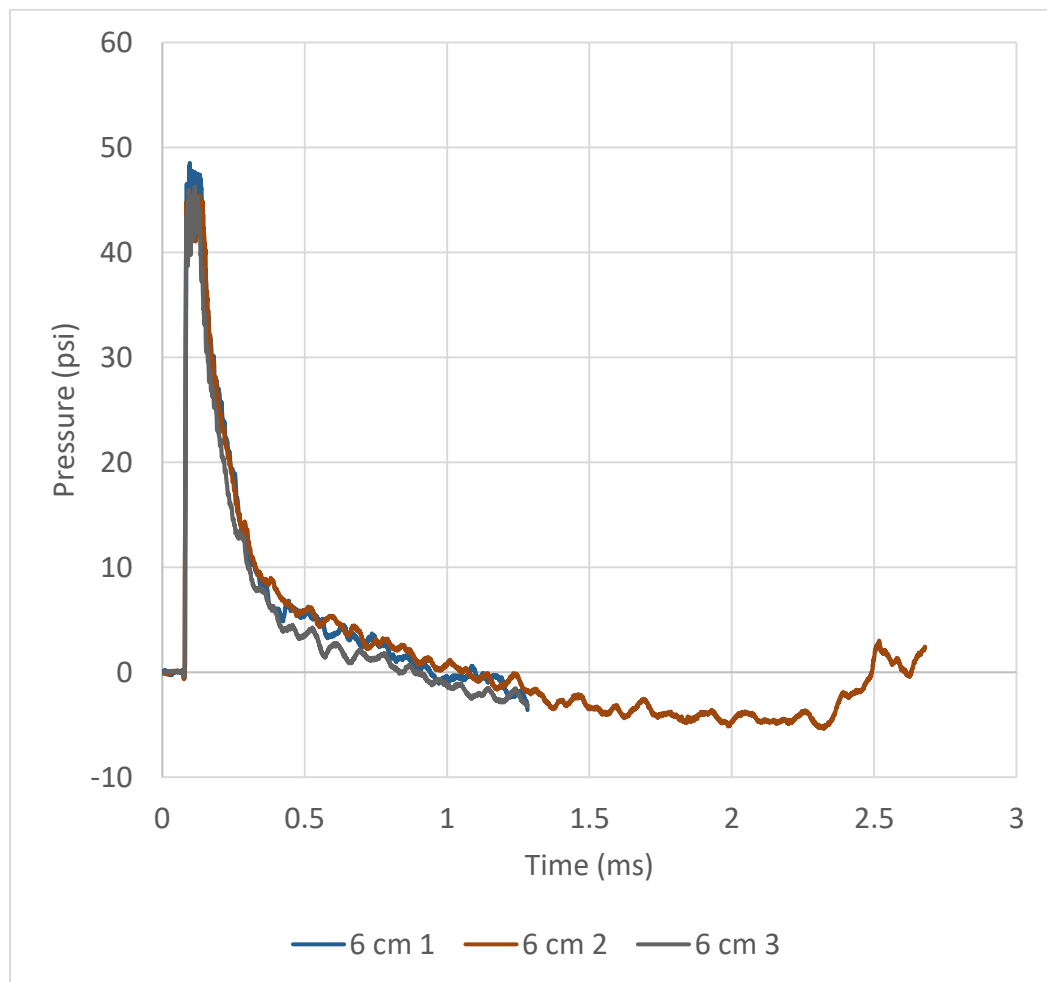
Figure 3.10. Pentolite data recorded 6 cm from the end of the shock tube
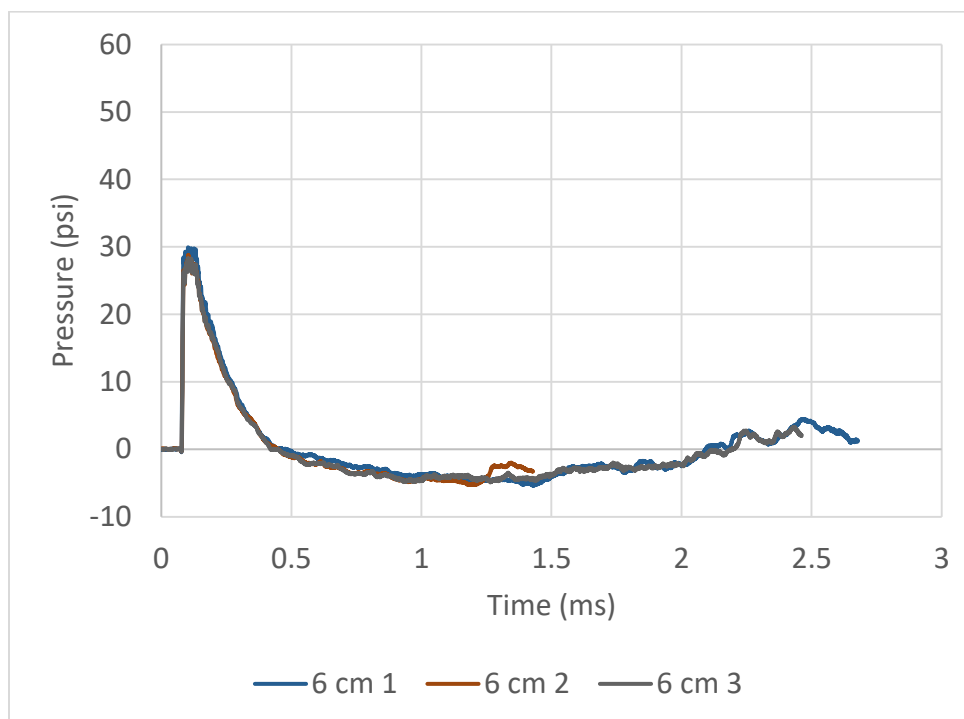
Figure 3.11. C4 data recorded 6 cm from the end of the shock tube

Table 3.8. Peak pressures, durations, and impulse 6 cm from the exit of the shock tube

	Pentolite			C4		
Experiment	1	2	3	1	2	3
Peak Pressure (psi)	48.527	46.284	45.653	29.919	28.784	28.324
Duration (ms)	0.822	0.746	0.892	0.361	0.361	0.339
Impulse (psi*ms)	9.072	7.563	9.401	4.570	4.219	4.229
Peak Pressure (kPa)	334.581	319.119	314.764	206.286	198.462	195.288
Impulse (kPa*ms)	62.5507	52.1476	64.8157	31.5072	29.0919	29.1562

3.3.4. 9 Centimeters from Exit of the Shock Tube. The fourth distance tested for both types of explosives was 9 cm (3.54 in.) from the exit of the shock tube. The results for each explosive (Figure 3.12 and Figure 3.13) are presented on different graphs so that the trends are easier to observe. The peak pressure and calculated impulse are both

presented in Table 3.9. The 95% confidence intervals for peak pressure and time duration

for both pentolite and C4 were calculated. The pentolite's confidence intervals were

(46.301 psi, 48.396 psi) for peak pressure and (0.261 ms, 0.284 ms) for time duration. The

C4's confidence intervals were (26.466 psi, 28.107 psi) for peak pressure and (0.336 ms,

0.345 ms) for time duration. Based on these confidence intervals, the data collected

indicated a high level of precision and three test iterations were adequate.
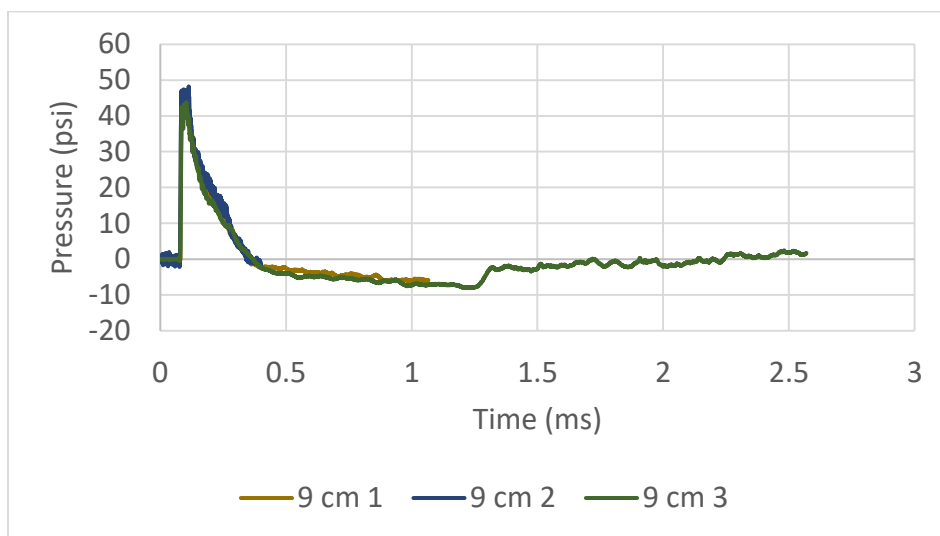
Figure 3.12. Pentolite data recorded 9 cm from the end of the shock tube

Table 3.9. Peak pressures, durations, and impulse 9 cm from the exit of the shock tube

	Pentolite			C4		
Experiment	1	2	3	1	2	3
Peak Pressure (psi)	46.918	48.197	43.788	28.265	27.062	26.532
Duration (ms)	0.269	0.263	0.287	0.336	0.341	0.345
Impulse (psi*ms)	5.076	5.311	4.628	3.412	3.348	3.338
Peak Pressure (kPa)	323.485	332.305	301.906	194.883	186.589	182.934
Impulse (kPa*ms)	34.9953	36.6184	31.9116	23.5218	23.0821	23.0145
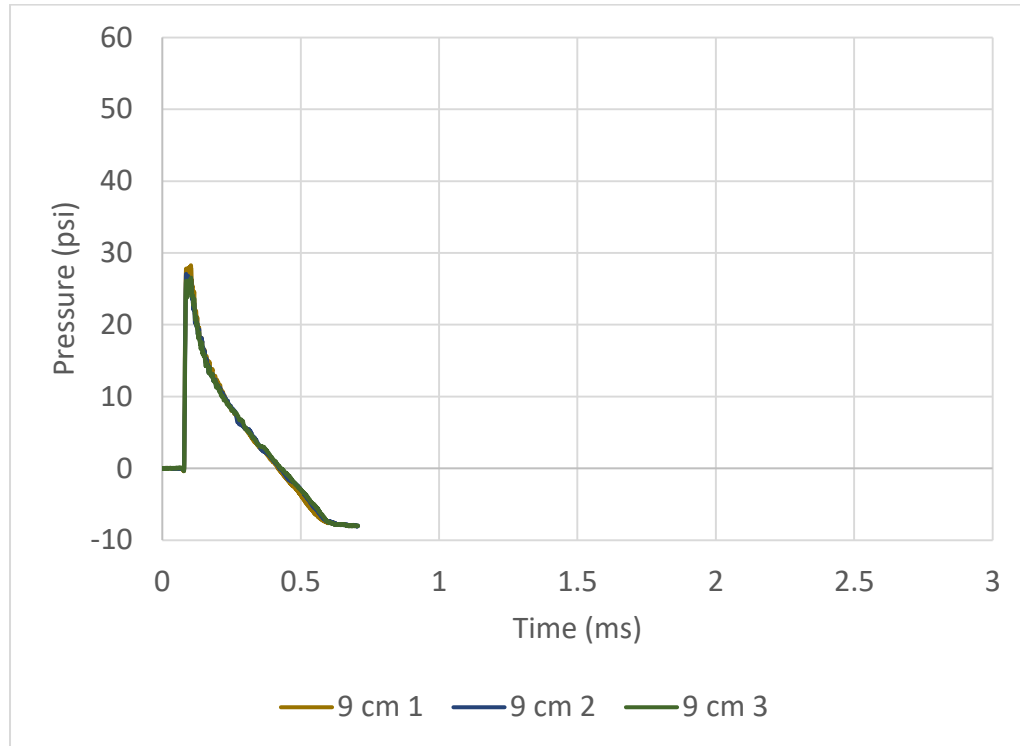
Figure 3.13. C4 data recorded 9 cm from the end of the shock tube

3.3.5. Observed Jet Wind Effect. The jet wind effect was observed in the Phantom high-speed videos. Test Series 1 Experiment 8 (pentolite with sensor at 6 cm) DAS data and Phantom video were used to illustrate the observed jet wind effect, as shown in Figure 3.14. The majority of the shock wave passed the pressure sensor before the arrival of the vortex ring. The arrival of the shock wave is denoted by "a." in Figure 3.14. The arrival of the vortex ring occurs approximately 0.45 ms after the shock wave and changes the decay rate of the pressure trace, as shown in Figure 3.14.b. The vortex ring fully passes over the pressure sensor approximately 0.8 ms after the arrival of the vortex ring, as shown in Figure 3.14c. The observed jet wind effect is caused by the formation and travel of the vortex ring with respect to the shock wave.
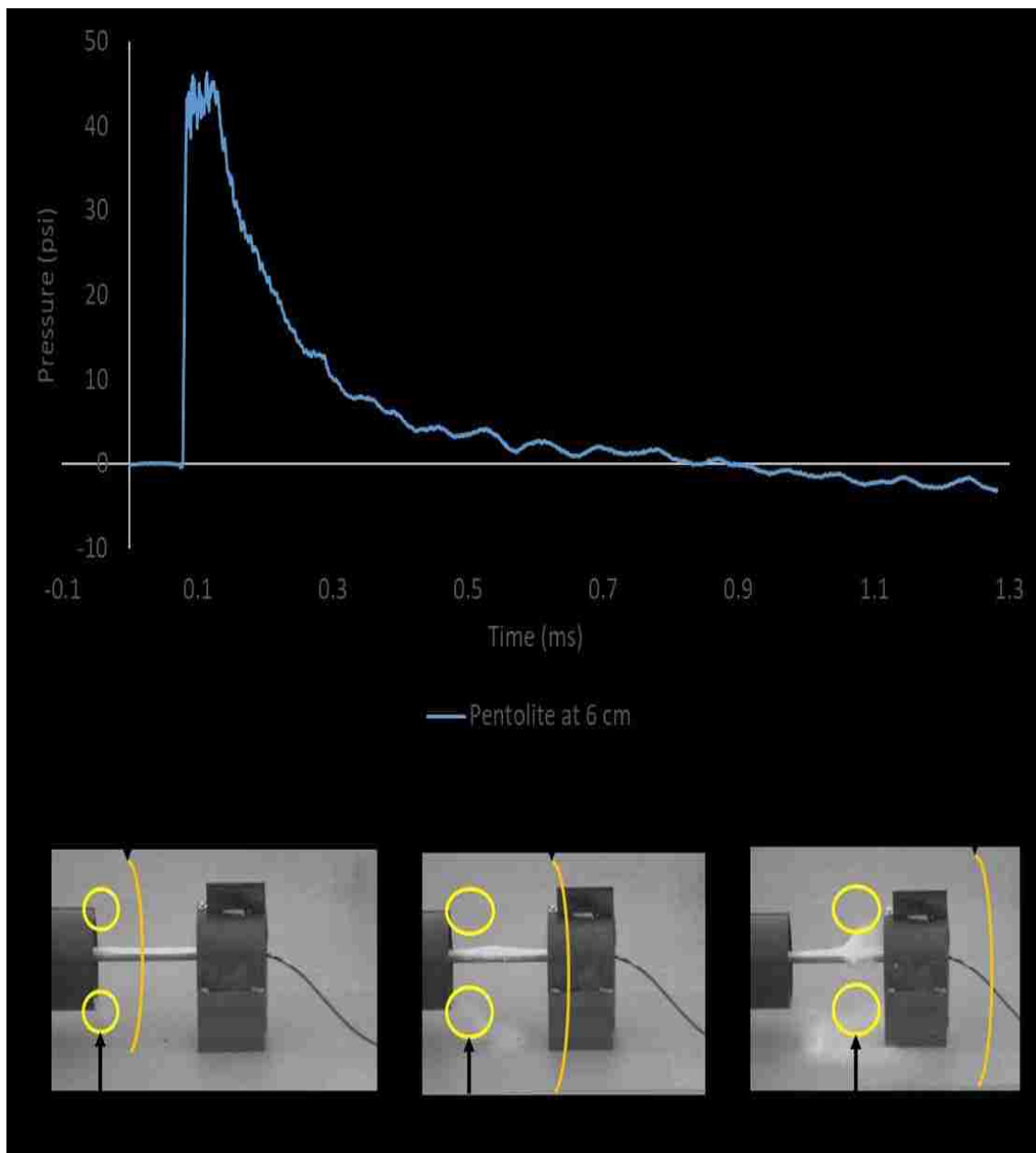
Figure 3.14. Sample pentolite pressure trace with stills from high speed video for indicated areas a. Arrival of the shock wave b. Arrival of vortex ring c. Departure of shock wave and vortex ring

After the explosive is detonated, the shock wave travels down the length of the shock tube and accelerates the air particles within the shock tube. After the shock wave

emerges from the end of the shock tube, the vortex ring is formed. The shock wave is traveling at a higher velocity than the vortex ring, thus complete separation will occur when the shock wave outruns the vortex ring. This separation can be clearly observed in Figure 3.15. The duration of the positive phase decreases as the distance from the end of the shock tube increases. Complete separation occurred between 6 and 9 cm (38.57% and 57.85% of the shock tube diameter) away from the shock tube exit. The 9 cm (orange) pressure trace clearly shows the distinction between the shock wave and the vortex ring. Overall, the observance of a Friedlander wave remains consistent only after separation of the shock wave and vortex ring.
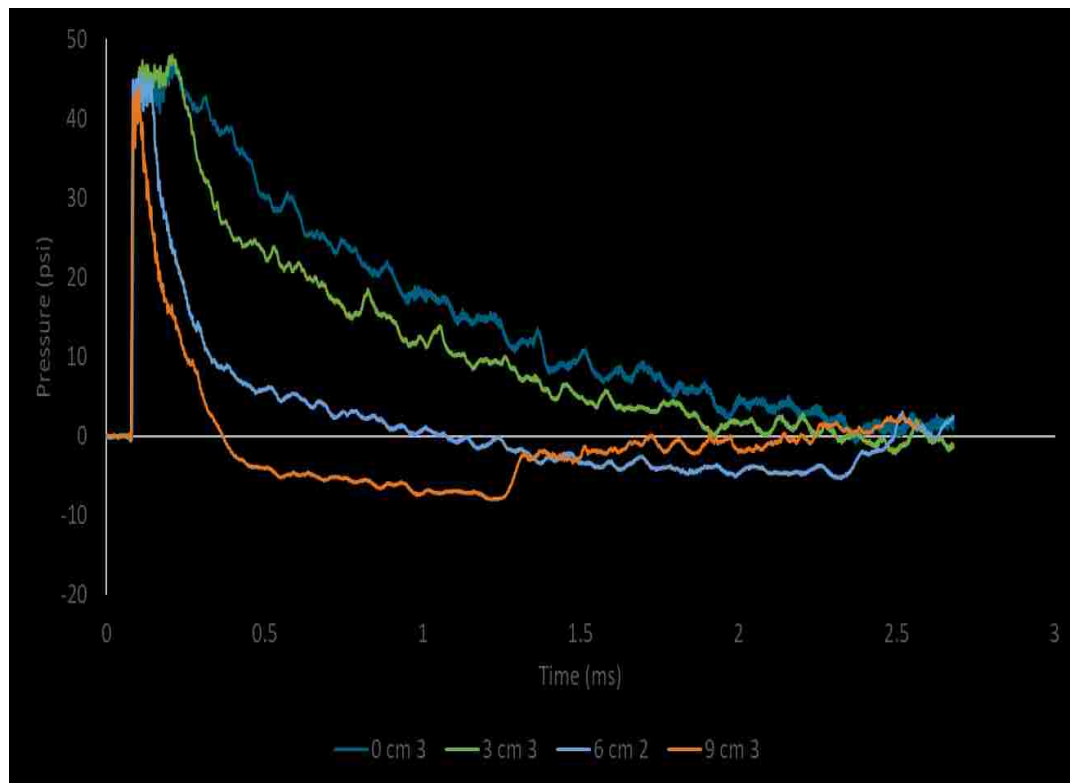
Figure 3.15. Overlay of all tested distances showing the separation of the shock wave and vortex ring

3.4. MODIFICATIONS TO THE FRIEDLANDER (OBJECTIVE 1)

The development of the modifications to be applied to the integral of the traditional Friedlander equation, Equation (8), began shortly after the first data sets were analyzed. One of the first observations made was that the decay rates followed the same trend but at different intervals for the two explosives. The decay rates of the C4 at 0 cm, 3 cm, and 6 cm distances appeared to have the same trend as the decay rates of the pentolite at 3 cm, 6 cm, and 9 cm, respectively, as shown in Table 3.10. This observance was initially assumed to be based on the gas production of the explosive instead of the mass of the explosive, as pentolite produces more gas than C4. To investigate the roles of gas production and velocity of the vortex ring, Equation (8) was used as the base equation. Equation (8) was used because peak pressure and positive phase time duration are required parameters. In addition, the Friedlander equation and variations are documented to describe an ideal decay. Equation (8) was modified by changing the exponent to the exponential from one to a variable. The modified Equation (8) resulted in Equation (21), where β is the impulse modifier.

$$I = \frac{P_s t^+}{e^\beta} \tag{21}$$

To determine the value of β, Equation (21) was rearranged to solve for β. The documented peak pressure, positive phase duration, and calculated impulse for each of the 24 experimental tests were inserted into Equation (21) and the β value calculated. The

resulting values for β are shown in Table 3.10. The previously observed trend between the decay rates was also observed for the values of β, which strengthens the hypothesis that moles of gas produced affects the decay rate of the explosive's pressure trace. Also observed for both explosives was the β value approaching 1.0 when the shock wave and vortex ring became separate entities. To describe mathematically this trend, a piecewise function was determined to be best suited to account for changing β values close to the exit of the shock tube.

Table 3.10. Values of β, impulse modifier, at each tested distance for both explosives

	Pentolite	C4
Distance (cm)	β	β
0	1.074	**1.147**
0	1.090	**1.136**
0	0.995	**1.108**
3	**1.166**	*1.335*
3	**1.239**	*1.356*
3	**1.105**	*1.21*
6	*1.481*	**0.860**
6	*1.519*	**0.901**
6	*1.467*	**0.820**
9	**0.909**	1.024
9	**0.870**	1.013
9	**0.997**	1.009

The piecewise function had to follow the trend of the β values for both explosives that were above the value 1.0, as shown in Figure 3.16. A trend line was plotted along the

nine points for each explosive. Each trend line was a second-degree polynomial with an R^2 value above 0.9. Another form a second-degree polynomial is shown in Equation (22),

$$y = a(x - h)^2 + k \tag{22}$$

where a defines the direction and width of the parabola, h is the x value of the vertex, and k is the y value of the vertex. The vertex is the maximum value of the parabola when a is negative and minimum value of the parabola when a is positive. To determine the values of a, h, and k, the ratios of the pentolite were used. The calculated values for a, h, and k were used to determine the equation for C4 as a confirmation of the values.
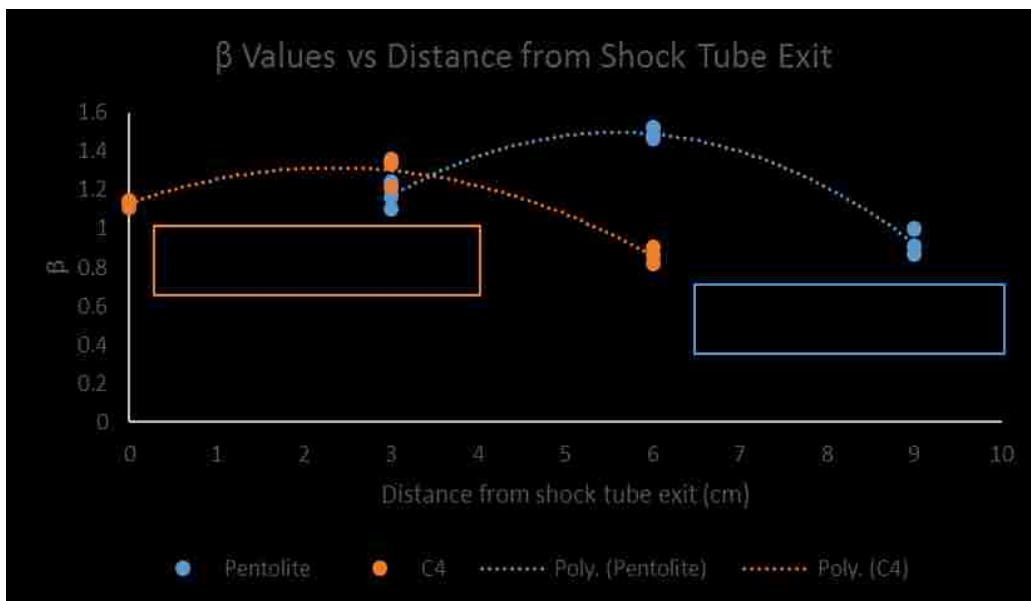
Figure 3.16. Values of β and best-fit trend line greater than 1.0 for pentolite and C4 at tested distances

Before the values of a, h, and k could be determined, the trend line had to be rewritten in the form of Equation (22). The values for pentolite from Figure 3.16 were used to determine the maximum value and the location of the vertex, resulting in Equation (23).

$$y = -0.049(x - 5.5857)^2 + 1.498 = -0.049(x - 5.59)^2 + 1.5 \tag{23}$$

The hypothesis that a related to gas production of the explosive was tested by equating the value of a to the gas production ratio, volume of the shock tube, and a constant, as shown in Equation (24),

$$-0.049 = \frac{g_{pentolite}}{g_{TNT}} * V * C_1 \tag{24}$$

where g is moles of gas produced by one mole of explosive, V is volume of the shock tube between the explosive and exit, and C_1 is a constant. Equation (25) solves for C_1,

$$C_1 = \frac{-0.049 * g_{TNT}}{g_{pentolite} * V} = -5.11 * 10^{-7} \ cm^{-3} \tag{25}$$

which was found to have a small value due to the large volume of the shock tube. The mass relationship and density relationship from Section 3.1 were used to determine the values of h and k from Equation (23).

The mass of the explosive determines how much energy is imparted into the shock wave and would have a greater influence than density. Thus, h was hypothesized to be the mass relationship and k was the density relationship. As with a, h was equated to volume of the shock tube and a constant with the mass relationship, as shown in Equation 26,

$$-5.59 = m_e * TNT\ equ * V * C_2 \tag{26}$$

where m_e is the mass of the explosive, *TNT equ* is TNT equivalency, V is volume of the shock tube, and C_2 is the fitting constant. The value of C_2 was solved for, as shown in Equation (27),

$$C_2 = \frac{-5.59}{m_e * TNT\ equ * V} = 5.47 * 10^{-6}\ cm^{-3}g^{-1} \tag{27}$$

The value for k was similar to a, but with a density ratio, as shown in Equation (28),

$$1.5 = \frac{\rho_{pentolite}}{\rho_{TNT}} * V * C_3 \qquad (28)$$

where ρ is density, V is volume of the shock tube, and C_3 is the fitting constant. The value

of C_3 was solved for, as shown in Equation (29),

$$C_3 = \frac{1.5 * \rho_{TNT}}{\rho_{pentolite} * V} = 1.89 * 10^{-5} \ cm^{-3} \qquad (29)$$

The absolute values of the constants increase an order of magnitude with each successive

parameter. With the parameters a, h, and k known, the piecewise function to describe β can

be developed.

The proposed parabolic function accounts for the separation of the shock wave and

the vortex ring. The parabolic function takes the form of Equation 30, when all the

parameters are inserted into Equation (21), where x is the distance outside the shock tube.

When combined with the constant decay rate after separation, the piecewise function takes

the form of Equation (30),

$$y = C_1 * V * \frac{g_e}{g_{TNT}} \left(x - (C_2 * m_e * TNT \ equ * V) \right)^2 + C_3 * V * \frac{\rho_e}{\rho_{TNT}} \qquad (30)$$

where β is the exponent to the exponential in Equation (21) and *y* is the parabolic function given in Equation (31) or the Rutter-Johnson equation.

$$I = \frac{PT}{e^\beta}, where\ \beta = \begin{cases} 1 & if\ y < 1 \\ y & if\ y \geq 1 \end{cases} \tag{31}$$

The Rutter-Johnson equation was then applied to the C4 to determine the soundness. The resulting values and percent error with respect to the parabola values are given in Table 3.11. The values for *a* and *k* are very close to parabola values. The *h* value was 10% above the given value, which may be because the third iteration at 3 cm for the C4 is an outlier. If the value in the equation is removed from the trend line calculation, the percent error for *h* would be reduced; however, the percent error of *a* and *k* would increase. Before the equation could be considered a replacement for the current method, the error between the Rutter-Johnson equation and the Friedlander method would need to be compared.

The midpoint approximation method was used to calculate the actual impulse value for each of the experimental data sets. The error was calculated by comparing actual impulse value to impulse values calculated from Equation (8) (Friedlander method) and Equation (31) (Rutter-Johnson method). The percent error for the Friedlander and Rutter-Johnson methods is presented in Table 3.12, where the listed error is representative of the other iterations at each distance for both explosives. The reduction of the error from the Friedlander impulse calculation is needed for the development of the P-I graph of animal

data to be scaled to humans. The entire error comparison table is given in Appendix A. The

Rutter-Johnson method reduced the error from the Friedlander method when the vortex

ring interacts with the shock wave. The error between the Friedlander method and the

Rutter-Johnson method is the same when the value of β is equal to one, which is when the

shock wave and vortex ring are separate entities. Overall, the Rutter-Johnson method

accounts for the vortex ring interacting with different portions of the shock wave.

Table 3.11. Values of *a*, *h*, and *k* from Equation (30) and percent error

	Equation (30)	Parabola	Percent Error
a	-0.0339	-0.0339	0.00%
h	2.5872	2.33	9.94%
k	1.3181	1.315	0.24%

Table 3.12. Comparison of error between Friedlander and proposed methods

	Pentolite		C4	
Distance (cm)	Friedlander error	Rutter-Johnson error	Friedlander error	Rutter-Johnson error
0	9.41%	9.41%	15.79%	3.99%
3	10.71%	8.12%	23.36%	11.16%
6	59.45%	3.81%	16.47%[*]	16.47%[*]
9	12.20%[*]	12.20%[*]	2.41%[*]	2.41%[*]

*The value of β is one

3.5. SUMMARY

This section has proposed a new method for calculating impulse outside of a shock

tube (Section 3.4). Based on the four confidence intervals, the peak pressure remains steady

for both pentolite and C4 outside the shock tube, which is consistent with Giannuzzi et al.'s work [26]. However, this is not true with the time duration, as the vortex ring extends the positive phase. This proposed method accounts for the changes in decay rate as the shock wave and vortex ring separate from one another. The proposed method reduces the error found in Friedlander methods when the vortex ring directly influences the decay of the shock wave. Thus, the Rutter-Johnson equation fulfills the requirements for Objective 1 which was to accurately determine impulse for all experimental designs.

Through analysis of the experimental data and the Rutter-Johnson equation, the distance at which the shock wave and vortex ring separate was found to always occur before or at 60% of the shock tube diameter. The 60% shock tube diameter should be used in future animal bTBI to ensure the animal is exposed decay trends observed in open-air testing. The Rutter-Johnson can be used on other shock tube diameters and sizes, since volume is accounted for in the equation. The Rutter-Johnson equation was not tested with reflected pressures and the relationship to related pressures needs to be studied.

The Rutter-Johnson method will be used in the following sections in the generation of a human P-I graph of bTBI and its relationship with observable injuries. The Rutter-Johnson method will be used on 31.58% of the gathered animal bTBI data, which will then be scaled to humans. The Friedlander method will be applied to the other 68.42% from open-air and interior shock tube experimental designs that did not include impulse. Overall, the modification to the Friedlander method of calculating impulse with only peak pressure and time duration allows for a better representation of the loading on an animal's brain outside a shock tube.

4. PROPOSED HUMAN BTBI SEVERITY REGIONS (OBJECTIVE 2)

The human bTBI severity regions were determined by plotting the scaled peak pressure and scaled impulse presented in Table 2.1 (page 35) from the animal model to humans. The peak pressure was scaled using Jean's method (Equations (16) (page 37) and (17) (page 38)). A scaling method has been developed for impulse, as no impulse scaling method had been published.

This section is divided into four subsections. The impulse calculation for open air, interior shock tube, and exterior shock tubes is discussed in Section 4.1. The scaling of peak pressure and positive phase duration from the animal model to humans is discussed in Section 4.2. The proposed human bTBI P-I graph and severity regions are presented and discussed in Section 4.3. A summary of the methods used to determine human bTBI severity regions is presented in Section 4.4.

4.1. SCALING OF IMPULSE

In Section 3, the Friedlander impulse equation (8) was used to calculate impulse for open air and interior shock tube experiments. For both of these test methods, the shock wave and resulting pressure trace resemble a Friedlander curve. However, exterior shock tube experiments do not always resemble a Friedlander curve. To determine the impulse for the exterior shock tube experiments, the Rutter-Johnson equations developed in Section 3.4 (Equation (30) and (31)) were used. The equations used for each cited study are summarized in Table 4.1.

The open-air and exterior shock tube experiments that included impulse (Song, Beamer, and Shridharani) had the β decay value calculated using Equation (32),

$$\beta = \ln\left(\frac{PT}{I}\right) \tag{32}$$

where P is the given peak pressure, T is the given positive phase time duration, and I is the given impulse value. The calculated β value was assumed to describe the decay rate of the pressure trace for each specific experimental design. The calculated β value will be used for the scaled impulse in Section 4.2.

The other exterior shock tube experiment's impulse values were calculated by using the Rutter-Johnson equation developed in Section 3.4. 60% shock tube diameter exit distance was confirmed by analyzing Kabu, Budde, and Svetlov works. The shock wave and vortex ring were found to be separate entities at those distances. For the shock tube experiments where the animals were placed at the end of the shock tube (Long and Kuehn), the y value (Equation (23)) was found to be less than one for both experiments. Thus, the traditional Friedlander equation was used to calculate impulse.

Two of the data sets in Table 2.1, Turner and Wang, reported reflective peak pressures. To determine the impulse value for these studies, Equation (3) was used to calculate the incident peak pressure. The dynamic pressures associated with the reported reflective pressure were determined by interpolating the dynamic pressure delta value from reflective pressures in reported in Figure 2.7 that were directly above and below the reflective pressure reported by Turner and Wang. The calculated incident peak pressure was used to determine the impulses for Turner and Wang by using the proposed modified impulse calculation equation and the Friedlander equation, respectively. The impulse for Turner was found to be the same as the Friedlander method.

Table 4.1. Impulse equations used for data sets that did not include impulse

First Author	Test type	Model	Sensor Orientation	Reported			Data points	Equation	Value
				PP	I	T			
Song [88, 89]	Open Air	Mice	Incident	x	x	x	101		β
Beamer [51]	Shock Tube	Mice	Incident	x	x	x	2		β
Shridharani [109]	Shock Tube	Pigs	Incident	x	x	-	20		β
Pun [90]	Open Air	Rats	Incident	x	-	x	2	Friedlander	Impulse
Chen 1 [91]	Open Air	Goats	Incident	x	-	x	4	Friedlander	Impulse
Li [92]	Open Air	Goats	Incident	x	-	x	7	Friedlander	Impulse
Saljo 1 [93]	Open Air	Pigs	Incident	x	-	x	8	Friedlander	Impulse
Chen 2 [94]	Open Air	Pigs	Incident	x	-	x	4	Friedlander	Impulse
Wang [48]	Shock Tube	Mice	Reflective	x	-	x	9	Friedlander Swisdak	Impulse
Risling [97]	Shock Tube	Rats	Incident	x	-	x	4	Friedlander	Impulse
Pham [98]	Shock Tube	Rats	Incident	x	-	x	8	Friedlander	Impulse
Kochanek [99]	Shock Tube	Rats	Incident	x	-	x	1	Friedlander	Impulse
Garman [106]	Shock Tube	Rats	Incident	x	-	x	1	Friedlander	Impulse
Saljo 2 [108]	Shock Tube	Rats	Incident	x	-	x	2	Friedlander	Impulse
Turner [96]	Shock Tube	Rats	Reflective	x	-	x	4	Rutter-Johnson Swisdak	Impulse
Kabu [95]	Shock Tube	Rats	Incident	x	-	x	20	Rutter-Johnson	Impulse
Budde [100]	Shock Tube	Rats	Incident	x	-	x	2	Rutter-Johnson	Impulse
Long [104]	Shock Tube	Rats	Incident	x	-	x	3	Rutter-Johnson	Impulse
Svetlov [105]	Shock Tube	Rats	Incident	x	-	x	5	Rutter-Johnson	Impulse
Kuehn [107]	Shock Tube	Rats	Incident	x	-	x	26	Rutter-Johnson	Impulse

4.2. SCALING ANIMAL DATA TO HUMANS

Four animal species were cited in this research and needed to be scaled to humans

individually. The peak pressure and impulse were scaled using two different methods. The

peak pressure was scaled by using Jean's method discussed in Section 2.2.2.2. The three

values in Table 2.2 are calculated in order to scale the rat and goat animal models. The

mass of the flesh surrounding the skull of a rat could not be found, thus it was assumed that

the ratio of a mouse's skull and flesh is the same for a rat. This value may change with new

research but goes beyond the scope of this research. The resulting value of the mass of a

rat's flesh surrounding the skull was found to be approximately 8 grams. The η value, head

scaling formula, for the rat and goat were then calculated using Equation (16). The η values

for each of the animal models and humans are given in Table 4.2. The given peak pressure

and model specific η were then inserted into Equation (17) resulting in the equivalent

human peak pressure. The human peak pressures were found to be lower than the animal

models, due to humans having a higher η value (less soft tissue and skull).

Table 4.2. Scaling parameter for referenced animal models for use in equation (17)

Species	η^s
Mouse	0.126
Rat	0.143
Goat	0.059
Pig	0.024
Human	0.75

The scaled impulse was calculated using Equation (33),

$$I_{scaled} = \frac{P_{scaled}T_{scaled}}{e^\beta}$$ (33)

where P$_{scaled}$ is scaled peak pressure (Equation (17)), T$_{scaled}$ is scaled duration (Equation (14)), and β is the decay rate calculated by either Equation (21) or (32). Equation (21) was used when the animal was outside the shock tube and impulse was not given; whereas, Equation (32) was used when the impulse value was given. If the testing was conducted inside a shock tube or in open air and impulse was not reported, the value for β was 1.0 based on Tasissa et al., Chandra et al., and Kleinschmit [23, 25, 62] discussed in Section 2.1.4.

4.3. HUMAN SEVERITY CURVES (OBJECTIVE 2)

The scaled peak pressures and impulse values were divided into four severity groups: mild, moderate, severe, and not given. After the data sets were separated into severity groups, the values were plotted on a P-I graph. The produced human bTBI P-I graph, shown in Figure 4.1, has regions where numerous studies have been conducted and other regions with little to no research. The severity group with the largest number of data points was the mild group, because the focus of bTBI research has been on mild bTBI. The second largest group was the severity not explicitly given group. This group was plotted to show the areas were bTBI studies have been conducted and determine the likelihood of bTBI based on the relationship produced in this research. The moderate and severe severity groups had the least number of data, because lung protection is required to prevent lung injury. Without lung protection, the brain will sustain secondary injuries from reduced oxygen [61, 109, 116]. From Figure 4.1, the spread of the mild bTBI data points is diverse allowing for a good understanding of the mild bTBI. Note: pressure will be on the x-axis and impulse will be on the y axis for the rest of this dissertation, although both orientations are acceptable and data published with axis titles switched. However, the moderate and

severe bTBI data points are linear, due to the use of shock tubes. Thus, more testing needs to be conducted on moderate and severe bTBI to produce a more definitive ranges.
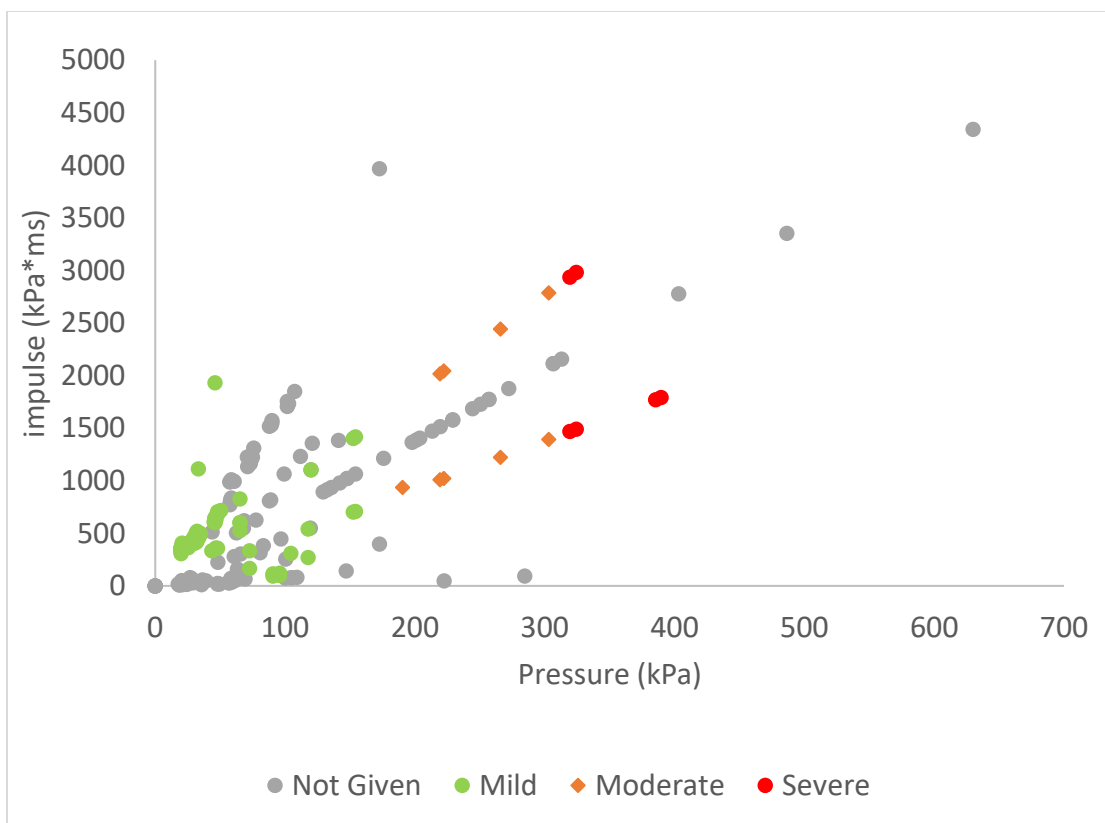
Figure 4.1. Human bTBI P-I graph with severities denoted

The three explicitly given severities had no overlapping data points on Figure 4.1, thus each bTBI severity has a distinct region based on the relationship between pressure and impulse. The region for each severity began at the lowest peak pressure and the lowest impulse occurrence, as shown in Figure 4.2. A log-log graph was used to present the severity regions, so the spread of the data could be visualized easier. The mTBI region

began with the lowest occurrence of a bTBI in the unspecified group, since an injury was documented. The author assumed the "not given" data points in this region were mild bTBIs. The other "not given" data points were assigned the severity of the data points in close proximity. Boxes were used to assign severity regions instead of curves discussed in Section 2.1.6 because the dynamic region of the severities are not known and produces a more conservative model. The beginning point of each severity region for humans is given in Table 4.3. Unlike other P-sT bTBI graphs that give a finite range, the starting point is only given, due to severity regions extending along both axes. These severity regions will be referred to in the following section (Section 5). These severity regions are conservative, since Jean's pressure scaling is conservative. Upon further examination of Figure 4.2, six regions of under researched areas were found, which were: greater than 100 kPa and lower than 75 kPa*ms; greater than 20 kPa and 4,000 kPa*ms; greater than 300 kPa and 100 kPa*ms; boundaries between no bTBI and mild; boundaries between mild and moderate; and boundaries between moderate and severe. Testing is not feasible, however, for low pressure and high impulse or high pressure and low impulse regions, as these values are difficult to achieve experimentally. These regions have not, to the author's knowledge, been previously identified.

Table 4.3. Thresholds for each human bTBI severity region

	Threshold	
	Pressure (kPa)	Impulse (kPa*ms)
mild	17.7	7.2
moderate	190	935
severe	319	1467
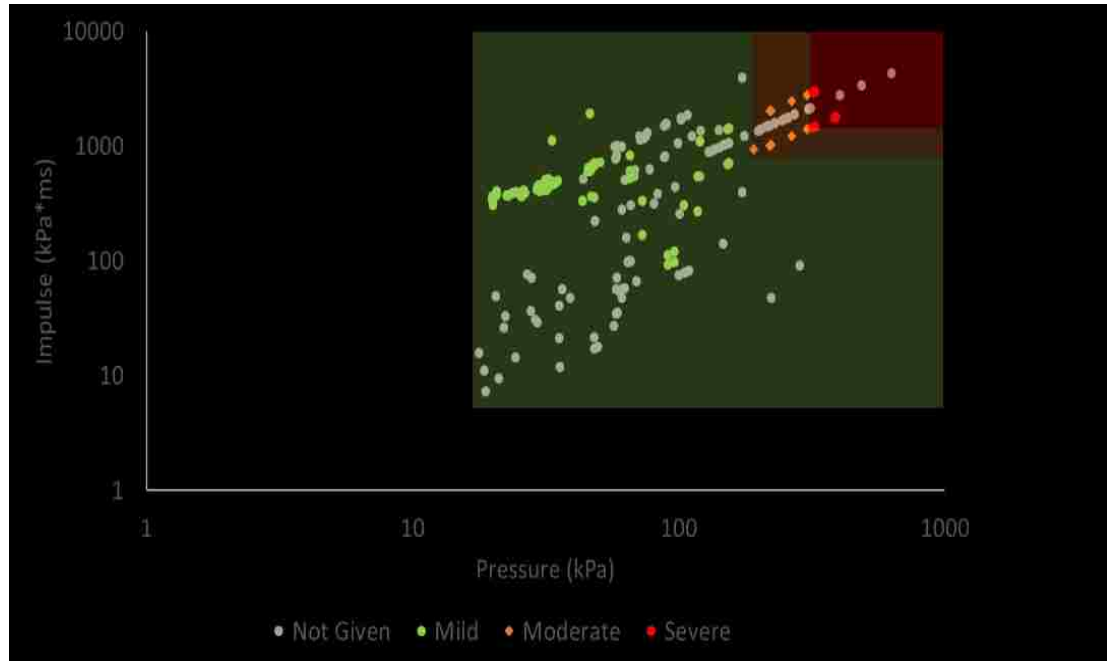
Figure 4.2. Human bTBI P-I graph with severity region identified

4.4. SUMMARY

The human bTBI P-I graph with proposed severity regions defined was developed in this section. The severities were determined from scaled animal bTBI studies that explicitly stated the severity of the bTBI and grouped other that were unspecified. The influence of impulse has been overlooked in the search of understanding the mechanisms of bTBI. The peak pressures were scaled by using the method proposed by Jean et al. [12]. The impulse scaling was conducted by using mass scaling on the time duration. The proposed bTBI regions will be used in the following section to determine the correlation between observable blast injuries (eardrum rupture and lung damage) and the occurrence of bTBIs, see Appendix B Table B.1 for all calculated values.

5. HUMAN bTBI RELATIONSHIP TO PHYSIOLOGICAL INJURIES (OBJECTIVE 3)

Explosive blasts detonated in the vicinity of animals or people can cause injuries to air-containing organs. The three most susceptible structures are bowels, lungs, and ears. However, lung damage and eardrum rupture are more observable than the bowel injuries. Observable lung injury symptoms are labored breathing, coughing, coughing up blood and chest pain [120]. Eardrum rupture is observed from discharge from the ear canal and hearing loss [119] As a result, numerous studies have been conducted to understand and define injury regions, which were discussed in Section 2.2. This section is divided into four subsections: lung damage, eardrum rupture, bTBI correlation to observable injuries, and summary of the section. The lung damage subsection discusses the processes used to create a P-I graph from the data presented in Section 2.3.1. The eardrum rupture subsection presents a P-I graph with different eardrum rupture regions from literature. The correlation subsection discusses correlations between the proposed bTBI P-I graph presented in Section 4.3. The summary subsection briefly recaps the correlations observed in the previous subsection. The overall goal of this section is to show that human bTBI regions can be related to observable blast induced injuries as a diagnostic tool on the battlefield.

5.1. LUNG INJURY

The blast effects on lung tissue has been greatly studied [10, 80, 81, 110, 121, 125]. As a result, improved body armor has been developed and the prevalence of lung injury has reduced in recent years. The same cannot yet be said for bTBI. Courtney and Courtney [110] produced a P-T graph for lung lethality curves from Bowen et al.'s [10] work. Baker et al. [80, 81] also used Bowen et al.'s [10] work to produce a 50% lung lethality P-I graph.

This researcher inferred data points from both graphs and were used to create a lung damage P-I graph for the four lung damage and lethality curves: threshold for injury, 1% lethality, 50% lethality, and 99% lethality. The impulse was calculated using Equation (8) with the inferred peak pressure and time duration values. The produced P-I 50% lethality curve was compared to the values given by Baker et al. [80, 81] in Figure 2.16 and Table 2.3. The inferred 50% lethality curve was found to have very similar values and further explained in Appendix C. The resulting lung damage and lethality P-I is shown as a log-log plot in Figure 5.1. The circle curve denotes the threshold for lung damage. The triangle curve denotes the region of 1% chance of lethality. The square curve denotes the 50% chance of lethality. The diamond curve denotes the area where 99% lethality occurs. Bass et al. [61] reported that these curves would shift up and to the right if a protective vest is worn. The curves presented in Figure 5.1 will be used for comparison with the proposed bTBI severity P-I curves in Section 5.3.
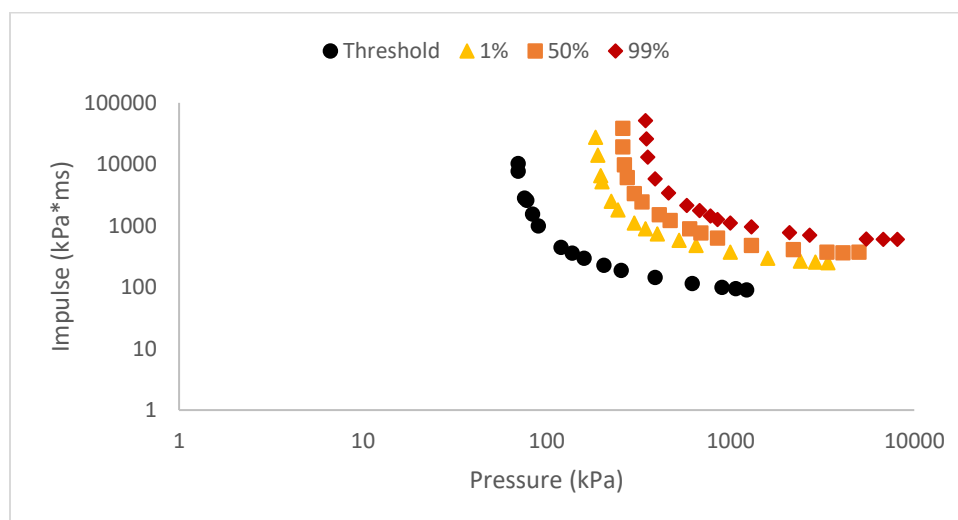
Figure 5.1. P-I lung damage curve for 70 kg man, calculated from Courtney and Courtney [110] and Baker et al. [80, 81]

5.2. EARDRUM RUPTURE

As with lung damage, studies have been conducted on eardrum rupture after an explosive blast [81, 124–126]. Unlike the lung damage P-I curves, the tympanic membrane (eardrum) ruptures at a minimum pressure and over large range of impulse values. The eardrum rupture from Section 2.3.2 (Figure 2.17) was redrawn to have the same axes as the proposed human bTBI P-I graph (Figure 4.2) and is given in Figure 5.2, where EDR is eardrum rupture. The triangle dotted line represents the threshold for eardrum rupture. The circle dotted line represents the 50 percent threshold for eardrum rupture. These two thresholds for eardrum rupture will be used in the comparison between human bTBIs and observable injuries in the following section (Section 5.3).
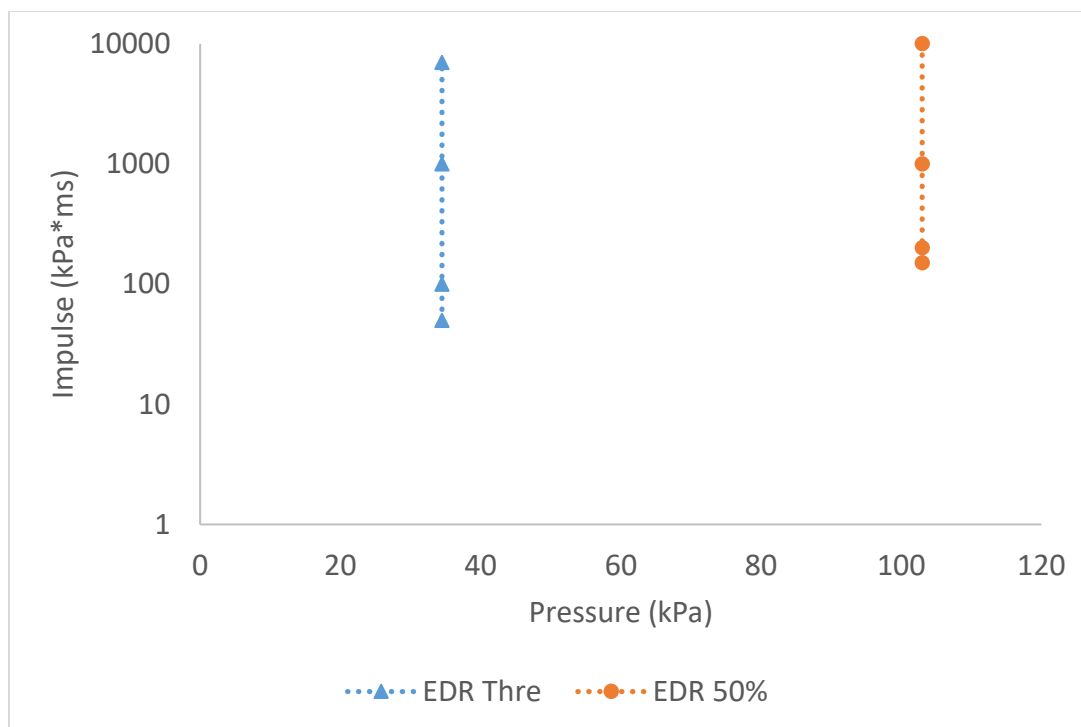
Figure 5.2. P-I curve for eardrum rupture, adapted from Baker et al. [81]

5.3. HUMAN bTBI SEVERITY REGIONS WITH PHYSIOLOGICAL INJURY P-I CURVES OVERLAID (OBJECTIVE 3)

The proposed human bTBI P-I graph from Section 4.3 was combined with the lung lethality curves from Section 5.1 and thresholds for eardrum rupture from Section 5.2. The bTBI severity regions were overlaid on the graph of observable physical injuries resulting in Figure 5.3.
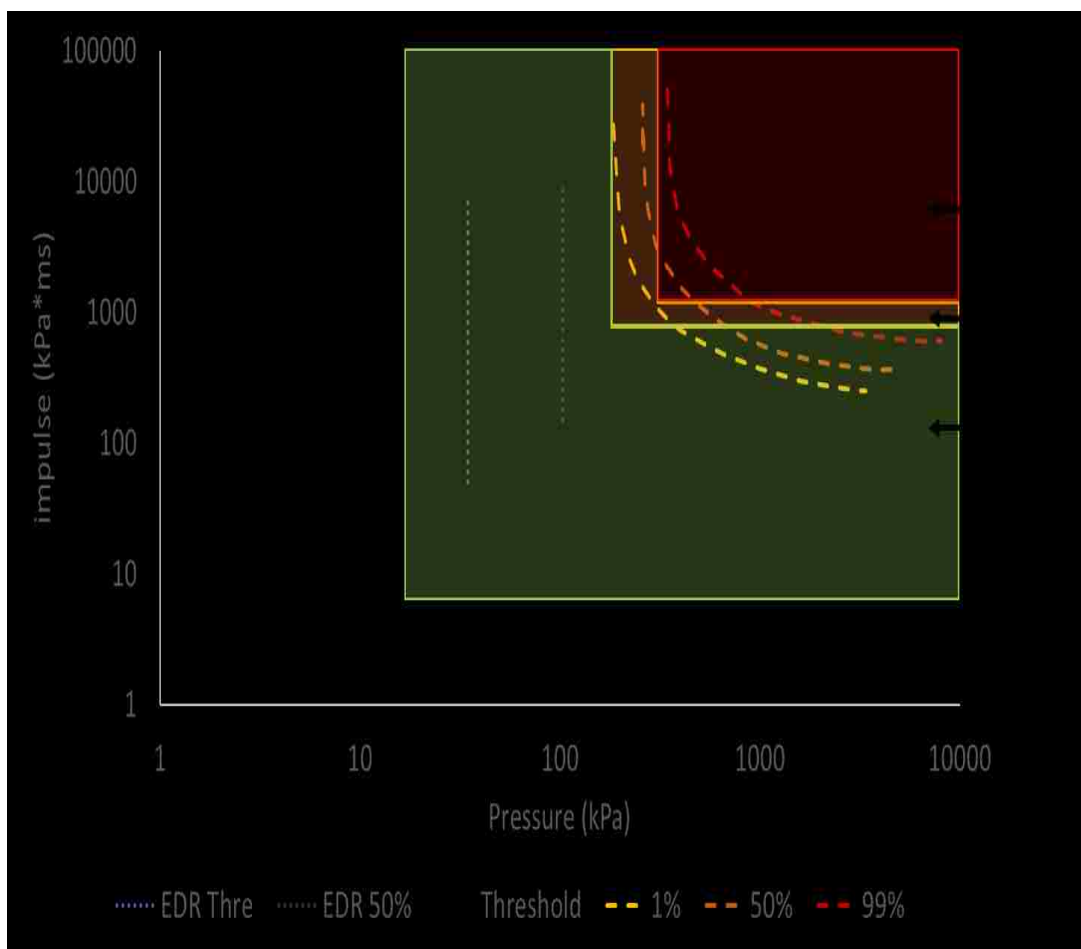
Figure 5.3. Human bTBI P-I graph with eardrum rupture and lung lethality curves overlaid

Several correlations can be from the produced graph.

1. mTBI occurs before eardrum rupture, which is consistent with White et al.'s findings [125]. Thus, eardrum rupture implies that an individual has a bTBI after a blast.

2. Lung injury is in the mTBI region. The mTBI region encompasses the majority of the threshold for lung injury region.

3. modTBI region encompassed the pressure sensitive regions of the 1 and 50% lung lethality curves.

4. mTBI region included the impulse sensitive region of the 1 and 50% lung lethality curves.

5. modTBI region contained the impulse sensitive region of the 99% lung lethality curve.

6. sTBI region contained the dynamic region of the 50% lung lethality curve.

7. sTBI region contained the pressure sensitive and dynamic regions of the 99% lung lethality curve.

These observed correlations indicate that physical injuries can be used as a guide in determining if a bTBI was acquired after an explosive blast.

By further examining the observed correlations, practical applications can be applied to the battlefield and urban environments. The correlations with the bTBI regions allow the individuals subjected to an explosive blast to quickly determine if they likely sustained a bTBI and seek appropriate medical attention. The occurrence of individuals

with ruptured eardrums and lung injury after a blast could be used as an indicator that the individuals in the area may have sustained a bTBI. However, if a few individuals perished, the surviving individuals may have a modTBI. If a large number of individuals have perished, the surviving individuals in close proximity would likely have lung injuries and either modTBI or sTBI. The individuals at a further distance may have sustained an mTBI. The ability to quickly associate a visible injury to a bTBI would allow for earlier treatment of individuals with a suspected bTBI and possibly reduce the long-term effects of the bTBI.

5.4. SUMMARY

The proposed human bTBI P-I severity regions were found to have seven correlations with known P-I curves for both lung damage and eardrum rupture. The ability to correlate an "invisible" injury to an observable injury in the same individual would further the understanding of the effects bTBIs after blast exposure. The correlations would also allow for individuals subjected to an explosive blast to receive appropriate medical treatment earlier and possibly reduce the long-term effects of the bTBI.

6. CONCLUSIONS

A signature wound of the current military conflicts is bTBI. Currently, the diagnosis of bTBIs is difficult, due to few observable symptoms as described in Section 1.2. This research was conducted to determine if correlations between the occurrence of bTBIs and observable physical injuries exist after an explosive blast, thus allowing for affected individuals to receive appropriate medical treatment. To achieve this goal, three objectives were identified. Objective 1 was to identify and develop impulse calculation equations for all animal bTBI testing methods. Objective two was to create a human bTBI P-I graph based on published animal bTBI data. Objective three was to correlate the human bTBI severity regions to observable blast injuries. Dr. Johnson's research team has been studying bTBI since 2015 publishing 85 [88, 89, 127, 128] of the 258 total data points on bTBI studies published to date. Experimental testing was also conducted to determine an impulse calculation equation for animals placed outside a shock tube. The equation allowed for the accomplishment of the objective. The following sections summarize the significance and conclusions identified for each of the three objectives.

6.1. IMPULSE EQUATION MODIFICATION

The Friedlander impulse equation (Equation (8)) was found not to estimate the impulse of a shock wave outside a shock tube in the jet wind region. When the shock wave exits the shock tube, a vortex ring forms thus increasing the duration of the shock wave. Experimental testing was conducted to develop and validate an equation to calculate impulse outside the shock tube and discussed in Section 3.2.

Upon analysis of the results, the vortex ring was found to extend the positive phase of the shock wave up to 9 times the duration inside the shock tube or beyond the vortex ring. The vortex ring had a slower velocity than the shock wave. The Rutter-Johnson equation (Equation (31)) was developed to account for this distance, which was found to be 60% of the shock tube diameter. Three equivalents were found to influence the separation of the shock wave and vortex ring were:

- ratio of gas production to TNT production

- mass of the equivalent amount of explosives

- density ratio to TNT

The Rutter-Johnson equation was found to reduce the error up to 66 % of the traditional Friedlander impulse equation outside a shock tube when within 60% of the shock tube diameter from the end of the shock tube.

6.2. HUMAN bTBI SEVERITY REGIONS

The data presented in Table 2.1 was converted from the animal models to humans using two different scaling methods. The reported peak pressure of the animals studied was scaled to humans using Jean et al.'s scaling method [12], which accounts for all the structures of the head including mass of the skull, mass of the brain, and mass of the surrounding soft tissue. An impulse scaling equation was developed to plot the impulse data on a P-I graph. The impulse scaling equation consisted of multiplying the scaled peak pressure (Jean et al.'s scaling method [12]) and scaled time duration (mass scaling method Equation (14)) and diving by the exponential to the β value, which is the impulse modifier.

Upon examination of the human bTBI P-I graph, five under researched regions were observed: greater than 100 kPa and lower than 75 kPa*ms, greater than 20 kPa and 4000 kPa*ms, greater than 300 kPa and 100 kPa*ms, boundary between mild and moderate, and boundary between moderate and severe.

6.3. CORRELATIONS BETWEEN bTBI SEVERITIES AND OBSERVABLE INJURIES

The human bTBI P-I graph with defined severity regions was overlaid with P-I curves for lung damage and eardrum rupture. Severn correlations were observed between the bTBI severity regions and observable physical injuries.

1. mTBI occurs before eardrums rupture

2. mTBI region encompasses majority of the threshold for lung injury region

3. mTBI region included the impulse sensitive region of the 1 and 50 percent lung lethality curves

4. modTBI region encompassed the pressure sensitive regions of the 1 and 50 percent lung lethality curves

5. modTBI region contained the impulse sensitive region of the 99 percent lung lethality curve

6. sTBI region contained the dynamic region of the 50 percent lung lethality curve

7. sTBI region contained the pressure sensitive and dynamic regions of the 99 percent lung lethality curve

Based on these correlations, a bTBI is very likely to be sustained by an individual subjected to an explosive event, whose unprotected eardrums ruptured. Moderate and severe bTBIs are likely sustained by individuals in close vicinity of deceased individual after an explosive event. Whilst survivability has increased due to improved body armor and hearing protection, the occurrence of bTBIs have increased.

6.4. CONCLUSIONS

One of the signature wounds of the current military conflicts is bTBI. This research has proposed using a P-I graph to identify the regions for each type of severity, never previously published.

- A P-I graph can be used to present bTBI data with 3 clear distinctions for mild, moderate and severe TBIs.
- Rutter-Johnson equation was developed to determine impulse outside of a shock tube.
- The minimum distance where the shock wave and vortex ring separate from one another at 60% of the shock tube diameter.
- The vortex ring was found to be influenced by the shock wave's source gas production, density, and mass in relation to TNT.
- The jet wind region was quantified.
- bTBIs can be correlated to observable blast injuries.
- Mild bTBI can be sustained without any visible indicator.

7. FUTURE WORK

Future research is needed to refine the severity regions for bTBI proposed by this dissertation. To achieve defining severity regions, testing needs to be conducted in the areas with little data on the P-I graph. Higher impulses need to be studied as well to determine the lethal limit. To achieve these higher impulses, shock tubes and shock tunnels need to be constructed to sustain pressures over a long positive phase duration. Testing needs to be conducted to determine the dynamic regions of the bTBI severities. An impulse scaling factor is also needed to more accurately represent the loading that the brain experiences.

The produced P-I graph can be used by all researchers to add their bTBI data with the goal of diagnosing and treating bTBIs. Also, the P-I graph can be used to determine if correlations exist between bTBIs and building damage after an explosive blast, in addition to the human observable injuries studied in this research.

Future research is needed to determine the effect that helmets have on the proposed human bTBI P-I graph. Since helmets are worn by members of the military and police, the P-I graph needs to account for this added layer of protection. The research will need to determine if the helmet is added to Jean et al.'s scaling parameter or the pressure and impulse thresholds modified.

The influence of the detonating cap on the explosives needs to be further investigated. A single cap test was conducted in this research, as shown in Figure 7.1. This pressure trace was the result of the cap and the pentolite stinger not being properly coupled. As with the other pentolite tests conducted at 6 cm the duration is extended at a low pressure.
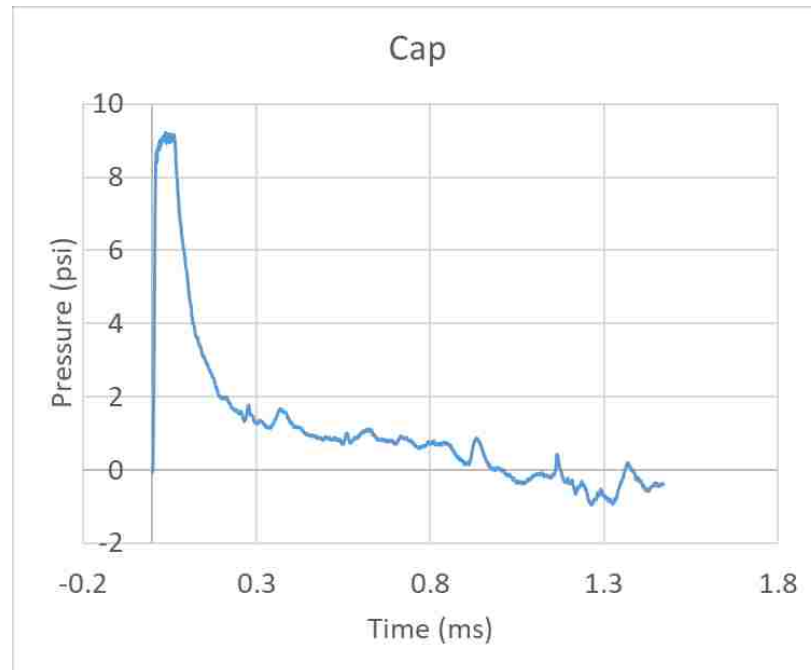
Figure 7.1. Pressure trace of cap measured at 6 cm outside the shock tube

APPENDIX A.

DATA TO ACCOMPANY SECTION 3

This appendix provides the recorded weight, peak pressure, time durations and impulses used for the calculations of β and the expanded Table 3.12. Pentolite stingers were used in this research, because they were commercially available. Before testing began, 30 pentolite stingers were weighed to ensure the mass of explosives was the same. The pentolite stingers were encased in plastic. All the stingers used in this research were 12 g, where 10 g were the pentolite and 2 g were the plastic chasing to ensure that all the stingers had the same weight. The C4 charges were weighed before each test to ensure each charge was 4.3 g. The impulse was determined by the midpoint approximation method on each of the recorded pressure traces. The peak pressure, positive phase time duration, and impulse values for all experimental testing are shown in Table A.1. The peak pressures remain relatively constant for the four distances measured, which is consistent with Giannuzzi et al.'s work [26]. The characteristics of the sensors used in this research were taken from the PCB website and published specification sheets [129–131].The time duration steadily decayed until the shock wave and vortex ring separated from one another. A similar trend to the time duration was observed with the calculated impulse at the distance where the vortex ring was no longer influencing the shock wave.

The expanded Table 3.12, shown in Tables A.2 (pentolite) and A.3 (C4), displays the values for impulse calculated using three different methods and the percent error between them. The first method was the midpoint approximation method (Equation (5)), which provides closest value to the actual impulse value. The midpoint approximation method values were used as the baseline for comparison for the other two methods. The second method was the integration of the traditional Friedlander pressure equation (Equation (8)), which is the current method to calculate impulse when peak pressure and

positive phase time duration are only given. The third method used was the proposed

equation from Section 3.4 (Equations (30) and (31)), which estimates the decay rate of the

pressure trace with the given peak pressure, time duration, distance outside the shock tube,

rupture pressure, and the volume of air in the shock tube between the shock wave source

and the end of the shock tube. The proposed method reduces the error of the Friedlander

method greatly. The most drastic error reduction was found to occur when the vortex ring

was influencing the end of the shock wave.

Table A.1. Recorded peak pressures, time durations, and calculated impulses

explosive	distance	experiment	P (psi)	T (ms)	I (psi*ms)
Pentolite	0	1	50.6727	2.1825	37.79453
		2	47.381	2.3585	37.57377
		3	47.1381	2.2675	39.52465
	3	4	51.9646	1.851	29.97359
		5	47.7127	1.9575	27.04682
		6	47.9587	1.833	29.21142
	6	7	48.5269	0.822	9.072208
		8	46.2843	0.7465	7.563371
		9	45.6526	0.8925	9.400715
	9	10	46.9175	0.2685	5.075643
		11	48.1968	0.263	5.311055
		12	43.7877	0.2865	4.628384
C4	0	1	26.7402	1.948	16.54909
		2	27.9734	1.875	16.83731
		3	29.0304	1.9135	18.34129
	3	4	27.4385	1.308	9.445778
		5	27.1687	1.384	9.693903
		6	25.2467	0.9005	6.779982
	6	7	29.9192	0.361	4.569728
		8	28.7844	0.361	4.219427
		9	28.3241	0.339	4.228745
	9	10	28.2654	0.336	3.411553
		11	27.0624	0.3405	3.34777
		12	26.5323	0.345	3.337972

Table A.2. Comparison between Pentolite Friedlander and Rutter-Johnson methods percent error

Distance (cm)	Midpoint	Friedlander	Percent error	Rutter-Johnson	Percent error
		Pentolite			
0	37.795	40.685	7.65%	40.685	7.65%
0	37.574	41.110	9.41%	41.110	9.41%
0	39.525	39.321	0.52%	39.321	0.52%
3	29.974	35.385	18.05%	29.366	2.03%
3	27.047	34.359	27.04%	28.514	5.43%
3	29.211	32.340	10.71%	26.838	8.12%
6	9.072	14.674	61.75%	8.852	2.43%
6	7.563	12.711	68.06%	7.668	1.38%
6	9.401	14.989	59.45%	9.042	3.81%
9	5.076	4.634	8.70%	4.634	8.70%
9	5.311	4.663	12.20%	4.663	12.20%
9	4.628	4.615	0.29%	4.615	0.29%

Table A.3. Comparison between C4 Friedlander and Rutter-Johnson methods percent error

Distance (cm)	Midpoint	Friedlander	Percent error	Rutter-Johnson	Percent error
		C4			
0	16.549	19.163	15.79%	17.209	3.99%
0	16.837	19.295	14.60%	17.328	2.91%
0	18.341	20.436	11.42%	18.352	0.06%
3	9.446	13.203	39.78%	9.509	0.67%
3	9.694	13.833	42.70%	9.962	2.77%
3	6.780	8.364	23.36%	6.023	11.16%
6	4.570	3.973	13.05%	3.973	13.05%
6	4.219	3.823	9.40%	3.823	9.40%
6	4.229	3.532	16.47%	3.532	16.47%
9	3.412	3.494	2.41%	3.494	2.41%
9	3.348	3.390	1.26%	3.390	1.26%
9	3.338	3.367	0.88%	3.367	0.88%

APPENDIX B.

DATA TO ACCOMPANY SECTION 4

This appendix discusses the calculations used in Section 4. The calculations discussed are converting reflective pressure to incident pressure, the calculation of β for the external shock tube tests, and completion of Table 2.2 resulting in Table 4.1. One example will be given for reflective to incident pressure calculation and β, since all calculations were conducted in the same manner.

The reflective pressures reported by Turner et al. [96] and Wang et al. [48] were converted to incident pressures using Equations (2) and (3) from Section 2.1.1. In order to use Equation (3), the values for q, given in Figure 2.7, had to be estimated for the reported peak reflective pressures. The estimated q values were determined by using the example Swisdak [35] provided on page 100. The following calculations are representative of all reflective to incident pressure conversions. Equation 1 is the estimation of the dynamic pressure for the reported peak pressure.

$$q = \frac{(31.47 - 25.1) * (4.77 - 2.21)}{(41.45 - 25.31)} + 2.21 = \frac{15.7}{16.14} + 2.21 = 3.187 \, psi \quad (1)$$

The numerator of Equation (1) is the difference between the reported reflective pressure and closest reflective pressure in Figure 2.7 multiplied by the difference in dynamic pressures in the desired region. The denominator of Equation (1) is the difference in reflective pressures in desired region of Figure 2.7. The resulting value is added to the lower tabulated dynamic pressure. The resulting value from Equation (1) is inserted into

Equation (2) resulting in the estimated incident peak pressure. The resulting value was then converted to kilopascals to be used in Figure 4.1 and Figure 4.2. The same calculations were used for all the reported peak reflective pressure listed in Table 2.1

$$P = \frac{31.47 - (1.4 + 1) * 3.187}{2} = \frac{31.47 - 7.649}{2} = 11.91 \ psi \qquad (2)$$

The following example paragraphs explain the methods used to determine the β decay of Equation (31) for studies that placed the animal subject outside the shock tube. The β value was determined in two different methods. The first method used Equation (32), when peak pressure, positive phase time duration, and impulse were reported. The second method used the proposed equation to determine the β value. The first method was used for Shridharani et al. and Beamer et al.'s [51, 109] studies. The second method was used for Kabu et al., Long et al., Budde et al., Svetlov et al., Kuehn et al., and Turner et al.'s [95, 96, 100, 104, 105, 107] studies.

Numerous steps were required to determine the β value in the second method. First the detonation velocity had to be determined. For the gas driven shock tubes, the rupture pressure was converted to velocity using Equation (4), as the velocity at the rupture pressure was assumed to be the detonation velocity. The method to determine the velocity at pressures not listed in Figure 2.7 was calculated similar to the dynamic pressure seen in Equation (1). The second step was to determine the volume in both the driver and driven

sections of the shock tube. The third step was determining the moles of gas in driver section of the shock tube. The ideal gas equation, Equation (3), was used to determine the number of moles in the driver section. The fourth step was to determine the mass of the gas, which was calculated from the grams per mole ratio for the specific gas used in the study. The fifth step was to determine the density of the gas, which was calculated by dividing the mass by the volume of the driver section of the shock tube. The sixth step was to insert all the values in Equation (30). These steps allowed for the calculation of β.

$$n = \frac{PV}{RT} \tag{3}$$

The missing rat and goat values in Table 2.2 were calculated in different manners. For the rat, the ratio of the skull to surrounding soft tissue was assumed to be the same. The ratio was used to estimate the mass the soft tissue surrounding the skull of a rat. The ratio and resulting soft tissue mass for the rat are given in Equation (4). The resulting value and other tabulated values were used to calculate η by using Equation (16). The goat η value was determined by inputting the goat values given in Table 2.2 into Equation (16). These calculations allowed for the values of η to be determined for use in Equation (17), which are given in Table 4.1.

$$M_{rat\ flesh} = \frac{M_{rat\ skull} * M_{mouse\ flesh}}{M_{mouse\ skull}} = \frac{3.19 * 1.876}{0.74} = 8.087\ g \qquad (4)$$

Table B.1. Data points in Figure 4.1

Not Given		Mild		Moderate		Severe	
222.5898	47.63921	19.88978	409.087	222.4901	1021.85	324.4876	1490.303
58.4753	70.87128	19.88978	409.087	219.3805	1007.568	319.5121	1467.452
36.42167	57.01677	19.93735	431.6389	222.4901	2043.701	324.4876	2980.606
26.94898	76.96336	19.96025	411.2269	219.3805	2015.137	319.5121	2934.903
57.36629	988.0173	19.99358	390.5223	303.3418	1393.185	389.7908	1790.227
58.61016	1009.44	19.99358	394.2741	266.0256	1221.8	385.4372	1770.232
71.04887	1223.672	20.01658	397.3289	303.3418	2786.37		
76.02435	1309.364	20.01658	398.9981	266.0256	2443.599		
88.15209	1518.24	20.08599	412.9318	190.6946	935.8669		
90.0179	1550.375	20.13653	416.0585				
101.8347	1753.895	20.13653	416.0585				
107.4321	1850.299	20.26139	445.4182				
43.81654	513.1624	20.44781	404.9391				
60.95532	993.8402	20.55456	420.0626				
284.8136	91.43474	20.65976	459.1994				
69.3097	66.3495	20.65999	440.5703				
35.56321	21.4047	22.54756	480.5184				
39.11547	47.91882	22.54756	480.5184				
29.34675	28.88913	22.8954	497.5603				
27.86664	36.4322	22.8954	497.5603				
35.56321	40.76019	23.69606	538.5964				
57.98822	800.3147	24.4779	555.9591				
58.29919	817.9943	25.40533	534.1749				
58.61016	835.8167	25.40533	533.9219				
57.83274	770.2794	25.59167	527.911				
57.98822	785.6667	25.59167	527.4724				
58.14371	801.1254	25.95155	494.0776				
71.35983	1132.344	26.1534	510.7892				
73.22564	1178.766	26.20256	522.6792				
75.09145	1226.046	26.43911	504.5283				
73.22564	1160.269	29.15914	604.5496				
73.84758	1187.082	29.61121	592.6676				
74.46951	1214.181	29.61121	592.6676				
89.39596	1529.399	29.73126	586.5671				
90.0179	1571.046	29.96772	554.8263				
102.7676	1732.203	30.29201	598.2252				
101.8347	1707.124	30.53876	594.6462				
24.40851	14.51518	30.53876	594.6462				
22.3016	33.15561	30.59703	584.407				
18.61451	11.06962	30.70375	562.9414				
21.07257	9.398526	30.70375	559.0201				

Table B.1. Data points in Figure 4.1 (Cont.)

21.95045	26.10685	30.77683	566.5532				
20.54584	48.87254	30.86205	568.734				
17.73663	15.82134	30.86205	568.6431				
18.79008	7.263117	30.94111	541.1649				
68.62267	620.4124	30.94111	540.6845				
99.29207	1064.446	31.02736	578.5702				
111.9206	1230.826	31.07418	552.3165				
120.9411	1357.212	31.09597	563.9841				
141.237	1383.226	31.13093	570.5446				
120.1818	1103.939	31.27979	574.2387				
119.588	549.2425	31.30342	584.5344				
80.80023	315.4337	31.34959	537.5695				
100.0817	74.78148	31.36523	574.5238				
59.5237	54.91285	31.44562	563.9394				
147.1361	141.1061	31.44737	555.2467				
49.69145	17.84285	31.44826	575.1381				
56.89006	26.94207	31.46531	578.5662				
48.11127	21.49604	31.51878	559.016				
62.68407	58.1547	31.53522	536.4274				
48.11127	17.32517	31.58109	568.6249				
60.92831	56.42301	31.59286	535.0473				
35.82095	11.82809	31.59286	537.4424				
57.94352	57.03216	31.67801	581.3054				
65.84444	100.0092	31.74279	537.0657				
64.26425	97.44605	31.75242	554.7412				
64.79098	98.02578	31.93418	575.2939				
58.99697	35.08697	32.0163	607.0374				
104.9979	78.90914	32.06166	526.9995				
109.2117	81.779	32.06166	525.568				
65.14213	98.79873	32.06761	549.8534				
104.9979	78.66873	32.06761	550.7897				
58.11909	34.42906	32.09823	545.9045				
60.95532	279.955	32.09823	546.0752				
88.01656	808.4831	32.16197	573.9382				
172.8084	396.8364	32.22143	595.463				
88.9186	816.7688	32.28885	551.0075				
172.8084	3968.364	32.3602	544.4826				
272.484	1877.192	32.5425	540.6875				
257.1493	1771.549	32.5508	574.1753				
229.186	1578.905	32.60957	574.9443				
198.0656	1364.51	33.11033	555.0941				
148.0023	1019.615	33.21613	532.3914				
201.2227	1386.26	33.21613	531.8511				
175.9656	1212.259	33.58722	569.7098				
154.3166	1063.115	34.13896	534.6852				
148.0023	1019.615	34.20139	565.2763				
142.139	979.2219	35.12596	572.5327				
129.5104	892.2214	43.59877	376.6674				
135.8247	935.7216	45.31711	586.5621				
132.6676	913.9715	45.82251	560.2598				
630.1433	4341.173	46.15815	593.5098				

Table B.1. Data points in Figure 4.1 (Cont.)

486.7187	3353.095	46.16737	571.1136				
403.2799	2778.27	46.42601	558.0325				
306.7615	2113.337	46.91357	380.3048				
229.186	1578.905	46.92784	610.6489				
313.0758	2156.837	47.3387	549.8922				
306.7615	2113.337	48.0076	374.1793				
257.1493	1771.549	48.12057	560.3279				
250.835	1728.048	48.27814	567.9029				
244.5207	1684.548	50.47215	567.7485				
219.7146	1513.654	46.20695	1931.191				
213.4003	1470.154	33.39797	1112.076				
203.9288	1404.903	72.68186	166.9062				
28.93287	30.56299	72.68186	333.8125				
60.95532	47.59235	117.7839	270.4784				
62.75941	504.4213	117.7839	540.9567				
68.17165	547.9216	65.46553	526.1715				
77.64308	624.0471	65.46553	826.8409				
48.381	222.2037	65.46553	601.3388				
65.95694	302.9264	65.46553	601.3388				
83.36675	382.8859	90.77622	92.31008				
96.94041	445.2269	96.0435	97.66636				
27.99646	70.86645	90.77622	113.3633				
63.37341	160.4149	96.0435	119.9411				
100.4862	254.3573	120.1818	1103.939				
30.93468	78.30389	154.3882	709.0726				
24.96655	63.19695	152.5224	700.5033				
45.53245	115.2547	154.3882	1418.145				
79.29417	200.7146	152.5224	1401.007				
76.73963	194.2483	104.4576	307.5542				
121.6005	307.803						

APPENDIX C.

DATA TO ACCOMPANY SECTION 5

This appendix details the methods used to create the lung damage P-I curves in Figure 5.1 and how the overlay was applied on Figure 5.3. The lung damage P-I curves were created by estimating numerous points on the P-T graph shown in Figure 2.15. The points were estimated by overlaying an Excel graph with the same dimensions and axes, as shown in Figure C.1. Points were plotted on the Excel graph and compared to the lung damage curves. This method was used for the four P-T curves. The Friedlander impulse equation, Equation (8), was used to determine the impulse value. The created 50% P-I curve was compared to the data points presented in Table 2.3 from Baker et al. [80, 81] and found to be representative of the data. Thus, the lung P-I graph was determined to be a good representation of lung damage.

Figure C.1. P-T lung damage graph [110] with Excel P-T graph overlaid with points on the curves

The overlay was applied on Figure 5.3 by plotting the lung damage and eardrum rupture P-I curves on an Excel graph. The threshold points for each bTBI severity, shown in Table 4.3, were also plotted on the P-I graph, as shown in Figure C.2. The threshold points served as the corners of the severity regions, as the dynamic regions have yet to be defined. The mild and moderate severity regions were defined by an "L" shape beginning at the threshold point and extended to the next threshold point. For the severe severity region, a rectangular shape was used, as the lethality region has yet to be defined. Each severity region extends indefinitely in both pressure and impulse between threshold points, as this is the nature of a P-I curve.
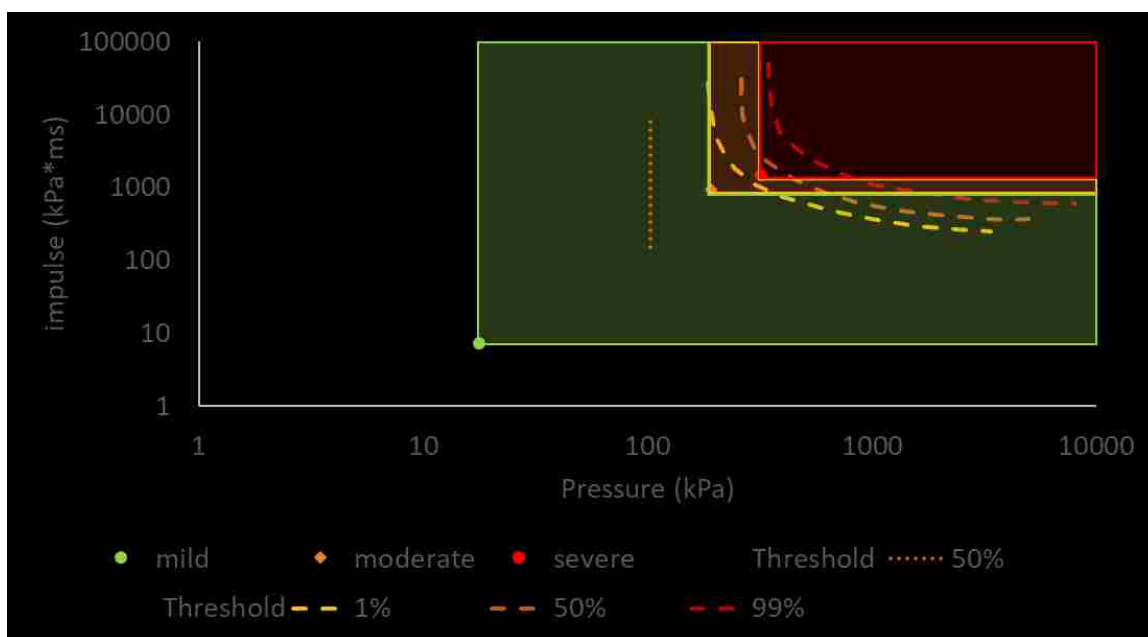

Figure C.2. Human bTBI P-I graph with threshold for each severity shown overlaid with observable injuries

REFERENCES

1. DePalma, R.G., Burris, D.G., Champion, H.R., Hodgson, M.J.: Blast Injuries. N. Engl. J. Med. 352, 1335–1342 (2005). doi:10.1056/NEJMra042083

2. DePalma, R.G.: Combat TBI: History, Epidemiology, and Injury Modes. In: Kobeissy, F.H. (ed.) Brain Neurotrauma: Molecular, Neuropsychological, and Rehabilitation Aspects. CRC Press/Taylor & Francis, Boca Raton, FL (2015)

3. Benzinger, T., Brody, D., Cardin, S., Curley, K., Mintun, M., Mun, S., Wong, K., Wrathall, J.: Blast-related brain injury: Imaging for clinical and practical applications: Report of the 2008 St. Louis workshop. J Neurotrauma. 26, 2127–2144 (2009). doi:10.1089/neu.2009.0885

4. Faul, M., Coronado, V.: Epidemiology of traumatic brain injury. In: Grafman, J. and Salazar, A.M. (eds.) Handbook of Clinical Neurology. pp. 3–13. Elsevier (2015)

5. Rao, V., Koliatsos, V., Ahmed, F., Lyketsos, C., Kortte, K.: Neuropsychiatric disturbances associated with traumatic brain injury: A practical approach to evaluation and management. Semin. Neurol. 35, 64–82 (2015). doi:10.1055/s-0035-1544241

6. Glassberg, E., Nadler, R., Erlich, T., Klien, Y., Kreiss, Y., Kluger, Y.: A decade of advances in military trauma. Scand. J. Surg. 103, 126–131 (2014). doi:10.1177/1457496914523413

7. Butler, F.K., Blackbourne, L.H.: Battlefield trauma care then and now: A decade of Tactical Combat Casualty Care. J. Trauma Acute Care Surg. 73, S395–S402 (2012). doi:10.1097/TA.0b013e3182754850

8. Butler, F.K.: Two Decades of Saving Lives on the Battlefield: Tactical Combat Casualty Care Turns 20. Mil. Med. 182, e1563–e1568 (2017). doi:10.7205/MILMED-D-16-00214

9. Centers for Disease Control and Prevention, National Institutes of Health, Department of Defense, Department of Veterans Affairs: Report to Congress on Traumatic Brain Injury in the United States : Understanding the Public Health Problem among Current and Former Military Personnel. (2013)

10. Bowen, I.G., Fletcher, E.R., Richmond, D.R.: Estimate of man's tolerance to the direct effects of air blast. (1968)

11. Zhu, F., Chou, C.C., Yang, K.H., King, A.I.: Some considerations on the threshold and inter-species scaling law for primary blast-induced traumatic brain injury: A semi-analytical approach. J. Mech. Med. Biol. 13, 1350065 (2013). doi:10.1142/S0219519413500656

12. Jean, A., Nyein, M.K., Zheng, J.Q., Moore, D.F., Joannopoulos, J.D., Radovitzky, R.: An animal-to-human scaling law for blast-induced traumatic brain injury risk assessment. Proc. Natl. Acad. Sci. U. S. A. 111, 15310–15315 (2014). doi:10.1073/pnas.1415743111

13. Rafaels, K.A.: Blast Brain Injury Risk, (2010)

14. Mays, G.C., Smith, P.D. eds: Blast effects on buildings. Design of buildings to optimize resistance to blast loading. Thomas Telford, London (1995)

15. Dawodu, S.T.: Traumatic Brain Injury (TBI) - Definition, Epidemiology, Pathophysiology: Overview, Epidemiology, Primary Injury, https://emedicine.medscape.com/article/326510-overview#a1

16. Mayo clinic staff: Traumatic brain injury - Symptoms and causes - Mayo Clinic, https://www.mayoclinic.org/diseases-conditions/traumatic-brain-injury/symptoms-causes/syc-20378557

17. Shively, S.B., Horkayne-Szakaly, I., Jones, R. V, Kelly, J.P., Armstrong, R.C., Perl, D.P.: Characterisation of interface astroglial scarring in the human brain after blast exposure: a post-mortem case series. Lancet Neurol. 15, 944–953 (2016). doi:10.1016/S1474-4422(16)30057-6

18. Ling, G., Ecklund, J.M., Bandak, F.A.: Brain injury from explosive blast: description and clinical management. In: Grafman, J. and Salazar, A.M. (eds.) Handbook of Clinical Neurology. pp. 173–180. Elsevier (2015)

19. Defense and Veterans Brain Injury Center: DOD Worldwide Numbers for TBI. (2017)

20. Centers for Disease Control and Prevention: What are the treatments for TBI?, http://www.neurology.org/cgi/doi/10.1212/WNL.0b013e3182553c38

21. Dang, B., Chen, W., He, W., Chen, G.: Rehabilitation Treatment and Progress of Traumatic Brain Injury Dysfunction, https://www.hindawi.com/journals/np/2017/1582182/, (2017)

22. Chou, A., Krukowski, K., Jopson, T., Zhu, P.J., Costa-Mattioli, M., Walter, P., Rosi, S.: Inhibition of the integrated stress response reverses cognitive deficits after traumatic brain injury. Proc. Natl. Acad. Sci. 114, E6420–E6426 (2017). doi:10.1073/pnas.1707661114

23. Tasissa, A.F., Hautefeuille, M., Fitek, J.H., Radovitzky, R.A.: On the formation of Friedlander waves in a compressed-gas-driven shock tube. Proc. R. Soc. A Math. Phys. Eng. Sci. 472, (2016). doi:10.1098/rspa.2015.0611

24. Phillips, M.: Numerical modeling and characterization of blast waves for application in blast-induced mild traumatic brain injury research, https://lib.dr.iastate.edu/etd/15789/, (2016)

25. Chandra, N., Ganpule, S., Kleinschmit, N.N., Feng, R., Holmberg, A.D., Sundaramurthy, A., Selvan, V., Alai, A.: Evolution of blast wave profiles in simulated air blasts: Experiment and computational modeling. Shock Waves. 22, 403–415 (2012). doi:10.1007/s00193-012-0399-2

26. Giannuzzi, P.M., Hargather, M.J., Doig, G.C.: Explosive-driven shock wave and vortex ring interaction with a propane flame. Shock Waves. 26, 851–857 (2016). doi:10.1007/s00193-016-0627-2

27. Arakeri, J.H., Das, D., Krothapalli, A., Lourenco, L.: Vortex ring formation at the open end of a shock tube: A particle image velocimetry study. Phys. Fluids. 16, 1008–1019 (2004). doi:10.1063/1.1649339

28. Cooper, P.W.: Explosives Engineering. Wiley-VCH, New York (1996)

29. Editors of Merriam-Webster Dictionary: Compressional Wave, https://www.merriam-webster.com/dictionary/compressional wave

30. Merriam-Webster: Pressure Wave | Definition of Pressure Wave, https://www.merriam-webster.com/dictionary/pressure wave

31. Kinney, G.F., Graham, K.J.: Explosive Shocks in Air. Springer Berlin Heidelberg, Berlin, Heidelberg (1985)

32. Sochet, I. ed: Blast effects : physical properties of shock waves. Springer International Publishing (2018)

33. Johnson, C.E.: Fragmentation Analysis in the Dynamic Stress Wave Collision Regions in Bench Blasting, https://uknowledge.uky.edu/mng_etds/16, (2014)

34. Dewey, J.M.: Measurement of the physical properties of blast waves. In: Igra O., S.F. (ed.) Experimental Methods of Shock Wave Research. pp. 53–86. Springer International Publishing, Cham (2016)

35. Swisdak Jr., M.M.: Explosion Effects and Properties Part I - Explosion in Air. , White Oak, Silver Spring, Maryland (1975)

36. Kingery, C.N., Bulmash, G.: UN - SaferGuard - Kingery Bulmash Blast Parameter Calculator, https://www.un.org/disarmament/un-saferguard/kingery-bulmash/

37. Swisdak, M.M.: DDESB blast effects computer version 6, user's manual and documentation. DDESB Tech. Pap. (2005)

38. Hi-Techniques: Synergy Operator's Manual, http://www.hi-techniques.com/, (2013)

39. Hi-Techniques: Hi-Techniques - Synergy | High Speed Data Acquisition, http://www.hi-techniques.com/products/synergy/

40. Friedlander, F.G.: The Diffraction of Sound Pulses. I. Diffraction by a Semi-Infinite Plane. Proc. R. Soc. A Math. Phys. Eng. Sci. 186, 322–344 (1946). doi:10.1098/rspa.1946.0046

41. Taylor, G.I.: The propagation of blast waves on the ground. In: Batchelor, G.K. (ed.) The Scientific Papers of Sir Geoffrey Ingram Taylor volume 3. Cambridge University Press, Cambridge (1941)

42. Dewey, J.M.: The Friedlander Equations. In: Sochet, I. (ed.) Blast Effects: physical properties of shock waves. pp. 37–55. Springer International Publishing, Cham (2018)

43. Dewey, J.M.: The shape of the blast wave: studies of the Friedlander equation. In: Proceeding of the 21st International Symposium on Military Aspects of Blast and Shock (MABS), Israel. pp. 1–9. , Israel (2010)

44. Thornhill, C.: The shape of a spherical blast wave, Armament Research and Development Establishment (ARDE) Memo.(B) 41/59. , London (1959)

45. Ben-Dor, G., Igra, O., Elperin, T. eds: Handbook of shock waves. Academic Press (2001)

46. Zhu, F.: Modeling of Blast Wave and Its Effect on the Human/Animal Body. In: Basic Finite Element Method as Applied to Injury Biomechanics. pp. 689–701. Elsevier (2018)

47. Needham, C.E.: Blast waves Propagation. In: Blast Waves. pp. 87–99. Springer Berlin Heidelberg, Berlin, Heidelberg (2010)

48. Wang, H., Zhang, Y.P., Cai, J., Shields, L.B.E., Tuchek, C.A., Shi, R., Li, J., Shields, C.B., Xu, X.-M.: A compact blast-induced traumatic brain injury model in mice. J. Neuropathol. Exp. Neurol. 75, 183–196 (2016). doi:10.1093/jnen/nlv019

49. Needham, C.E., Ritzel, D., Rule, G.T., Wiri, S., Young, L.: Blast testing issues and TBI: Experimental models that lead to wrong conclusions. Front. Neurol. 6, (2015). doi:10.3389/fneur.2015.00072

50. Panzer, M.B., Wood, G.W., Bass, C.R.: Scaling in neurotrauma: How do we apply animal experiments to people? Exp. Neurol. 261, 120–126 (2014). doi:10.1016/j.expneurol.2014.07.002

51. Beamer, M., Tummala, S.R., Gullotti, D., Kopil, K., Gorka, S., Ted Abel, Bass, C.R.D., Morrison, B., Cohen, A.S., Meaney, D.F.: Primary blast injury causes cognitive impairments and hippocampal circuit alterations. Exp. Neurol. 283, 16–28 (2016). doi:10.1016/j.expneurol.2016.05.025

52. Reneer, D. V., Hisel, R.D., Hoffman, J.M., Kryscio, R.J., Lusk, B.T., Geddes, J.W.: A multi-mode shock tube for investigation of blast-induced traumatic brain injury. J. Neurotrauma. 28, 95–104 (2011). doi:10.1089/neu.2010.1513

53. Hoffman, J.M., Lusk, B.T., Perry, K.: Investigations of Shock Tunnel Dynamics and Energy Realization. Blasting Fragm. 3, 207–226 (2009)

54. McLane, D.J., Rathbun, J.T., Hoffman, J.M., Lusk, B.T.: Shock-tunnel waveform analysis. In: 37th Conference on Explosives and Blasting Technique. International Society of Explosive Engineers, San Diego, CA (2011)

55. Rathbun, J.T., McLane, D.J., Hoffman, J.M., Lusk, B.T.: Examination and Comparison of Shock Wave Characteristics in Open-Air Arena Test vs. Shock Tunnel Confinement. Blasting Fragm. 7, 1–10 (2013)

56. Yu, Q., Grönig, H.: Shock waves from an open-ended shock tube with different shapes. Shock Waves. 6, 249–258 (1996). doi:10.1007/BF02535738

57. Henkes, C., Olivier, H.: Flow characterization of a detonation gun facility and first coating experiments. J. Therm. Spray Technol. 23, 795–808 (2014). doi:10.1007/s11666-014-0083-4

58. Bazhenova, T. V., Bormotova, T.A., Golub, V. V., Kotel'nikov, A.L., Chizhikov, A.S.: The total pressure losses in a flow behind a shock wave emerging from channels of various geometries. Tech. Phys. Lett. 27, 669–670 (2001). doi:10.1134/1.1398963

59. Duan, Q., Xiao, H., Gao, W., Shen, X., Wang, Q., Sun, J.: Experimental investigation on shock waves generated by pressurized gas release through a tube. J. Loss Prev. Process Ind. 36, 39–44 (2015). doi:10.1016/j.jlp.2015.05.007

60. Haselbacher, A.C., Balachandar, S., Kieffer, S.W.: Open-Ended Shock Tube Flows: Influence of Pressure Ratio and Diaphragm Position. AIAA J. 45, 1917–1929 (2007). doi:10.2514/1.23081

61. Bass, C.R., Panzer, M.B., Rafaels, K.A., Wood, G., Shridharani, J., Capehart, B.: Brain injuries from blast. Ann. Biomed. Eng. 40, 185–202 (2012). doi:10.1007/s10439-011-0424-0

62. Kleinschmit, N.N.: A Shock Tube Technique for Blast Wave Simulation and Studies of Flow Structure Interactions in Shock Tube Blast Experiments, http://digitalcommons.unl.edu/engmechdisshttp://digitalcommons.unl.edu/engmechdiss/22, (2011)

63. Maeno, K., Kaneta, T., Morioka, T., Honma, H.: Pseudo-schlieren CT measurement of three-dimensional flow phenomena on shock waves and vortices discharged from open ends. Shock Waves. 14, 239–249 (2005). doi:10.1007/s00193-005-0256-7

64. Honma, H., Ishihara, M., Yoshimura, T., Maeno, K., Morioka, T.: Interferometric CT measurement of three-dimensional flow phenomena on shock waves and vortices. Shock Waves. 13, 179–190 (2003). doi:10.1007/s00193-003-0206-1

65. Ethridge, N.H., Lottero, R.E., Wortman, J.D., Bertrand, B.P.: Computational and experimental studies of blockage effects in a blast simulator. , ABERDEEN PROVING GROUND MD (1984)

66. Wortman, J.D., Lottero, R.E.: Comparison of Hull Hydrocode Computations of Shock Tube Blockage Effects on Target Loading for Step Shocks and Rapidly-Decaying Shocks. , Aberdeen Proving Ground MD (1982)

67. Celander, H., Clemedson, C.-J., Ericsson, U.A., Hultman, H.I.: The Use of a Compressed Air Operated Shock Tube for Physiological Blast Research. Acta Physiol. Scand. 33, 6–13 (1955). doi:10.1111/j.1748-1716.1955.tb01188.x

68. Rathbun, J.T., McLane, D.J., Hoffman, J.. M., Lusk, B.T.: Investigating Planer Propagation of a Shock Wave in a Shock Tunnel. In: 38th Annual Conference on Explosives and Blasting Technique. International Society of Explosive Engineers, Nashville, TN (2012)

69. Slotnick, J.A.: Explosive Threats and Target Hardening Understanding Explosive Forces, It's Impact on Infrastructure and the Human Body. In: Lonnermark, A. and Ingason, H. (eds.) Fourth International Symposium on Tunnel Safety and Security. pp. 19–30. International Symposium on Tunnel Safety and Security, Frankfurt, Germany (2010)

70. Jeremić, R., Bajić, Z.: An approach to determining the TNT equivalent of high explosives. Sci. Rev. 56, 58–62 (2006)

71. Berthelot, M.: Explosives and their power. John Murray, London (1892)

72. Berthelot, M.: Sur la force de la poudre et des matières explosives. Gauthier-Villars, Imprimeur-Libraire, Paris (1872)

73. Dobratz, B.M.: Properties of Chemical Explosives and Explosive Simulants. , Livermore, CA (United States) (1972)

74. National Center for Biotechnology Information: Pentolite | C12H13N7O18 - PubChem, https://pubchem.ncbi.nlm.nih.gov/compound/56841779

75. Marchand, K.A., Cox, P.A., Peterson, J.P.: Blast analysis manual, Part I–Level of protection assessment guide–Key asset protection program construction option (KAPPCO). (1991)

76. Merrifield, R.: Simplified calculations of blast induced injuries and damage. Health and Safety Executive, Technology and Health Sciences Division (1993)

77. Oswald, C.J., Skerhut, D.: FACEDAP user's manual. (1993)

78. Parisi, F., Balestrieri, C., Asprone, D.: Blast resistance of tuff stone masonry walls. Eng. Struct. 113, 233–244 (2016). doi:10.1016/j.engstruct.2016.01.056

79. Parisi, F.: Blast fragility and performance-based pressure-impulse diagrams of European reinforced concrete columns. Eng. Struct. 103, 285–297 (2015). doi:10.1016/j.engstruct.2015.09.019

80. Baker, W.E., Kulesz, J.J., Ricker, R.E., Bessey, R.L., Westine, P.S., Parr, V.B., Oldham, G.A.: Workbook for predicting pressure wave and fragment effects of exploding propellant tanks and gas storage vessels. , San Antonio, TX (1975)

81. Baker, W.E., Cox, P.A., Kulesz, J.J., Strehlow, R.A., Westine, P.S.: Explosion hazards and evaluation. Elsevier, New York (1983)

82. Blasts / Explosions | MB Industries, http://wm.mbindustries.com/what-we-protect-against/85-2/

83. Nalagotla, J.K.R.: Pressure-Impulse Diagrams using finite element analysis for reinforced concrete slabs subjected to blast loading, https://mospace.umsystem.edu/xmlui/bitstream/handle/10355/33223/NalagotlaPreImpDia.pdf?sequence=1&isAllowed=y, (2013)

84. Li, Q.M., Meng, H.: Pressure-impulse diagram for blast loads based on dimensional analysis and single-degree-of-freedom model. J. Eng. Mech. 128, 87–92 (2002). doi:10.1061/(ASCE)0733-9399(2002)128:1(87)

85. Piehler, T., Birk, A., Benjamin, R., Boyle, V., Summers, E., Aubert, S.: Near-Field Impulse Loading Measurement Techniques for Evaluating Explosive Blast. (2009)

86. Rao, B., Chen, L., Fang, Q., Hong, J., Liu, Z. xian, Xiang, H. bo: Dynamic responses of reinforced concrete beams under double-end-initiated close-in explosion. Def. Technol. 14, 527–539 (2018). doi:10.1016/j.dt.2018.07.024

87. Krauthammer, T., Astarlioglu, S., Blasko, J., Soh, T.B., Ng, P.H.: Pressure–impulse diagrams for the behavior assessment of structural components. Int. J. Impact Eng. 35, 771–783 (2008). doi:10.1016/J.IJIMPENG.2007.12.004

88. Song, H., Cui, J., Simonyi, A., Johnson, C.E., Hubler, G.K., DePalma, R.G., Gu, Z.: Linking blast physics to biological outcomes in mild traumatic brain injury: Narrative review and preliminary report of an open-field blast model. Behav. Brain Res. 340, 147–158 (2018). doi:10.1016/J.BBR.2016.08.037

89. Song, H., Konan, L.M., Cui, J., Johnson, C.E., Langenderfer, M., Grant, D., Ndam, T., Simonyi, A., White, T., Demirci, U., Mott, D.R., Schwer, D., Hubler, G.K., Cernak, I., DePalma, R.G., Gu, Z.: Ultrastructural brain abnormalities and associated behavioral changes in mice after low-intensity blast exposure. Behav. Brain Res. 347, 148–157 (2018). doi:10.1016/j.bbr.2018.03.007

90. Pun, P.B.L., Kan, E.M., Salim, A., Li, Z., Ng, K.C., Moochhala, S.M., Ling, E.-A., HongTan, M., Lu, J.: Low level primary blast injury in rodent brain. Front. Neurol. APR, (2011). doi:10.3389/fneur.2011.00019

91. Chen, H.-J., Xu, C., Li, Y., Chen, Z.-Q., Li, G.-H., Duan, Z.-X., Li, X.-X., Zhang, J.-Y., Wang, Z., Feng, H., Li, B.-C.: An open air research study of blast-induced traumatic brain injury to goats. Chinese J. Traumatol. - English Ed. 18, 267–274 (2015). doi:10.1016/j.cjtee.2015.11.006

92. Li, B.C., Li, Y., Xu, C., Wang, J., Chen, Z., Li, G., Zhang, J., Hu, S., Wang, L., Feng, H.: Blast-induced traumatic brain injury of goats in confined space. Neurol. Res. 36, 974–982 (2014). doi:10.1179/1743132813Y.0000000314

93. Säljö, A., Mayorga, M., Bolouri, H., Svensson, B., Hamberger, A.: Mechanisms and pathophysiology of the low-level blast brain injury in animal models. Neuroimage. 54, (2011). doi:10.1016/j.neuroimage.2010.05.050

94. Chen, C., Zhou, C., Cavanaugh, J.M., Kallakuri, S., Desai, A., Zhang, L., King, A.I.: Quantitative electroencephalography in a swine model of blast-induced brain injury. Brain Inj. 31, 120–126 (2017). doi:10.1080/02699052.2016.1216603

95. Kabu, S., Jaffer, H., Petro, M., Dudzinski, D., Stewart, D., Courtney, A., Courtney, M., Labhasetwar, V.: Blast-associated shock waves result in increased brain vascular leakage and elevated ROS levels in a rat model of traumatic brain injury. PLoS One. (2015). doi:10.1371/journal.pone.0127971

96. Turner, R.C., Naser, Z.J., Logsdon, A.F., DiPasquale, K.H., Jackson, G.J., Robson, M.J., Gettens, R.T.T., Matsumoto, R.R., Huber, J.D., Rosen, C.L.: Modeling clinically relevant blast parameters based on scaling principles produces functional & histological deficits in rats. Exp. Neurol. 248, 520–529 (2013). doi:10.1016/j.expneurol.2013.07.008

97. Risling, M., Plantman, S., Angeria, M., Rostami, E., Bellander, B.-M., Kirkegaard, M., Arborelius, U., Davidsson, J.: Mechanisms of blast induced brain injuries, experimental studies in rats. Neuroimage. 54, S89–S97 (2011). doi:10.1016/j.neuroimage.2010.05.031

98. Pham, N., Sawyer, T.W., Wang, Y., Jazii, F.R., Vair, C., Taghibiglou, C.: Primary blast-induced traumatic brain injury in rats leads to increased prion protein in plasma: A potential biomarker for blast-induced traumatic brain injury. J. Neurotrauma. 32, 58–65 (2015). doi:10.1089/neu.2014.3471

99. Kochanek, P.M., Dixon, C.E., Shellington, D.K., Shin, S.S., Bayir, H., Jackson, E.K., Kagan, V.E., Yan, H.Q., Swauger, P.V., Parks, S.A., Ritzel, D.V., Bauman, R., Clark, R.S.B., Garman, R.H., Bandak, F., Ling, G., Jenkins, L.W.: Screening of biochemical and molecular mechanisms of secondary injury and repair in the brain after experimental blast-induced traumatic brain injury in rats. J. Neurotrauma. 30, 920–937 (2013). doi:10.1089/neu.2013.2862

100. Budde, M., Shah, A., McCrea, M., Cullinan, W., Pintar, F., Stemper, B.: Primary Blast Traumatic Brain Injury in the Rat: Relating Diffusion Tensor Imaging and Behavior. Front. Neurol. 4, 154 (2013)

101. Kawoos, U., Gu, M., Lankasky, J., McCarron, R.M., Chavko, M.: Effects of exposure to blast overpressure on intracranial pressure and blood-brain barrier permeability in a rat model. PLoS One. 11, (2016). doi:10.1371/journal.pone.0167510

102. Sawyer, T.W., Wang, Y., Ritzel, D.V., Josey, T., Villanueva, M., Shei, Y., Nelson, P., Hennes, G., Weiss, T., Vair, C., Fan, C., Barnes, J.: High-Fidelity Simulation of Primary Blast: Direct Effects on the Head. J. Neurotrauma. 33, 1181–1193 (2016). doi:10.1089/neu.2015.3914

103. Skotak, M., Wang, F., Alai, A., Holmberg, A., Harris, S., Switzer, R.C., Chandra, N.: Rat injury model under controlled field-relevant primary blast conditions: Acute response to a wide range of peak overpressures. J. Neurotrauma. 30, 1147–1160 (2013). doi:10.1089/neu.2012.2652

104. Long, J.B., Bentley, T.L., Wessner, K.A., Cerone, C., Sweeney, S., Bauman, R.A.: Blast Overpressure in Rats: Recreating a Battlefield Injury in the Laboratory. J. Neurotrauma. 26, 827–840 (2009). doi:10.1089/neu.2008.0748

105. Svetlov, S.I., Prima, V., Kirk, D.R., Gutierrez, H., Curley, K.C., Hayes, R.L., Wang, K.K.W.: Morphologic and biochemical characterization of brain injury in a model of controlled blast overpressure exposure. J. Trauma - Inj. Infect. Crit. Care. 69, 795–804 (2010). doi:10.1097/TA.0b013e3181bbd885

106. Garman, R.H., Jenkins, L.W., Switzer, R.C., Bauman, R.A., Tong, L.C., Swauger, P. V, Parks, S.A., Ritzel, D. V, Dixon, C.E., Clark, R.S.B., Bayir, H., Kagan, V., Jackson, E.K., Kochanek, P.M.: Blast exposure in rats with body shielding is characterized primarily by diffuse axonal injury. J. Neurotrauma. 28, 947–959 (2011). doi:10.1089/neu.2010.1540

107. Kuehn, R., Simard, P.F., Driscoll, I., Keledjian, K., Ivanova, S., Tosun, C., Williams, A., Bochicchio, G., Gerzanich, V., Simard, J.M.: Rodent Model of Direct Cranial Blast Injury. J. Neurotrauma. 28, 2155–2169 (2011). doi:10.1089/neu.2010.1532

108. Säljö, A., Bao, F., Haglid, K.G., Hansson, H. a: Blast exposure causes redistribution of phosphorylated neurofilament subunits in neurons of the adult rat brain. J. Neurotrauma. 17, 719–26 (2000). doi:10.1089/089771500415454

109. Shridharani, J.K., Wood, G.W., Panzer, M.B., Capehart, B.P., Nyein, M.K., Radovitzky, R.A., Bass, C.R.D.: Porcine head response to blast. Front. Neurol. MAY, (2012). doi:10.3389/fneur.2012.00070

110. Courtney, M.W., Courtney, A.C.: Working toward exposure thresholds for blast-induced traumatic brain injury: Thoracic and acceleration mechanisms. Neuroimage. 54, S55–S61 (2011). doi:10.1016/j.neuroimage.2010.05.025

111. Mishra, V., Skotak, M., Schuetz, H., Heller, A., Haorah, J., Chandra, N.: Primary blast causes mild, moderate, severe and lethal TBI with increasing blast overpressures: Experimental rat injury model. Sci. Rep. 6, 26992 (2016). doi:10.1038/srep26992

112. Ouellet, S., Petel, O.E.: On the prospective contributions of the shock physics community to outstanding issues concerning blast-induced traumatic brain injury. Shock Waves. 27, 821–827 (2017). doi:10.1007/s00193-017-0773-1

113. Brown rat - Skull Base, http://skullbase.info/skulls/mammals/brown_rat.php

114. McGregor, B.: Meat, Carcass and Offal Yields of Goats, http://agriculture.vic.gov.au/agriculture/livestock/goats/production/meat-and-offal-yields-of-goats

115. Sarma, K.: Morphological and craniometrical studies on the skull of Kagani goat (Capra hircus) of Jammu Region. Int. J. Morphol. 24, 449–455 (2006). doi:10.4067/S0717-95022006000400025

116. Bass, C.R., Rafaels, K.A., Salzar, R.S.: Pulmonary injury risk assessment for short-duration blasts. J. Trauma - Inj. Infect. Crit. Care. 65, 604–615 (2008). doi:10.1097/TA.0b013e3181454ab4

117. Peters, P.: Primary blast injury: an intact tympanic membrane does not indicate the lack of a pulmonary blast injury. Mil. Med. 176, 110–114 (2011). doi:10.7205/MILMED-D-10-00300

118. Mrena, R., Pääkkönen, R., Bäck, L., Pirvola, U., Ylikoski, J.: Otologic consequences of blast exposure: A finnish case study of a shopping mail bomb explosion. Acta Otolaryngol. 124, 946–952 (2004). doi:10.1080/00016480310017045

119. Mayo clinic staff: Ruptured eardrum (perforated eardrum) - Symptoms and causes - Mayo Clinic, https://www.mayoclinic.org/diseases-conditions/ruptured-eardrum/symptoms-causes/syc-20351879

120. Madsen, J.: Explosives and Blast Injuries - Injuries; Poisoning - Merck Manuals Professional Edition, https://www.merckmanuals.com/professional/injuries-poisoning/mass-casualty-weapons/explosives-and-blast-injuries

121. White, C.S., Jones, R.K., Damon, E.G., Fletcher, E.R., Richmond, D.R.: The Biodynamics of Airblast. , Albuquerque, NM (1971)

122. Butler, F.K., Giebner, S.D., McSwain, N., Pons, P. eds: Prehospital Trauma Life Support Manual: Military Version. Jones and Bartlett Learning, Burlington, MA (2014)

123. Butler, F.K., Bennett, B., Wedmore, C.I.: Tactical Combat Casualty Care and Wilderness Medicine: Advancing Trauma Care in Austere Environments. Emerg. Med. Clin. North Am. 35, 391–407 (2017). doi:10.1016/j.emc.2016.12.005

124. Hirsch, A.E.: The Tolerance of Man to Impact. Ann. N. Y. Acad. Sci. 152, 168–171 (1968). doi:10.1111/j.1749-6632.1968.tb11974.x

125. White, C.S.: The Scope of Blast and Shock Biology and Problem Areas in Relating Physical and Biological Parameters. Ann. N. Y. Acad. Sci. 152, 89–102 (1968). doi:10.1111/j.1749-6632.1968.tb11969.x

126. Hirsch, F.G.: Effects of Overpressure on the Ear-A Review. Ann. N. Y. Acad. Sci. 152, 147–162 (1968). doi:10.1111/j.1749-6632.1968.tb11972.x

127. Song, H., Konan, L., Cui, T. Ndam, A. Simonyi, J., Johnson, C.E., Cernak, I., Demirci, U., Hubler, G.K., DePalma, R.G., Gu, Z.: The Behaviours and Neuropathology Linked with Biomechanics in a Murine Model of Open-Field Blast-Induced Mild Traumatic Brain Injury. In: Society for Neuroscience Annual Meeting, Neuroscience 2017. , Washington, DC (2017)

128. Song, H., Landry Konan, J., Cui, I., Ndam, T., Simonyi, A., Johnson, C.E., Cernak, I., Demirci, U., G., G., Hubler, R., DePalma, G., Gu, Z.: The behaviors and neuropathology linked with biophysics in a murine model of open-field blast-induced mild traumatic brain injury. In: Military Health System Research Symposium (MHSRS) (2017)

129. PCB Piezotronics: 137B23B Quartz, free-field, ICP® Blast Pressure Pencil Probe Specifications, www.pcb.com, (2018)

130. Walter, P.L.: Measuring Static Overpressures in Air Blast Environments. PCB Piezotronics, Depew, NY, Tech. Note No. PCB-TN-27-051009. (2010)

131. Walter, P.: Air-Blast and the Science of Dynamic Pressure Measurements. Piezotronics, PCB, Sound Vib. 10–16 (2004)

VITA

Barbara Rutter was born in Germany. She attended school in the Vernon Parish School District and graduated from Leesville High School in May 2008. She joined the United States Marine Corps in May 2009 and deployed to Afghanistan in 2012. She received her Bachelor of Science degree in Engineering Physics from Southern Arkansas University in December 2013. She received her Master of Science degree in Explosives Engineering from Missouri University of Science and Technology in December 2015. She was discharged from the Marine Corps in 2017. She received her Doctor of Philosophy in Explosives Engineering from Missouri S&T in May 2019.